Predicting Fatigue Crack Growth Life in Z-fibre Reinforced Composites

Tang, Suchao

Award date:
2019

Awarding institution:
Coventry University

Predicting Fatigue Crack Growth Life in Z-fibre Reinforced Composites

By

Suchao Tang

April 2018

A thesis submitted in partial fulfilment of the University's requirements for the Degree of Doctor of Philosophy

Certificate of Ethical Approval

Applicant:

Suchao Tang

Project Title:

Modelling and Design of Damage Tolerant Composite Joints

This is to certify that the above named applicant has completed the Coventry University Ethical Approval process and their project has been confirmed and approved as Low Risk

Date of approval:

06 August 2015

Project Reference Number:

P35957

Abstract

In the past three decades, the quest to produce lightweight structures has led to an increasing use of fibre reinforced polymer composite materials. A long-standing problem with composite laminates is their low delamination resistance and poor impact damage tolerance due to the lack of through-thickness reinforcement. Z-fibre (or known as Z-pinning) is an effective and simple method of increasing the delamination resistance and impact damage tolerance of composite laminates. Although the prediction methods of z-pinned structures under static load have been well developed in literature, few papers can be found that address the prediction of z-pinned structural response under cyclic loading.

The aim of this PhD project is to develop a methodology for accurately predicting the fatigue life of pin reinforced laminates, beyond the current state of the art. In order to achieve this aim, work has been undertaken to meet the following objectives:

- To model existing laminates (unpinned and pinned), to understand modelling techniques such as the virtual crack closure technique (VCCT) and the cohesive zone method (CZM), and to validate models against examples in literature;
- To develop a fatigue degradation law to account for the reduction of pins' bridging force under cyclic loading;
- To implement the degradation law to the prediction framework and predict the fatigue crack growth rate and life of pin-reinforced composite laminates;
- To conduct experimental tests to validate the accuracy of the proposed prediction methodology.

The scope of this work is limited to pin-reinforced laminate and simple joint subjected to the mode I loading. A fracture mechanics based approach is proposed to predict fatigue crack growth life of z-pinned joints, which uses the finite element method (to deliver the crack tip strain energy release rate) in conjunction with a crack growth rate law. The strain energy release rate is evaluated by the VCCT method in finite element analyses, and cohesive elements are used at discrete pin locations to represent the z-pin bridging forces. The cohesive parameters within the FE model are degraded with the cycle numbers to account for the property degradation and bridging force reduction during fatigue loading.

A degradation law is proposed to describe the process of a z-pin debonding and frictional pull-out from laminate under the mode I fatigue loading, which is based on the damage mechanics approach with empirical fitting parameters.

As demonstration examples, the fatigue crack growth life of a pin-reinforced double cantilever beam (DCB) and a pin-reinforced "top-hat" joint have been predicted by the proposed methodology. The predicted results are validated by experimental test results; both the crack length vs. fatigue life curve and fatigue crack growth rate vs. crack length curve are found to be in good agreement.

Contents

List of figures

List of table

1. Introduction

1.1 Background

The ongoing requirement to produce increasingly lightweight structures has led to an increasing use of composite materials, especially in the aerospace industry in which excess weight carries a significant operational cost. Aircraft structures in the latter half of the 20th century were mostly made of aluminium alloys and the steadily increasing use of composites was mainly limited to secondary structures. With growing experience and confidence, the use of carbon fibre reinforced plastic (CFRP), has been expanded to primary structures in the 21st century.

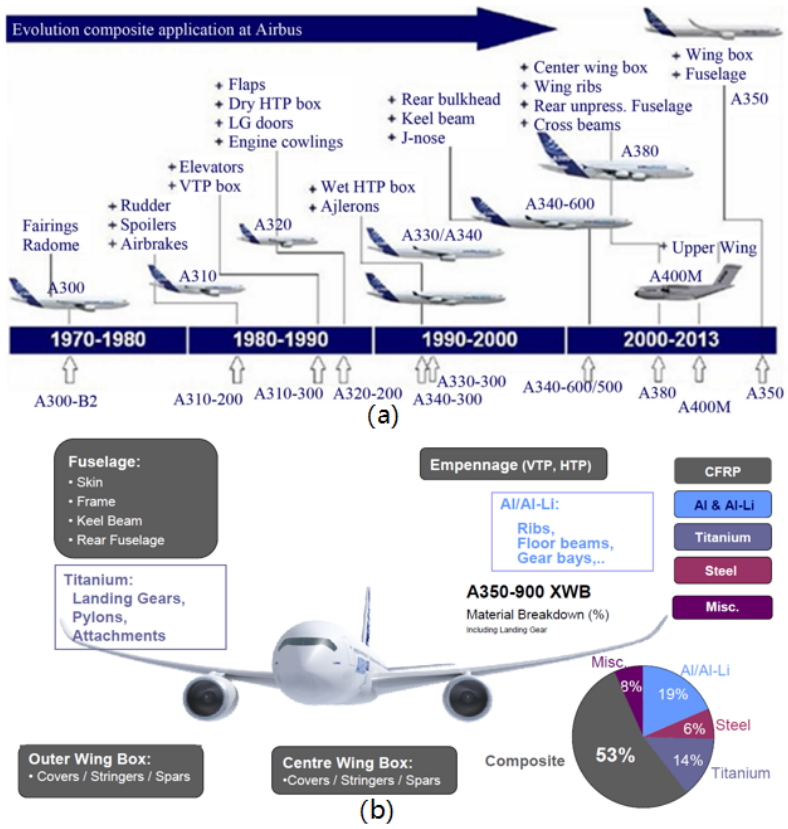

Fig. 1-1 (a) Evolution of the use of composites in Airbus aircraft [1] and (b) usage of composite materials in the A350 XWB [2]

Fig. 1-1a shows the evolution of composite material use in Airbus aircraft structures since 1970. The tendency towards increasing use of composite material has reached a significant milestone with the

Airbus A350XWB (Fig. 1-1b) where the proportion of composite material exceeds 50% of the total material usage. A single piece made of composite material can replace an entire assembly of metal by parts consolidation, streamlining the production process and reducing lifetime maintenance. The impressive all-composite fuselage for A350 XWB is shown in Fig. 1-2, with 13 metres long and comprises four panels and the floor grid.

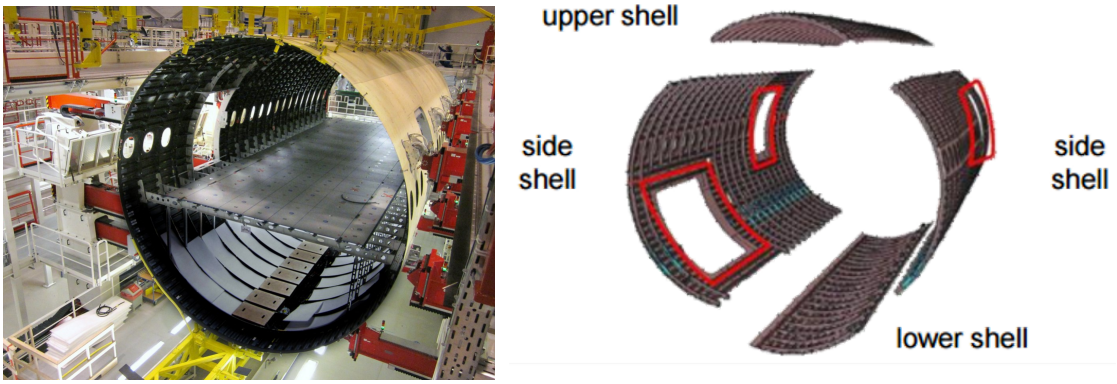

Fig. 1-2 (a) The first A350 XWB forward fuselage in Nordenham, Germany (b) a sketch of the "four panel" assembly into a fuselage by "lap joint" configuration.

As a replacement for "traditional" materials such as aluminum and titanium alloys, carbon fibre reinforced plastics also have the advantage of fatigue resistance, design flexibility and corrosion resistance. While initially more expensive to produce than conventional metallic parts, composite components can save aircraft operators cost on future maintenance costs since the material doesn't rust or corrode. An A350 XWB, for example, requires 50% fewer structure maintenance tasks, and the threshold for airframe checks is at 12 years compared to eight for the A380.

One area where composite materials do not exhibit such clear cut advantages over conventional materials occurs when composite components must be joined together. A key requirement for the future development of composite aircraft structures is for improved understanding of joining technologies, and of improvements to the joining technologies available. There are two main joining techniques available for composites - mechanical fastening (such as bolting and riveting) and adhesive bonding. As the currently preferred method for joining aerospace structures, bolted joints suffer severely from stress concentration and fiber damage due to hole drilling, necessitating thicker

structures in the joint region. Adhesive bonds offer a relative weight reduction, and offer a more uniform load distribution. However, due to the absence of a through-thickness compressive load from a fastener, bonded joints are vulnerable to interlaminar damage resulting from impacts, delamination and debond.

In the civil aerospace industry, the bonding of composites is well-understood and the processes are well-developed for various joints of secondary structures. For example, the Airbus A350XWB has a large number of stiffeners-to-skin panels (Fig. 1-3b) which contain composite to composite bonded joints. The overall bondline length of these joints amounts to about 5 km per aircraft [3]. However, composite bonded joints are not currently used in aircraft primary structures (Fig. 1-3a) that must be certified for damage tolerance requirements [3].

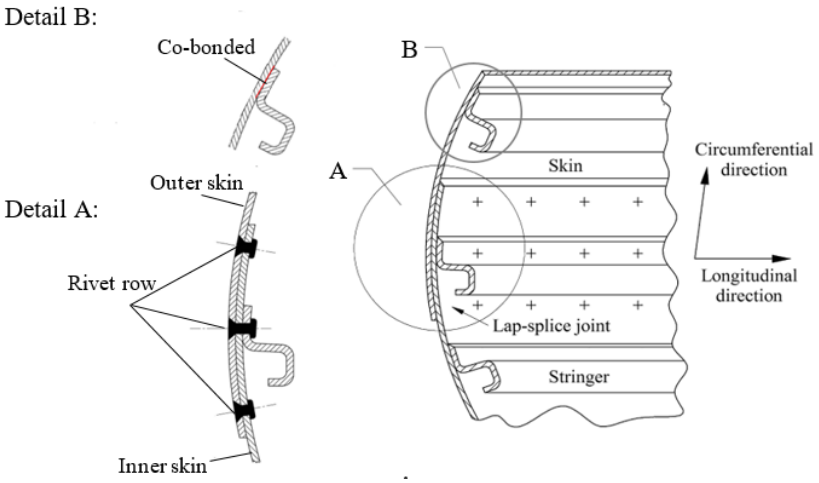

Fig. 1-3 Typical composite fuselage with (a) riveted lap splice joint (primary structures) (b) co-bonded stiffener-to-skin joint (secondary structures)

The main certification issue is the significant scatter in the long-term durability of bonded joints, which is affected by many factors such as surface treatment, adhesive curing cycle, curing conditions and adherend's moisture content [4]. In addition to manufacturing uncertainties, fatigue life prediction of bonded composite joints is challenging and also influenced by many factors (e.g. load level, strain rate and environmental conditions) [5-8]. The impact of those factors on the joint's long term durability require expensive and time-consuming experimental fatigue investigations.

According to [4], one of three options should be met to certify damage tolerance of structures with bonded joints:

- Nondestructive testing/inspection (NDI/NDT)
- Proof testing
- Crack-stopping design features

To date, no method of nondestructive testing/inspection (NDI/NDT) has demonstrated the capability to quantify the long-term strength and durability of bonded joints. Furthermore, proof testing each critical bonded joint on every new aircraft would be prohibitively expensive. A promising alternative approach is to establish crack-stopping design features, such as so-called rivet-less nut plates [9], surface modifications [10] or small metal rods (z-rods) as through-thickness reinforcement [11-14]. It can be concluded that z-rods add to the damage tolerance of the laminate predominantly by crack bridging and energy absorption during pullout from the matrix resin. Additionally, they add to the damage tolerance by plastic deformation of the metal reinforcement. However, a problem with those crack-stopping design features is the high cost and complex manufacturing process.

1.2 Z-pins in composite laminates and joints

A technique that has great potential for improving the performance of bonded joints but with only a modest increase in manufacturing cost, is the insertion of high stiffness, high strength pins in the through thickness direction [15] in a process called Z-fibre® pinning, or z-pinning. The bridging mechanism of z-pinning is similar to the z-rods, but z-pinning is the only technique which can be applied directly to the prepreg laminates without excessive fibre damage. This is important because presently many load carrying composite components, including many aircraft structures, are made using prepreg laminates, and excessive fibre damage would degrade the in-plane mechanical properties.

Z-pins were initially used to improve the interlaminar fracture toughness and impact damage resistance of composite laminates (Fig. 1-4a), but also improve resistance to fatigue loading. Research in [15] has also shown that z-pins form a large-scale crack bridging zone to retard fatigue crack growth, which is similar to that created under static loading.

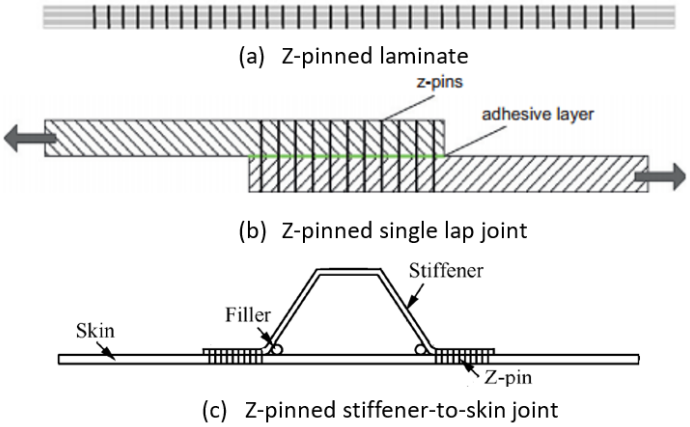

Fig. 1-4 Schematic principle of z-pins as reinforcing elements in (a) laminates and (b) bonded lap joints [16] (c) stiffener to skin hat joint [121]

The mechanism of bond failure which involves bonded plies being pulled (i.e. mode I failure) apart suggests that the concept of z-pins could be expanded to composite structural joints to improve the through thickness strength properties (Fig. 1-4b). For these reasons, z-pins are used in military aircraft such as the Boeing F18 E/F inlet ducts (Fig. 1-5), with a cost savings of $83000 and a reduction of 35 pounds in weight, by replacing 4000 titanium fasteners in what was previously a bolted design.

Fig. 1-5 Z-pinning applications in aerospace: composite inlet duct skins fastened with the hat stringers by z-pins for the F18 E/F Super Hornet center fuselage section

Accompanying the ongoing development of z-pins, several prediction approaches have been developed to assess the failure of z-pinned composite structures under static loading [17-24]. However, any future introduction of z-pinned composite bonded joints into primary aircraft structures requires an understanding of their fatigue performance and a corresponding prediction methodology to be established. Neither of these requirements have yet been adequately met and therefore the application

of z-pins as feature in composite bonded joints is generally limited to military aircraft and the automotive industry. The development of a methodology to predict the fatigue life of z-pinned composite bonded joints is therefore of high interest. Prediction of z-pinned composite laminates under mode I fatigue loading is a first step towards modelling pinned joints in real structures.

1.3 Scope, aim, and objectives

The scope of this research is to develop innovative predictive techniques to assess the failure of z-pinned composites under mode I fatigue loading. The primary aim of this research is to develop a reliable methodology for predicting the fatigue life of z-pin reinforced composite laminates, beyond the current state of the art.

In order to achieve this aim, work has been undertaken to meet the following objectives:

1. To review and study current published literature in composite joints, through-thickness reinforced laminates, and analysis methods to understand the current state-of-the-art in these fields

2. To model both unpinned and z-pinned laminates under static load to develop a thorough understanding of finite element (FE) analysis and fracture analysis mechanics theory, and to develop relevant modelling skills, and using virtual crack closure technique (VCCT) and cohesive zone model (CZM) to calculate fracture mechanics parameters

3. To investigate the z-pin bridging force degradation under fatigue loading, and to formulate an appropriate fatigue degradation law that represents this behavior. To determine the constitutive model for individual z-pins subjected to fatigue mode I loading, and implement the constitutive model to the prediction framework

4. To predict fatigue crack growth rate and life of pin-reinforced laminate in a double cantilever beam (DCB) and in a pin-reinforced bonded joint (top-hat stringer panel)

5. To conduct experimental tests on DCB geometry to validate predictions made with the FE model and pin fatigue model developed in this study

1.4 Structure of the Thesis

This thesis is structured with eight chapters, and can be considered as having three main parts:

- In Part 1, an overview of the problem and motivation of the study are stated (Chapter 1). A state-of-the-art literature review is presented in Chapter 2, which is followed by a summary

of the theories used in this thesis (Chapter 3).

- In Part 2, methodologies developed in this research is described in Chapter 4. Both unpinned and pinned DCB/ENF are modelled under the static loading, followed by fatigue life prediction of unpinned DCB/ENF. The results are then validated by comparison with experimental data in published papers (Chapter 6).
- Part 2 continues by predicting the fatigue crack growth life of a pinned DCB (Chapter 7), and fatigue experiments are performed to validate the prediction (Chapter 5). Furthermore, the methodology is extended to predict the fatigue life of a pinned hat joint, and this is validated by comparison with the results obtained from the literature (Chapter 7).
- In Part 3, final conclusions and recommendations for future work are presented (Chapter 8).

2. Literature Review

2.1 Current joining techniques and prediction method for composite structures

Currently jointing practice for thermosetting composites in aerospace industry are mechanical fastening, adhesive bonding or hybrid joints, such as bolted/bonded joints. Understanding of their failure modes is beneficial to the failure analysis of pin-reinforced bonded structures.

2.1.1 Mechanical fastening

Mechanical fasteners can be categorized into four types: pins, rivets, screws and bolts. Since pins are not viable for conventional joints, and screws can be pulled out of the laminate easily, only rivets and bolts are recommended for load-carrying CFRP joint [25]. In general, rivets are relatively lighter and cheaper than other types of mechanical fastening while bolts have the greatest strength.

Fig. 2-1 ASTM D 6484/6484M: fixture of Open-hole compression test[27].

Many experimental tests have been performed to validate the properties of mechanically fastened joints designs in composite materials. Some common standards have been established to obtain comparable results (e.g. American Society for Testing and Materials (ASTM) [26-30], Military Handbook (MIL-HDBK-17F working group) [31], National Aeronautical Space Administration (NASA) [32-35]). The ASTM and MIL standards are applicable to tape and fabric reinforced composites, which includes open-hole tensile [26] and compressive test [27] (Fig. 2-1), filled-hole tensile and compressive tests[28], and the bearing test with static/ fatigue loading [29, 30]. The third standard (NASA), is applicable to textile composite materials such as braided, woven, knitted, and

stitched composites.

As reported in D5961/D5961M-05e1 bearing test [29], there are several failure modes of mechanically fastened joints, including those shown on (Fig. 2-2):

(a) lateral (net-tension),
(b) shear-out,
(c) bearing,
(d) tear out, and
(e) cleavage.

Among those failure modes, only bearing failure is acceptable for the designer since such local failure is stable, and will result in catastrophic failure.

Fig. 2-2 Bearing test failure modes for ASTM D 5961/D 5961M-05: (a) lateral (net-tension), (b) shear-out, (c) bearing, (d) tear out, and (e) cleavage [29].

After the development of experimental standards, several investigations have been carried out to predict bolted joint in the composite material. Camanho and Lambert [36] proposed a methodology that is able to predict the elastic limit in each ply and ultimate failure load of mechanically fastened composite joints, based on the calculation of stress distribution for every single ply using semi-analytical method (elasticity theory and finite elements); Ireman [37] used finite element based methods to produce design diagrams, which are capable of predicting the bearing strength under different uniaxial bearing-bypass load. Load distribution in a multi-row fastener joint was first obtained by FE method, and then stress analysis for infinite plates was carried out to determine whether the critical failure is by net-section or bearing. This predictive method gave reasonable correlation with the experiment, with a considerable time saving; Zhang [38] used 1D springs to model fasteners, and predicted composite joints using boundary element formulation; Dano et al. [39]

developed a methodology to predict bearing stiffness using FEA based on progressive damage model. His methodology is useful for investigating material property degradation rules and failure criteria.

There are many important factors to consider in the design of composite joints. Selections of matrix resin and fiber, initial preload or clamping force, and lay-up sequences have been discussed in [40-43]. The effects of e/d, w/d ratios (as illustrated in Fig. 2-2) and the initial bolt clamping torque of pultruded fiber reinforced plastic (PFRP) composites have been studied by Cooper and Turvey [44]; Sun [45] investigated the effect of clamping area on the stiffness and failure load of bolted composite joint; Khashaba [46] studied the effect of washer size on the strength of composite bolted joints; McCarthy [47] investigated the effects of bolt-hole clearance on the stiffness and bearing strength of single lap bolted composite joints.

2.1.2 Adhesive bonding

For aerospace applications, adhesively bonded joints offer significant advantages over mechanically fastened joints, such as lower local stress concentrations, smooth surfaces, effective manufacturing cost and weight savings. However, bonded joints are not considered to be reliable for long-term durability (30 years) due to the difficulties of non-destructive inspection, sensitivity to peel loading, and the inability to disassemble and reassemble adhesive joints for maintenance and/or inspection. Material degradation in service can be caused by exposure to ultraviolet light, chemical attacks from the environment and ageing in the presence of moisture [48].

Adhesive bonded joints can be divided into four common configurations (Fig. 2-3): single lap joint, double lap joint, scarf joint and stepped joint. The single lap joint is the weakest configuration due to its inherent eccentricity, and double lap joints have better bonding strength since they do not have eccentricity problem. However, scarf joints and stepped joints have best bonding strength due to their largest bonding area [49].

In general, adhesively bonded joints will fail in one of 5 modes, which are shown on Fig. 2-4. The adherends can fail in longitudinal tension (marked as “tensile” on the figure), delamination (interlaminar) or transverse cracking (marked as “transverse”). Failure can also occur within the

adhesive (called “cohesive” failure) and in the middle of adherends and adhesive (called “adhesive” failure, which is not shown on Fig. 2-4).

Fig. 2-3 Basic types of adhesive bonded joint [49]

Fig. 2-4 Failure modes of adhesive bonded joint [49]

Many researchers have investigated the high stress concentration near the overlapping edge of adhesive joints, due to the discontinuity of elastic properties at material interfaces. Based on elastic stress analysis, Goland and Reissner [50] illustrated that high peel and shear stresses concentration can be affected by geometric parameters (e.g. overlap length and adhesive thickness). In order to reduce stress concentration, Sancaktar and Lawry [51] have carried out a photo-elastic study of prebend single lap joints. The study indicated that prebend angles reduced the stress concentrations on the

overlap region. The load carrying capacity increased as much as 71 % by using pre-bent adherends. In addition, Hart-Smith and Bunin [52] studied the effect of tapered overlap edges while Adams [53] has also investigated the fillet geometry at the overlap edge by experiment. It has been demonstrated that the transverse and tensile stress concentration is also alleviated by the fillet.

Many analytical models have been proposed for prediction of adhesively bonded joints. The earliest analysis developed by Goland and Reissner [54] was a cylindrical bent plate analysis of single lap joint, introducing the effects of joint edge moment to account for eccentricity. Later, Hart-Smith [55] proposed a layered beam model to predict the behavior of single lap joints. This beam model removes the lumped overlap restriction which was assumed by Goland and Reissner. Oplinger [56] also developed a beam method which is able to predict large deformation of the joint overlap. In his method, the effect of overlap bending moments is calculated, and individual deformation of upper and lower adherends are assumed. Adams [57,58] developed a minimum strain method based on 2-D elasticity theory, to ensure stress-free boundary conditions at the free ends, although the analytical analysis assumed that constant peel and shear stresses along the thickness of the adhesive.

The necessary assumptions and simplifications limit the applicability of analytical solutions to real world applications. Such limitations can be eliminated by numerical methods, in addition, numerical methods can improve the prediction because they take into account the geometric nonlinearity of the problem, and the effect of detailed geometric features such as fillets [59,[60]. Wooley and Carver [61] successful applied the 2D linear finite element method to single lap joints to investigate the effect of material non-linearity, spew fillets and adherend tapering; Adams and his co-workers [62, [63] studied the effect of adhesive spew fillets on the reduction of peak adhesive stresses. Both geometric and material nonlinear behavior were modeled based on plane strain assumption.

To take into account the properties of the adhesive, Hart and Barker [64] developed a 2D four node element to represent adhesive layer with finite thickness as a separate feature. This approach enables the joining of different materials; Lin and Lin [65] developed an element that modelled any possible adhesive layer conditions and nonidentical adherends based on Timoshenko beam theory. Those

methods assumed linear variation of normal and shear transverse stresses through the thickness of the adherends.

Andruet [66] proposed both 2D and 3D finite elements for geometrically nonlinear adhesively bonded joints. In the 2D model, Andruet applied Bernoulli beam elements at the adherends, and plane elements at the adhesive layer while the interface between adherend and adhesive are rigidly linked using beam elements. For the 3D model, shell elements and solids elements are used to represent adherends and adhesive respectively. In general, 2D FEM is very convenient to approximate stress distributions along the overlap, whilst 3D FEM can capture the free-edge effect, which causes delamination and damage to cross-plies in composites.

2.1.3 Hybrid joining techniques (bonded/bolted joints)

Efficient joint practice is crucial to exploiting the full potential of CFRP. As the presently favored joining method, bolted joints suffer severely from stress concentrations around the bolt holes.

If the composites are joined by adhesive bonding, the through-thickness damage is often occurs owing to the absence of a mechanical fastener. To inhibit those damage mechanisms, Hart-Smith [67] investigated a hybrid (bonded/bolted) stepped lap joints theoretically, but no significant benefit over perfectly bonded joints has been found. However, the idea of combining adhesive bonding and mechanical fastening was then employed by many researchers to develop through-thickness joint reinforcement.

Certain designs of hybrid bonded/bolted (HBB) joint have been shown to retain greater static and fatigue strength. Li [68] carried out experimental static and fatigue tests on a butt joint configuration (Fig. 2-5). Compared with conventional bonded joint and bolted joint, the static strength is improved by a factor of 52% and 127%, respectively. The fatigue life of the bonded /bolted joint was about 5-15 times higher than the bonded joint.

The improvement in [68] is indicative of good load sharing between two joining method. The capacity of load sharing depends on many factors: joining type, lay-up, thickness of the specimen, bolt diameter,

interference-fit, adhesive properties, etc.

A number of experimental studies [69-74] reported that the bonded/bolted joint initially failed in adhesive bonding, follow by typical bolted joint fail. Kelly [70] performed experimental static tests for a polyurethane adhesive bonded/bolted joint configuration. Strength is improved by a factor of 21% and 33% over the individual bonded and bolted joints, respectively. Nevertheless, when the polyurethane adhesive replaced by epoxy adhesive, no improvement was reported. When little to no load sharing occurs, there is only a very limited (or nonexistent) improvement in the strength of the bonded/bolted joint. In [75], a bonded/bolted single lap joint was tested. Different from the butt joint in [68], the hybrid joint did not improve compared to the individual joint.

Fig. 2-5 Schematic configurations of composite butt joints [68]

To predict the response of bonded/ bolted joints subjected to the static loading, several analytical models and numerical models is developed in open literature.

The analytical models are based on Goland and Reissner's classical bonded joint model and are resolved by the matrix displacement method [76, 77]. Advantage of these models are the efficiency based on a large number of simplifications and incorporate empirical factors. However, analytical models are difficult to predict the stress fields on adhered due to the complex nature of composite material. As an alternative solution, this problem is overcome by 3D FE analysis [78, 79], with the expense of computationally expensive.

2.1.4 Summary

In this literature survey, both mechanical fastening and adhesive bonding have been reviewed, covering typical joining types, possible failure modes, experimental tests and prediction methods (analytical and numerical). Both mechanical fastening and adhesive bonding have significant

limitations as methods of joining composite laminates.

The relative advantages and disadvantages of mechanical and adhesive joining methods are summarised in Table 2-1 below.

Table 2-1 Mechanical fastening vs. adhesive bonding

	Mechanical fastening	Adhesive bonding
Advantages	● Simple manufacturing process ● Simple inspection procedure ● Provides through-thickness reinforcement ● Simple disassembly	● Small stress concentration ● Excellent fatigue properties ● Sealed against corrosion ● Relatively lightweight
Disadvantages	● Stress concentration ● Prone to corrosion ● Prone to fatigue cracking	● Sensitive to peel stress ● moisture degradation ● Difficult inspection and disassembly

An established alternative approach is bonded/bolted joint which is potentially attain better static strength than the conventional bonded and bolted joints. However, few bonded/bolted joint configurations have been reported that experience load sharing which limit the preformence of bonded/bolted joints.

2.2 Fatigue failure and analysis method

A structure can fail suddenly under single application of a high stress, or can fail under cyclic loading at lower stress levels. The latter mechanism of material failure is a phenomenon called “fatigue”, and was first identified as a critical loading pattern of metal in the 1850s. After extensive study, numerous experimental programs have been conducted to characterize the fatigue behavior and many theoretical or empirical models have been established to evaluating the service life of materials under fatigue loading.

Fatigue performance of composite laminates has been intensively studied by many researches. Sjögren [80] conducted tests for composite laminates subjected to both static and fatigue loading. The result shows the threshold values G_{th} of the ENF test in the fatigue loading were only about 10% of G_C

owing to the brittleness and weak fatigue resistant of the matrix. Since the current generation of composite structures follow the 'no growth' design criterion, this places a severe constraint upon the design of light weight aircraft structures.

2.2.1 Mechanically fastened joints

When composites are joined by a mechanical fastener, the stress concentrations caused by hole significantly lowers the fatigue performance. The fatigue performance is affected by many factors, including: fastener type, preload/torque, bolt-hole clearance and selection of R-ratio and environmental conditions.

The bearing strength and the bolt torque relaxation of bolted composite joints under cyclic load was studied by Chen [81]. Results show that the fatigue performance improved when higher preload applied. Chen's results also showed that specimens exposed to humid environment show reasonable declines in fatigue performance.

Counts [82] investigated the effects of frequency, R-ratio and thermal aging upon a bolted composite joint under cyclic compression test. The fatigue results were unaffected when the frequency varies from 0.1 Hz to 10 Hz and also insensitive to 10,000 h thermal aging. In addition, higher R-ratios resulted in higher maximum bearing stresses.

Starikov [83] experimentally studied the composite multirow joints with countersunk titanium and composite fasteners under cyclic loading. The result shows that titanium fasteners have better fatigue performance than composite fasteners, due to their better ability to withstand cyclic shear loading.

Wei [84] investigated the interference fit size effect of bonded/ bolted lap joint under cyclic loading. Significant improvements have been reported due to the interference fit effect, and that fatigue life of the best interference fit would be 5-10 times h than that of the worst interference fit (0%, neatfit).

2.2.2 Adhesive bonded joints

The fatigue behavior of adhesively bonded composites is affected by many factors, including: the material property of adhesives and adherends, the geometry of joints, environmental conditions,

applied loads, and the quality of surface treatment and curing conditions.

Stiffness/strength based work

Since the degradation of strength and/or stiffness is used as a measure of increasing damage during fatigue loading, considerable experimental investigation have been carried out to obtain the S-N curve.

Many researchers have investigated the effect of different shapes and configurations of bonded joints to improve fatigue performance. Ishii [85] and Zeng [86] studied the effect of overlap length for bonded lap joints in fatigue. Counterintuitively, better fatigue performance was founded for bonded joint with shorter overlap, since only slight improvement has been found when 30 mm overlap replace by 20mm. Similar trends were observed for fatigue crack initiation stage.

Mattos [87] studied the effect of two different adhesive edge shapes (Squared Edge, Spew Fillet Edge) and of different surface preparations (peel-ply, grit blasted and degreased) in the single lap joint. Mattos concluded that both static and fatigue performance of two joints with different bonded areas can be correlated using a shape factor. Yi-Ming Jen [88] experimentally investigated the effect of scarf angles on the bonded scarf joints under cyclic loading. The result (Fig. 2-6) showed great improvement of fatigue performance with increasing scarf angle.

Fig. 2-6 Maximum cyclic applied stresses vs. fatigue life relation [88]

In addition, many researchers presented investigations in other ways to achieve better fatigue

performance. Khalili [89] experimentally studied the influence of adhesive reinforcement in composite single lap joints. Continuous glass fibers, chopped glass fibers and micro-glass powder were added to the adhesive layer, and the result (Table 2-2) shows a 125% improvement when the adhesive was reinforced with 30% micro-glass powder. Yang [90] studied the effect of curing conditions (pressure, temperature and curing time) on the fatigue lifetime of adhesively bonded joint, and optimized the curing scheme by means of the Orthogonal Test.

Table 2-2 Fatigue improvement for different adhesive reinforcement [89]

Adhesive joint	% Increase in fatigue life
Neat adhesive	–
30% unidirectional 0° fibre reinforced adhesive	84.8
30% unidirectional 45° fibre reinforced adhesive	41.5
30% unidirectional 90° fibre reinforced adhesive	−7
30% chopped fibre reinforced adhesive	62.7
20% micro-glass powder reinforced adhesive	71.6
30% micro-glass powder reinforced adhesive	125.3
40% micro-glass powder reinforced adhesive	77

For composite material, the orientation of the interface ply significantly affected the fatigue behavior. Johnson and Mall [91] investigated three interface conditions (0/0, 45/45 and 90/90) in composite cracked lap shear joints. For the 0/0 interface, fatigue crack initiation and propagation occurred in the adhesive region (adhesive failure (Fig. 2-7)). For the 45/45 interface, crack initiation occurs in the adhesive layer (cohesive failure), then propagate as delamination at the 0/45 interface. For the 90/90 interface, crack initiation occurs transversely, and followed by a combination of intraply failure and delamination. De Goeij [92] investigated the fatigue performance of composite bonded joints, and concluded joints with 0/0 interface have better fatigue strength than those with 45 degree and 90 degree oriented ply at the interface.

Fig. 2-7 Adhesive failure and cohesive failure [91]

The storage and test environment (temperature-thermal aging, and humidity water absorption) also significantly affect the fatigue strength of bonded joints. Ashcroft [93] experimentally investigated the fatigue strength of composite lap–strap joints under different test environments. The result reveals that the fatigue threshold load is considerably reduced as the glass transition temperature, T_g, was approached.

Fracture mechanics based work

Delamination is the growth of a crack between plies in the laminate, which is typically analysed using linear elastic fracture mechanics (LEFM) that uses the strain energy release rate, G, to quantify the fatigue resistance.

Generally, the strain energy release rate that correlates to crack propagation rate (da/dN) can be either the G_{max} or $\triangle G$. Mall [94] experimentally study the load ratio R effect, on the crack growth rate in double cantilever beam (DCB) and cracked lap shear (CLS) joints.

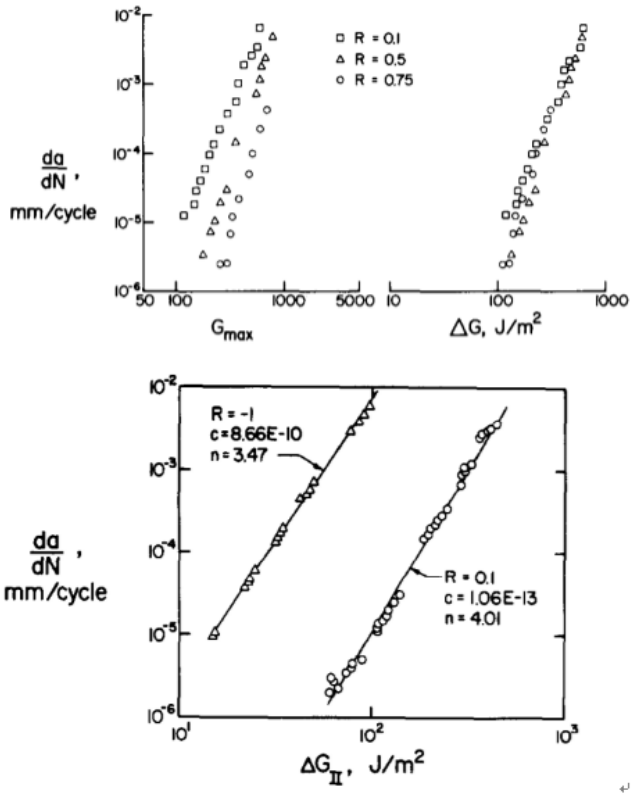

Fig. 2-8 da/dN against G_{max} or $\triangle G$ under different applied load ratio [94, 95]

Mall's [94] results (presented in Fig. 2-8) showed an apparent improvement in the relation of crack propagation rate against G_{max} at the higher values of R ratio, but the relation of da/dN against $\triangle$G is insensitive to the R ratio. Thus, the author concluded that $\triangle$G is the driving parameter for fatigue crack growth in bonded composite joints. This is due to the fact that under the same G_{max} the R ratio could be very different, and $\triangle$G can reflect R ratio properly. However, a different trend was found in a lap joint [95], when R= -1.This is mostly due to the increase of $\triangle$G.

The adhesive thickness effect has been studied by many researchers under cyclic loading. Mall and Ramamurthy [96] conducted mode-I tests for adhesively bonded composite joints, and found that the fatigue crack propagation rates is insensitive to the bondline thickness until the thickness increased to 0.508mm. Azari [97] investigated the influence of increasing adhesive thickness, between 0.13mm to 0.79mm, on the fatigue behavior of aluminum bonded joints under mixed-mode (ADCB) loading. Azari found that the influence of adhesive thickness was more noticeable when the da/dN is very high under mixed mode loading.

2.2.3 Fatigue life prediction methodology of composite laminates and joints

Current fatigue prediction approach could be categorized as:

- total life
- phenomenological models
- progressive damage models

Total life based approaches assume linear damage accumulation under cyclic (fatigue) loading. These methods are simple to execute, but have restricted capacity in fatigue prediction of complex structures, and it requires large amount of data, e.g. the *S-N* data that are sensitive to fibre orientation, geometry and load ratio. The total life based approaches characterized the final failure but there is no physical basis for the assumed damage accumulation and hence it is not applicable to monitor the damage in the sample. This could be overcome by the utilization of phenomenological models

Phenomenological models measured the degradation of strength or stiffness experimentally (e.g. Fig. 2-9) and related to damage evolution. Although those models are applicable to predict the residual

strength of a joint after a period of fatigue loading, they are extremely rely on experiments. A more adaptable method to characterizing fatigue damage is through progressive damage approaches.

Fig. 2-9 example of Phenomenological models [98] (Residual failure load curves for different fatigue loads).

Progressive damage approaches are widely used methods which describe fatigue crack popagation in the structure based on fracture mechanics or damage mechanics.

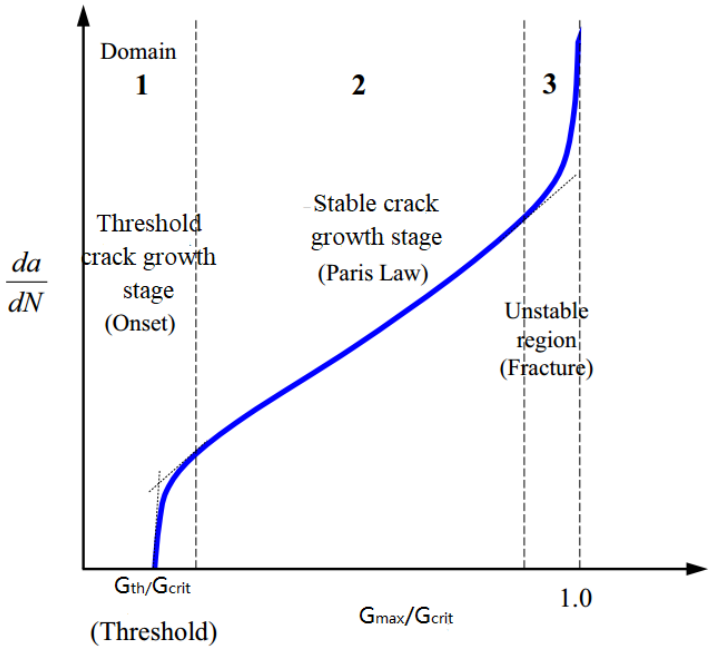

Fig. 2-10 Conceptual sketch of da/dN vs. G_{max}/G_{crit}

Fatigue crack growth proceeds in three distinct stages: crack initiation, stable crack propagation, unstable crack propagation (catastrophic failure). Initiation is the most complex stage of fatigue

fracture and take greatest portion of the fatigue life. However, aircraft is designed for damage tolerance, allowing long crack growth and inspection. Thus, this study focuses on the second stage which is stable crack growth.

In fracture mechanic based progressive damage approach, the stable crack propagation phase (region 2 in Fig. 2-10) is assumed to be dominant, and the crack growth rate is governed by the stress intensity factor *K* (for metallic materials) or strain energy release rate *G* (for composite materials).

Usually, an empirical crack growth law is applied to characterize crack growth life. Most of crack growth laws are based on the one proposed by Paris and Erdogan [99], which defined the d*a*/d*N* as a power law function of stress intensity factor in the crack front.

$$\frac{\mathrm{da}}{dN} = C\Delta K^m \tag{2-1}$$

By integrating the crack growth law, an estimate of d*a*/d*N* (and hence the life of the joint) can be obtained.

Fatigue crack propagation rate and joint life in bonded structures can be predicted by means of the FEA in combination with the crack growth law. Wahab [100] established a generalized fatigue crack growth prediction framework for composite bonded joints as shown in Fig. 2-11.

Fig. 2-11 Summary of the steps of fatigue crack growth life prediction from [100]

The detailed procedure of fatigue life prediction proposed can be categorized as follows:

- Experimental fracture mechanics tests (e.g. DCB specimens) were carried out to generate crack growth data, and 2D finite element analysis are used to obtain the G vs. a relationship (VCCT technique) under a specific load.
- The failure life (N_f) was then evaluated by integrating a the Paris law between initial and final crack lengths, which was determined by the crack length at which the G reached the fracture toughness G_{IC}.
- Different stress level was then analysed to produce the S-N curves and compared with the experimental result.

This method is a powerful procedure which is potentially applicable to many common joint types, including hybrid joints such as the pin-reinforced bonded joint. Thus, this method will be expanded to the current research project.

Damage mechanics based approaches are also widely used to predict fatigue crack propagation rate using the cohesive zone method (CZM). Moura [101] developed a cohesive zone based methodology to predict fatigue performance of bonded composites under mode II loading, rather than the fracture mechanic based approaches.

In this approach, fracture is characterized by a cohesive zone model with a single damage parameter. The evolution of this damage parameter was calculated by both static and fatigue damage. For the quasi-static loads, the damage parameter was evaluated by combining damage mechanics and fracture mechanics. Based on this, a relationship between damage evolution and da/dN was established to account for fatigue loading. The da/dN were measured experimentally and defined by the Paris law. Thus, this method is able to account for static and fatigue loads at the same time. This model links damage accumulation to the fatigue cycles automatically, while considering the energy release rate thresholds, load ratio R, and fracture mode mixity.

Since both VCCT and CZM within standard finite element method framework is not suitable to model matrix crack with arbitrary crack path, some methods have been developed that treat the discontinuity across the crack interface explicitly using the element formulation. By introducing extra degrees of freedom and enrichment functions, generalized finite element method (GFEM)

[169], extended finite element method (XFEM) [170-174] and phantom node methods (PNM) [175,176] have been developed based on the partition of unity method (PUM). Chen et al. [177-179] proposed the Floating Node Method (FNM), discontinuities are modeled locally within an element by partitioning the original finite element into sub-elements with the use of additional nodes. The main limitation of the above methods is the expensive computational cost due to additional DoFs or nodes.

Recently, Li and Chen [180, 181] proposed the Extended cohesive damage model (ECDM), which was develpted by introducing a cohesive damage model into the XFEM and then eliminating the enriched DoFs. Liu et al. [182-184] presented an augmented finite element method (AFEM) without the need of additional degree of freedom (DoFs) or phantom nodes. Four or three internal nodes are introduced to explain displacement jump at the beginning, the DoFs associated with these internal nodes will be condensed at an elemental level and there were no internal nodes present in the final form. Both ECDM and AFEM can effectively predict arbitrary delamination migration and accurately predict multi-crack initiation and propagation on a laminated composite

Nevertheless, the focus of this PhD is about long crack propagation and effect of z-pins to reduce crack growth rates. There is a lead crack in the specimens, which is a key assumption of the thesis, in order to focus on model development of z-pinned structures. Since VCCT is good for lead crack under linear elastic conditions, it is therefore chosen to calculate strain energy release rate and simulate crack propagation for this PhD.

In this PhD, fracture mechanics based fatigue life prediction is to be achieved by means of the finite element method by software ABAQUS for evaluating the relationship between strain energy release rate (G) and crack length (a), and also for numerical integration of the Paris law between the initial and critical crack lengths using the crack growth data generated by testing standard geometry (e.g. the double cantilever beam specimen).

2.3 Pin-reinforced laminates and joints

Z-pins is invented to improve the fracture toughness on composite laminates. The application of z-pins

are then extended to composite bonded joint to improve through thickness strength properties with only a moderate raise in fabrication expense. Compared to bolts and rivets, z-pin reinforced bonded joints induces less stress concentrations.

2.3.1 "Z-pins" in composite laminates

The so-called z-pin is a thin rod made from materials with high strength and high stiffness (e.g. titanium alloy, or fibrous carbon composite). Typically, the z-pins density within the composite structure range from 0.5 to 4.0 %, which is sufficient to provide significant improvement of through-thickness properties [102]. Each z-pin acts as a fine nail that locks the laminate plies together (Fig. 2-12). Existing pinning practices are limited to pins of diameter 0.25 mm (carbon fiber pin) and greater, but developing pining techniques with smaller diameter in the future could have significant improvement in both static and fatigue performance.

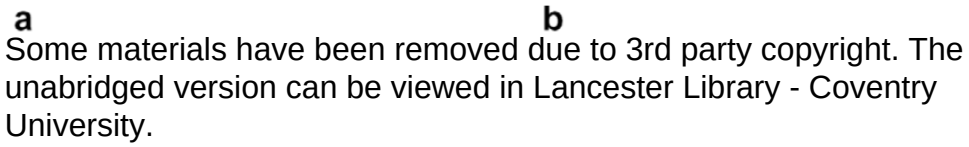

Fig. 2-12 (a) the size of typical z-pin, (b) z-pins inside a prepreg composite. [102]

Several methods have been developed to insert the z-pins and orient to the correct place, since their invention in the 1970s. The early insertion methods involved pushing every pin into the prepreg manually [103, 104], which is time-consuming and potentially inaccurate. In the 1980s [105], a semi-automated insert method was developed by using foam bed, which is collapsible and contains z-pins. Those foam bed was then placed at the top of the laminated prepregs, and inserted by curing pressure and acoustic vibration inside the autoclave.

Later, Aztex developed the UAZ (Ultrasonically Assisted Z- Fiber) method which became the most common process in current use [106]. This method is capable of rapid insertion of a large number of z-pins (Fig. 2-13). Recently, Song [107] and workers improved the efficiency by proposing a numerical-control multi-pin inserting system (based on UAZ technique), which is capable of inserting several pins into polymer foam synchronously.

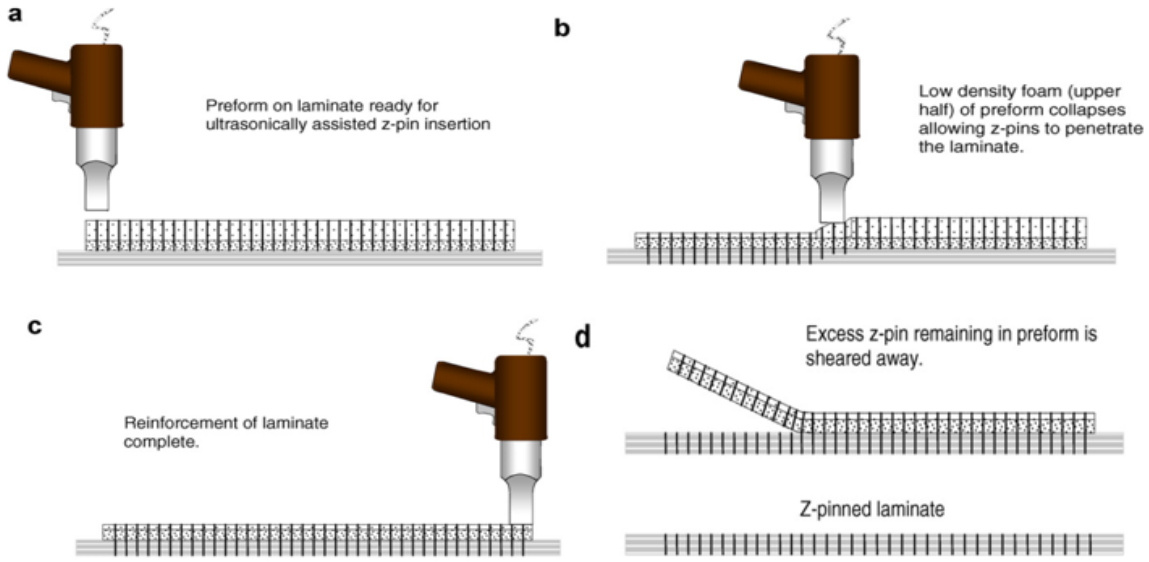

Fig. 2-13 Schematic of the UAZ process [102]

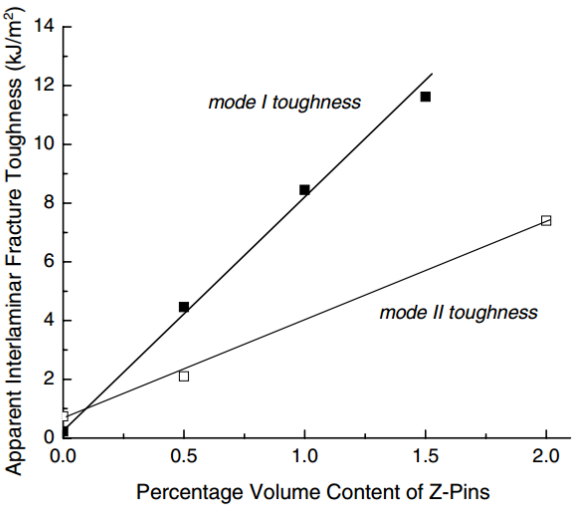

Fig. 2-14 Effect of z-pin on the modes I [117] and II [118] fracture toughness values for composite materials

A large number of studies revealed that z-pins is unable to prevent crack initation [109-114], but crack propagation is effectively constrained under a variety of different loading condition [109-116].

Fig. 2-14 shows that mode I and mode II fracture toughness improved linearly with the volume content of z-pins [117, 118]. This also indicates that z-pins are less competent at inhibiting mode II loading than mode I loading.

2.3.2 "Z-pins" in composite joints

The mechanism of bond failure which involves bonded plies being pulled apart suggests that the concept of z-pins can be extended to composite bonded joint to improve through thickness strength properties. Instead of using a few large bolts to reinforce a bonded composite joint, using many small pins causes less stress concentration. In addition, z-pins are capable of transforming propagation of a crack from an erratic to steady process, and therefore better loading sharing capacity can be achieved between the adhesive and mechanical bonds [113].

Several joint configurations reinforced with z-pins have been investigated in literature. Chang [119] carried out experimental static and fatigue tests of a pin reinforced single lap joint configuration (Fig. 2-15). The ultimate shear strength of pinned lap joints was up to 41% higher than that of the unpinned joints, and stable crack propagation is observed instead of fast fracture for unpinned specimens. Heimbs [120] proposed an innovative through-thickness reinforcement (metal arrow pins) to a typical T-pull test as shown in Fig. 2-16. Considerable improvements in failure strength was reported for pinned specimens.

Fig. 2-15 pin reinforced single lap joint configuration in [119]

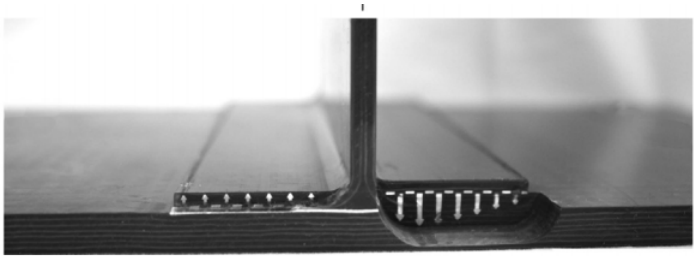

Fig. 2-16 pin reinforced T joint configuration in [120]

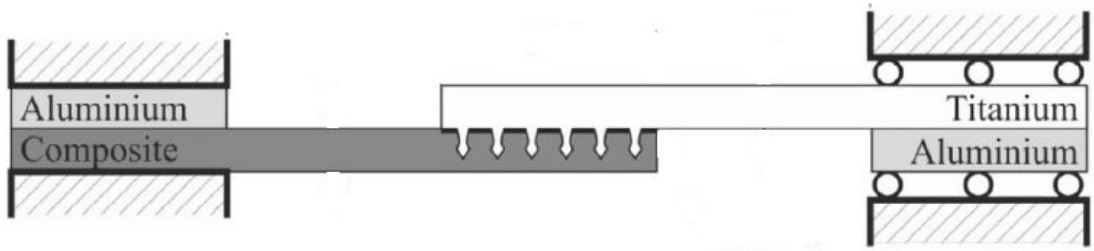

Fig. 2-17 an example of pin reinforced joint [20]

Ji [121] investigated the improvement of z-pins on hat joints under mode I loading. The ultimate failure strength increased by up to 27% at a 1,000,000-cycle loading by the presence of pins. Parkes [20] proposed a novel metal-composite joining technique, which reinforces toughness by small pins (Fig. 2-17). According to the experimental test, the ultimate strength increases by 6.5 times compared with unpinned joint.

2.3.3 Fatigue performance of z-pinned structure

The effect of z-pins on composites laminates and joints under fatigue loading has been experimentally investigated by many researchers. Research in [15] shown that z-pins bridging mechanism under fatigue loading is similar to the static loading. Z-pin reinforced carbon-epoxy composite were tested under both mode I and mode II cyclic loading. The results showed that z-pins are less competent at inhibiting mode II loading than mode I loading. However, a large-scale crack bridging zone (Fig. 2-18) is formed for both mode I and mode II loading, which generated high traction loads against crack propagation. Thus, fatigue performance increased linearly with the volume content of pins for both fracture mode.

Zhang et al. [122] experimentally studied the influence of z-pin diameter on the fatigue performance of z-pinned composits. This research found that for a constant areal density of pins, the bridging force generated by small diameter pin degraded slower than those with large diameter, for both debonding and friction stage.

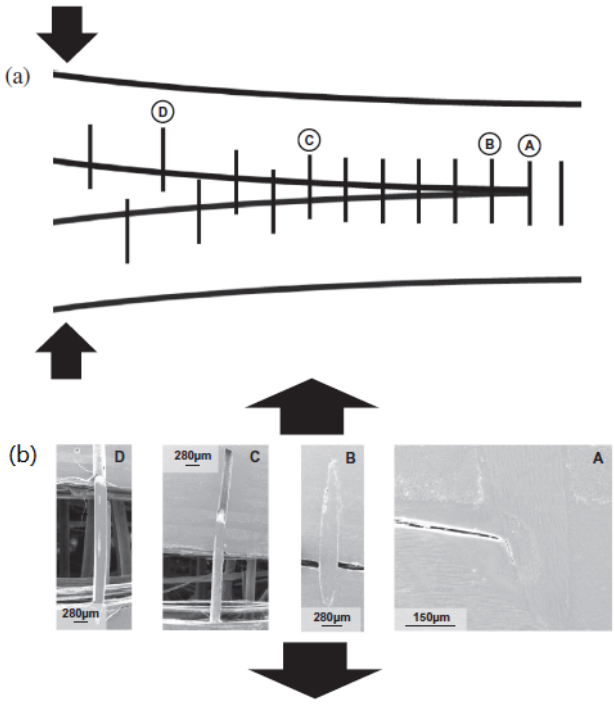

Fig. 2-18 The delamination fatigue cracks in z-pinned composites under mode I loading [15], (a) schematics (b) micrographs

A larger diameter pin has a larger interface between the pin and the laminates, than a smaller diameter pin, which has a greater probability of containing more and larger existing flaws, which propagate to form large interfacial cracks along the bond line during cyclic loading and ultimately cause pin debonding. Thus several smaller pins degrade slower under cyclic loading than a single large pin.

Pegorin, F. et al. [123] experimentally investigated the effect of z-pin length (2 mm, 4 mm and 8 mm) under mode I and mode II static and cyclic loading. For z-pinned composites subjected to mode I loading, the critical toughness improved considerably with the z-pin length increase from 2mm to 4mm. The load-displacement curve measured in the mode I test can be simplified in Fig. 2-19.

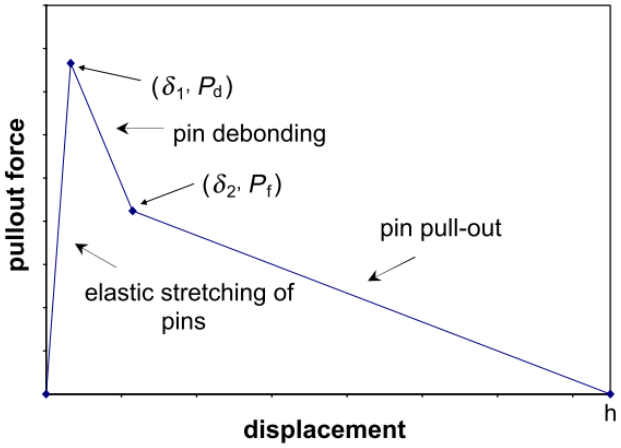

Fig. 2-19 A typical tri-linear constitutive law for single z-pin [123]

The single pin experienced three stages:

- z-pins first experienced elastic stretching,
- once the shear failure strength reached (the peak debond force P_d at δ_1), Z-pins started to debond
- once debonding was completed (the peak frictional force P_f at δ_2), the z-pins were completely pulled-out from the laminates, resisted only by friction.

According to the equation presented in this paper, traction load for all three stages increase with z-pin length, which match the experimental result well. However, only a small increase was found when the length increased from 4mm to 8mm. This is due to the fact that increasing the z-pin length eventually comes to a status by which multiple cracks propagations are more likely to occur. The exact locations and crack lengths are difficult to predict since they are functions of microscopic imperfections, such behaviour should be avoided in FE analysis on the author's PhD project.

Fig. 2-20 Z-pinning procedure on the composite hat joint [121]

Ji [121] experimentally investigated the z-pinned composite hat joints subjected to pull-off cyclic loading. In this study, the z-pins were made of STS 304 stainless steel with 0.5mm diameter and 5.7mm length. In order to reduce the damage induced by z-pinning process, conventional foam were replaced by thin acrylic moulds (Fig. 2-20). Compared to an unpinned hat joint, the fatigue strength of z-pinned joint improved by a factor of up to 48% after a 10^6cycle loading.

Son et al. [124] and Ko [125] experimentally studied the temperature effects on the fatigue performance of a metal pinned composite lap joint. Both standard metal pins and jagged metal pins were tested, and jagged pins results showed good improvement compared with standard pins and unpinned joint.

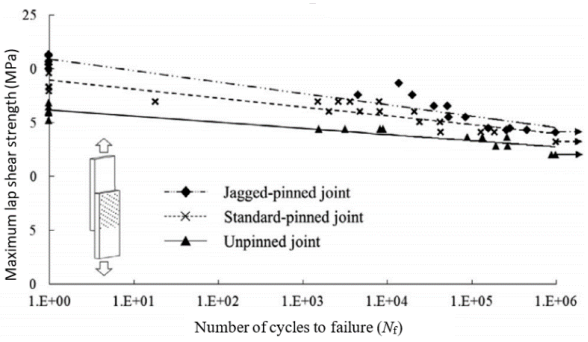

Fig. 2-21 Improvement of z-pins on S-N curve

Chang and Mouritz [126] investigated the z-pinned composite single lap joint under cyclic loading with different volume fraction of z-pins.

Fig. 2-22 Z-pinned lap joint under cyclic loading for different volume content of z-pins [126]

As shown in Fig. 2-22, the fatigue strength of z-pinned joints is 90% of static strength at 10^6 life cycles, which is significantly higher than those joints without reinforcement (75 of static strength). When the z-pin volume fraction increased to 4%, reduced fatigue strength is observed due to the fiber distortion which damage the in-plane property of the laminate. Thus, there is an optimal z-pin volume fraction beyond which more pin content actually begins to degrade fatigue life.

2.3.4 Prediction method of z-pinned structure under static load

Accompanying the increasing development of z-pins, many constitutive models of single Z-pin which describe the traction load vs. crack opening displacement relation have been developed in open literature, including empirical models [118], [144], analytical models [18], [143], [148], and numerical models [145], [150], [168]. Those constitutive models are then implemented to analytical solution or FE analysis to simulate z-pinned structure under static loading.

Several empirical models have been eshtablished in open literature, which is defined by an empirical traction load vs. crack opening displacement curve, attained by fitting experimental data of single pin pullout test. Ratcliffe and O'Brien [144] applied a bi-linear empirical constitutive model to an

analytical solution to predict the response of z-pinned DCB specimens. Cartié et al [118] derived an empirical pull out law from single Z-pin tests to predict mechanic response of a z-pinned T-joints.

Empirical models are the most direct method which can be used to predict z-pinned structure subjected to constant mode mixity loading (mode I, mode II or a fixed mode mixity). However, real structure are often subjected to variable mode mixty loading along with crack propagation. Thus, predict those structure by empirical model would be difficult and time-consuming. To this end, many researches focus on formulating analytical models for single z-pin.

Cox and Sridhar [18] developed a mixed mode traction law using an analytical micro-mechanical model. By varying the equilibrium equations of boundary conditions. This traction law can link the crack opening displacements to the bridging forces for many through-thickness reinforcement architectures, including z-pins. Grassi and Zhang [19] then applied Cox's micro-mechanical solution to model the material behavior of z-pin reinforcement and, based on this approach, z-pinned laminates under mode I static loading was successfully modelled by FEM.

Allegri and Zhang [143] developed a fully analytical and explicit bridging law for individual z-pin which is adaptable to the most of commercial FE code. In this analytical single pin model, z-pin is assumed to be a perfectly rigid body which embedded in a Winkler's type elastic foundation representing the embedding composite laminate. This analytical model was then employed to the FE s to predict the response of tee and cruciform joint.

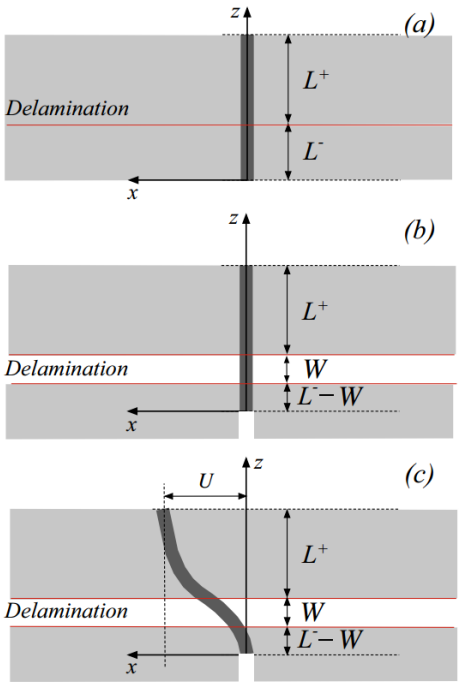

Fig. 2-23 Proposed bridging mechanism of a single pin [148]; (a) original configuration; (b) mode I; (c) mode II

Allegri Et al. [148] proposed a semi-analytical constitutive model which is described as Euler–Bernoulli beams undergoing small but finite rotations in an elastic foundation that represents surrounding composite laminate (Fig. 2-23). This model requires calibration of 6 parameters obtained by z-pins testes under a range of mode mixity, but the results shown good agreement for a wide range of mixed mode. Mohameda [147] employed this semi-analytical model to the cohesive element in FE analysis. Z-pin reinforced specimens have been simulated under mode I, mode II and mixed mode loading. The predicted load-displacement curve shows good agreement with experiments.

The traction forces generated by z-pins are affected by many factors, including z-pin mechanical and physical properties, manufacturing conditions (e.g. curing temperature, incline angel), and interfacial conditions. Due to the complexity of the z-pin bridging nature, numerical models were also established as an alternative solution.

Fig. 2-24 (a) schematic of single pin pullout test: (b) unit-cell model in FEA [145]

Bianchi and Zhang [145] developed a multi-scale modelling approach to predict a z-pinned DCB under static loading. Cohesive elements at pin region is used to model the z-pinned DCB geometry, by deriving the cohesive parameters from a unit-cell model of the single pin pull-out test (Fig. 2-24). This approach was then extended to mode II [150] and mixed mode [168] loading conditions.

2.3.5 Single pin bridging mechanism under fatigue loading

When the pin-reinforced structure is subjected to cyclic loading, the interface between the pin and resin is gradually worn out. Therefore, the bridging force generated by composite/z-pins interface is degraded with increasing fatigue cycles. A fatigue prediction that does not take account of this degradation will not be accurate, and the degradation must therefore be fully defined before the fatigue prediction.

To predict the fatigue life of pin-reinforced joint, degradation law of z-pin under fatigue loading is essential. Two papers have considered this degradation of the pin interface, and provide a possible law for the degradation [127, 128] based on the experimental finding.

Zhang [127] first proposed a micromechanics model for evaluating the reduction of bridging force (debonding and friction pull-out forces) under mode I fatigue loading, which is based on the fatigue data and experimental data from cyclic z-pin pull out tests (Fig. 2-25). In this model, the peak traction force of the z-pins which represents the composite/z-pins interface is degraded with increasing fatigue cycles.

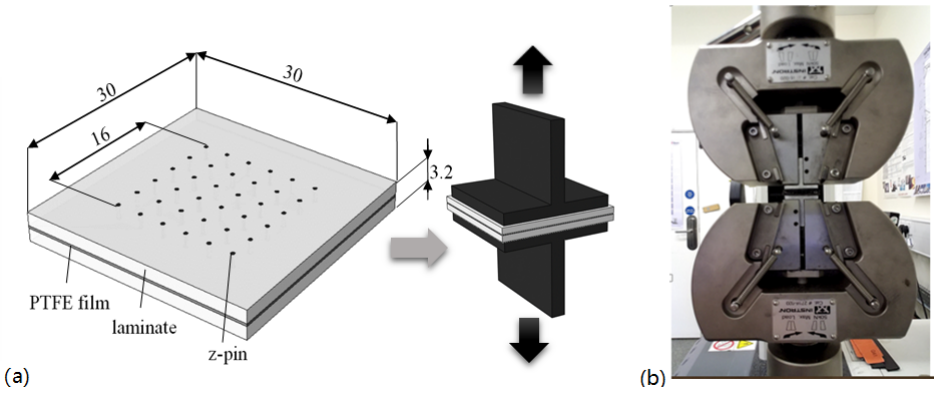

Fig. 2-25 Mode I pin pull-out test (a) test specimens geometry and mounting jigs (b) test fixture in test machine

Fig. 2-26 Pull-out load–displacement curves with different load cycles [127]

According to the experimental data, the maximum debonding load (P_d) and friction load (P_f), both reduced with an increasing number of load cycles due to the accumulation of fatigue-induced damage (e.g., micro- cracks) along the interface (Fig. 2-26).

In addition, tested specimen with larger applied displacement exhibit faster degradation due to the faster rate of damage accumulation along the pin bond-line (Fig. 2-27).

Fig. 2-27 Normalised debonding force degraded with numbers of cycles [127]

Fig. 2-28 A simplified tri-linear bridging law for z-pin (under static load)

This paper assumed a tri-linear bridging law function (Fig. 2-28) in which the parameters P_{d} and P_{f} degrade with the magnitude of cyclic z-pin displacement δ_{max} and number of cycle N as shown in equation (2-2) and (2-3).

$$P_d(\delta_{max}, N) = P_{d0}(\log N)^{-\beta\delta_{max}/\delta_1} \tag{2-2}$$

$$P_f(\delta_{max}, N) = P_{f0}(\log N)^{-\beta\delta_{max}/\delta_1} \tag{2-3}$$

where β is a fitting parameter based on experimental data.

However, this equation does not consider the displacement amplitude $\Delta\delta$, which is not a realistic

simplification. Another limitation is that the accumulated model is numerically incorrect (e.g. at the same displacement condition, the damage factors for 1000 cycles and 500 ×2 cycles are not identical).

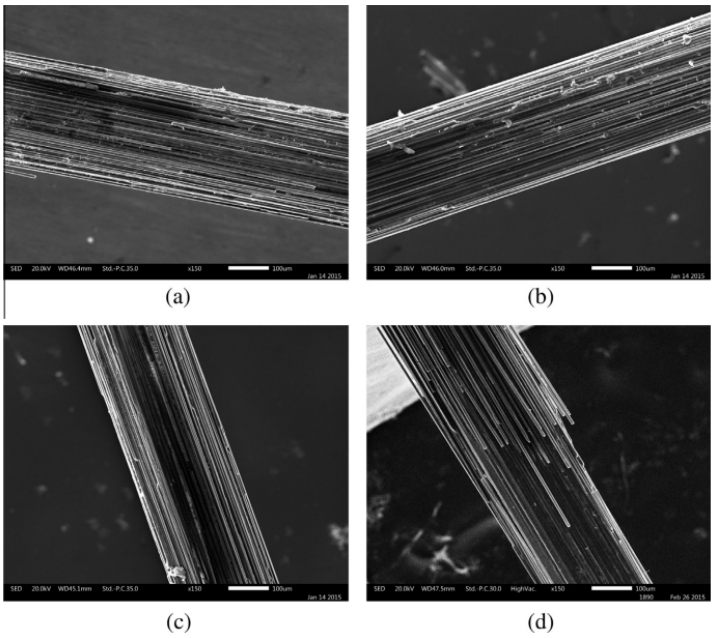

Fig. 2-29 Micrographs from Warzok et al [128] which show surface section of pins for (a) static test, (b) δ_0=3 mm, $\Delta\delta$= 0.05 mm and n =10^5, (c) δ_0=3 mm, $\Delta\delta$= 0.8 mm and n =10^5, (d) δ_0=1.5mm, $\Delta\delta$= 0.8 mm and n =10^6.

Warzok et al [128] experimentally studied the effect of different fatigue parameters on single z-pin. For mode I, it was shown that the degradation of pin behaviour during fatigue is mostly affected by the applied displacement amplitude and that the degradation is primarily caused by surface wear (Fig. 2-29). After their experimental investigation Warzok et al. [128] developed a phenomenological model to describe the degradation of energy dissipation per cycle D_{EF} and link it to the reduction of residual energy during pull-out D_E. The reduction of energy dissipation was then expressed via a power law:

$$D_{EF} = 1 - n^{-k} \tag{2-4}$$

According to the experimental results presented by Warzok [128], k depends on both δ_0 and $\Delta\delta$, therefore a linear relation is assumed in this paper:

$$k = k_{\delta_0} + k_{\Delta\delta} \tag{2-5}$$

Where k_{δ_0} and $k_{\Delta\delta}$ are experimentally determined exponent k

In Warzok's model, both the displacement amplitude $\Delta\delta$ and the average displacement δ_0 are considered, and thus overcomes one of the inherent limitations of Zhang's model [127]. However, comparison of the predictions against experimental data shows that the formula overestimates the degradation before 5×10^4 cycles and predicts a different trend to that shown by the experiment data (Fig. 2-30b). Furthermore, Warzok's model does not consider bonding behavior and does not provide an accumulated degradation model to account for degradation under variable displacement conditions.

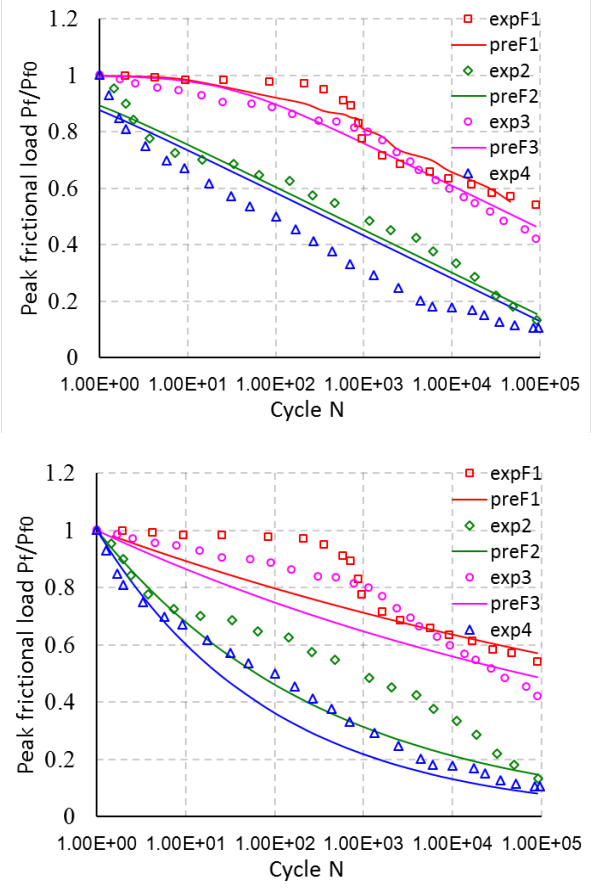

Fig. 2-30 Friction degradation prediction by (a) This model (b) Literature model [128]

2.4 Summary of literature survey

In this literature survey, both mechanical fastening and adhesive bonding have been reviewed, covering typical joining types, possible failure modes, experimental tests and prediction methods (analytical and numerical). When the components are fastened by bonding, the structure is vulnerable

to through-thickness damage such as impact and delamination due to the absence of fasteners. To improve through-thickness properties, several hybrid methods have been reviewed. Among those methods, pin-reinforced bonded joints were found to be very promising and their development in now widespread. Instead of using bolts to reinforce bonded composite joint, small pins (z-pins) cause less stress concentration while providing better load sharing compared to bolt/ bonded joint. A large number of experimental studies have shown that z-pins can significantly improve properties in laminate in the through-thickness direction, and similar trends were found in analytical and numerical studies of z-pin reinforced joints.

Current literature regarding fatigue failure shows that many studies have been made of fatigue in both mechanical fastening and adhesively bonded joints, including fatigue crack growth tests, evaluation of fatigue strength, retardation and repair of fatigue cracks.

Fatigue performance of z-pinned laminates and joints has been the subject of many experimental studies. For mode I fatigue tests (e.g. DCB), fatigue lifetime considerably increased with the presence of z-pins. However, for Mode II fatigue testing, z-pins only provided moderate improvements at low and high cyclic shear stress conditions. Over most of the ΔG_{II} range, there was only a small improvement in the fatigue resistance with z-pinning.

Several published papers have reported studies to predict the fatigue lifetime of composite materials and bonded composite joints. Both phenomenological based approaches and progressive damage based approaches have been used to investigate the fatigue behavior of adhesively bonded joints. The phenomenological based approach is widely applied to experimentally investigate the effect of joint geometry, laminate layout and test environment, whilst the progressive damage based approach (used in conjunction with the FEA method) are more applicable to predict the fatigue life of adhesively bonded joints as well as hybrid joints which are the main focus of the current research project.

For pin reinforced bonded joints, some methods have been developed to predict z-pinned laminates and joints under static loads. However, no literature was found to predict the fatigue life of these structures. Thus, the main novelty of the current research is to expand the progressive damage based

approach to predict the fatigue life of pin reinforced bonded joints, using either fracture mechanic based technique (VCCT) or damage mechanic based technique (CZM).

3. Theories and modelling techniques used in this thesis

3.1 Linear Elastic Fracture Mechanics

In this research, a fracture mechanics based methodology is used since it is able to predict delamination growth behaviour from the crack initiated to the crack finally failure, and the *G* based Paris law is established with available data from testing standard configurations, e.g. DCB, ENF.

3.1.1 Crack driving force

During the fracture mechanics based fatigue analysis, fatigue crack growth rate is normally linked to the stress intensity factor *K* or strain energy release rate *G*. The stress intensity factor *K* is usually applied to isotropic materials, e.g. metals, calculated by equation (3-1):

$$K = Y\sigma_r\sqrt{\pi a} \tag{3-1}$$

where *Y* is a geometry parameter, σ_r is the remote applied stress, *a* is usually the half crack length.

For composite materials, *G* is usually used, defined as

$$G = -\frac{\partial(U-V)}{\partial A} \tag{3-2}$$

where U is the potential energy accessible for crack propagation, V is the work for all external forces acting, and A is the crack extension area.

For a double-ended crack within an infinite solid, the rate of release in strain energy per crack tip is

$$G = \frac{2\pi a\sigma^2}{E} \tag{3-3}$$

For isotropic materials, G can be related to K by eq. 3-3:

$$G = \frac{K^2}{E} \tag{3-4}$$

where *E* stands for the elastic Young's modulus and v stands for the Poisson's ratio. In practice, a condition of plane strain is more usual, in which case one must include the factor ($1-v^2$) in the numerator.

3.1.2 Fracture criteria (static load) single or mixed mode

The basic failure criteria for linear elastic fracture mechanics is to compare the value of crack driving force K or G (determined by analytical solution or FEM) with the material fracture toughness K_C or G_C (determined by experiments). Under static load, crack will grow when:

$$G \geq G_C \tag{3-5}$$

Depend on the applied displacement condition, three basic fracture modes can be defined by: opening displacement (mode I), in-plane shear displacement (mode II), out of plane shear displacement (mode III). (Fig. 3-1). The growth of a delamination crack might occur under any one of these modes, or (as is more likely in real world applications) under a combination of all three modes.

To evaluate the propagation of damage under different combinations of loading, many "mixed mode" failure criteria have been proposed. Two well-known criteria were selected from the literature (the Power Law criterion [129] and the Benzeggagh and Kenane (B&K) criterion[130]) and these were used for mixed mode investigations in this study. The Power Law criterion [129] is one of the early and popular criteria which established an interaction between G_I/G_{IC}, G_{II}/G_{IIC} and G_{III}/G_{IIIC}:

$$\left(\frac{G_I}{G_{IC}}\right)^{\alpha}+\left(\frac{G_{II}}{G_{IIC}}\right)^{\beta}+\left(\frac{G_{III}}{G_{IIIC}}\right)^{\gamma} \geq 1 \tag{3-6}$$

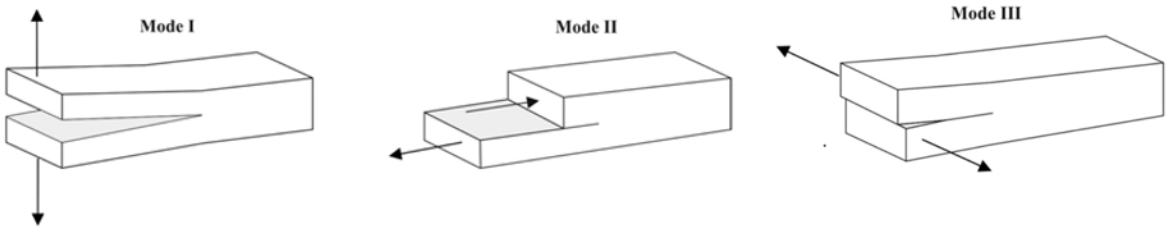

Fig. 3-1 Typical fracture modes (a) opening displacement (mode I), (b) in-plane shear displacement (mode II)and (c) out of plane shear displacement (mode III)

To describe this failure criterion, six fitting parameters are required where: α, β and γ are the e xponents, and G_{IC}, $G_{IIC}$and G_{IIIC} are the fracture toughness.

Another commonly used mixed mode law are develpoed by Benzeggagh and Kenane [130], whose

criterion has been shown to fit well with mixed-mode I + II experimental data. The total energy release rate $G_T = G_I + G_{II}$ is expressed as a function of the ratio G_{II}/G_T:

$$\frac{G_T}{G_{IC}+(G_{IIC}-G_{IC})\left(\frac{G_{II}}{G_T}\right)^{\eta}} \geq 1 \tag{3-7}$$

Reeder [131] proposed a linear interpolation governs the interaction between these two modes:

$$\frac{G_T}{G_{IC}+((G_{IIC}-G_{IC})\left(\frac{G_{II}}{G_T}\right)+(G_{IIIC}-G_{IC})\left(\frac{G_{III}}{G_T}\right))\left(\frac{G_{II}+G_{III}}{G_T}\right)^{\eta-1}} \geq 1 \tag{3-8}$$

where the total energy release rate is expressed as $G_T = G_I + G_{II} + G_{III}$ and the terms G_{IC}, $G_{IIC}$and $G_{IIIC}$and η are material parameters used to fit the experimental data.

3.1.3 Basic mode fracture tests

(a) Mode I

The Double Cantilever Beam (DCB) geometry is commonly tested to evaluate the mode I strain energy release rate and fatigue crack growth rate data (Fig. 3-2). During manufacture, a thermal insulated film is inserted to the mid-plane of DCB to initiate delamination. The pull-out displacement is applied to the end of DCB by hinges (Fig. 3-2a) or by loading blocks (Fig. 3-2b) while the load and delamination length are recorded (Fig. 3-2c).

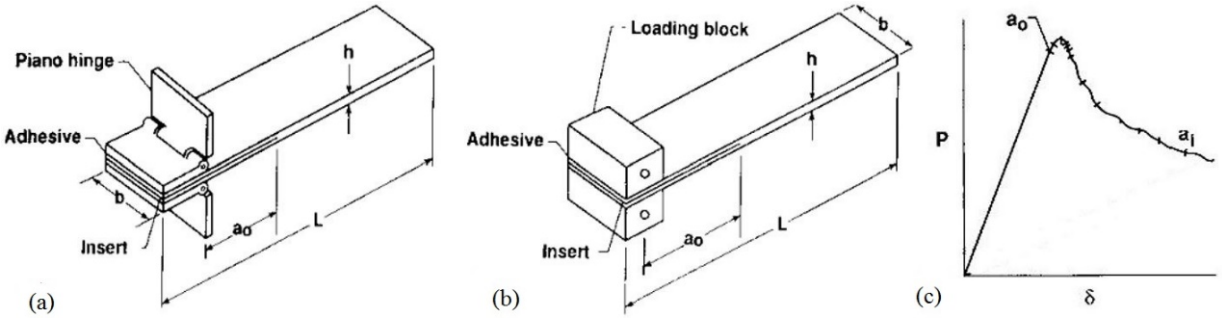

Fig. 3-2 DCB specimens (a) with hinges (b) with loading blocks (c) typical load-displacement curve recorded [133]

The Mode I fracture toughness G_{IC} can be assessed by the Irwin–Kies equation [132]:

$$\mathrm{G}_I = \frac{P^2}{2b}\frac{dC}{da} \tag{3-9}$$

As recommended in ATSM D5528 [133], the equation is then rewritten by modified beam theory (3-10) or compliance calibration method (3-11):

$$G_I = \frac{3P\delta}{2b(a+|\Delta|)} \tag{3-10}$$

$$G_I = \frac{3P^2\delta^{2/3}}{2A_1bh} \tag{3-11}$$

where Δ are evaluated empirically by developing a least squares plot of the cube root of compliance, $C^{1/3}$, as a fuction of delamination length a (Fig. 3-3a), and where A_1 is the slope of a/h vs. $C^{1/3}$ curve (Fig. 3-3b)).

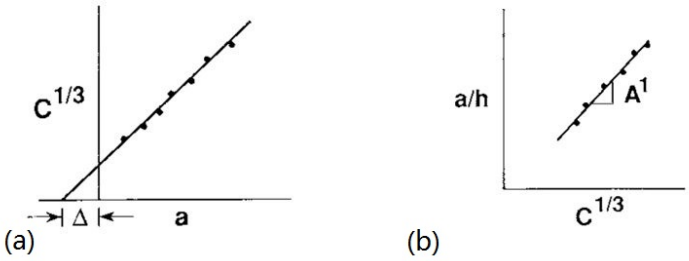

Fig. 3-3 (a) Modified Beam Theory (b) Modified Compliance Calibration as recommended in ATSM D5528 [133]

For fatigue crack growth data, the da/dN vs. ΔG data is then deduced from a vs. N data and a vs. G data.

(b) Mode II

The End-Notched Flexure (ENF) configuration Fig. 3-4 is used to evaluate the mode II strain energy release rate and fatigue crack growth rate data. A displacement is applied to the loading roller (Fig. 3-4a) while the load and delamination length (Fig. 3-4b) are recorded.

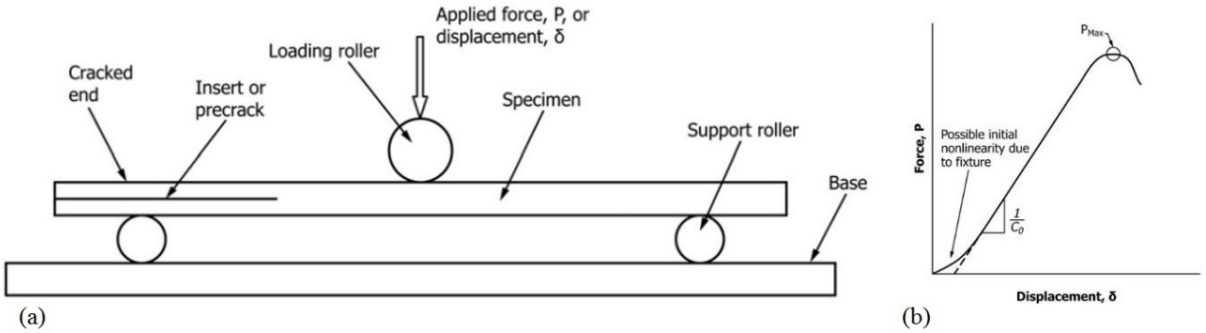

Fig. 3-4 (a) ENF test fixture and specimen, (b) typical load-displacement curve recorded

As recommended in ATSM D7905 [134], the mode II fracture toughness G_{IIC} can be evaluated by the compliance calibration method:

$$G_{IIC} = \frac{3mP_{Max}{}^2 a_0{}^2}{2B} \tag{3-12}$$

where m is the Compliance Calibration Coefficient, P_{Max} is the maximum force from the fracture test (Fig. 3-4b), a_0 is the initial crack length and B is the specimen width.

Fig. 3-5 Typical fit of compliance as a function of crack length for ENF fracture test in ATSM D7905 [134].

(c) Mixed mode I/II:

Some Mixed mode I/II tests have already been proposed in the literature, such as Asymmetrical Double Cantilever Beam (ADCB), Single Edge Notched Tensile (SENT) test, Constant Tension Shear (CTS) test. However, difficulties arise when attempting to use these tests to vary the mode ratio GI/GII

over a wide range. The mixed-mode bending test (MMB) designed by Reeder and Crews [129], is adaptable to a wide range of mode mixity (Fig. 3-6).

The G_I and G_{II} can be calculated by Equation (3-13) [135]:

$$\begin{cases} G_I = \frac{3a^2P^2}{4b^2Eb^3L^2}(3c-L)^2 \\ G_{II} = \frac{9a^2P^2}{16b^2Eb^3L^2}(c+L)^2 \end{cases} \quad (3\text{-}13)$$

Where the geometric parameters c and L are illustrated in Fig. 3-6.

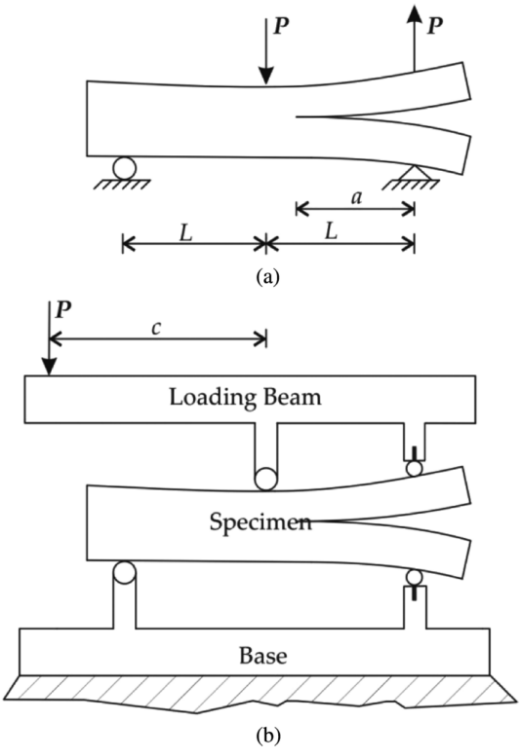

Fig. 3-6 (a) MMB specimen and (b) Test method schematics

3.2 Virtual Crack Closure Technique (VCCT)

The Virtual Crack Closure Technique (VCCT) was first presented in 1977 by Rybicki and Kanninen [136] for cracks in linear elastic, homogeneous and isotropic material. It was extended to model crack propagation in composite materials, and is based on the Griffith strain energy release rate. When the crack increases by a small increment Δa (compared to the total crack length a), the energy required to close the corresponding crack Δa can be calculated by VCCT [137]:

$$\begin{cases} G_I = -Z_i'(w_i' - w_{i^*}')/(2\Delta ab) \\ G_{II} = -X_i'(u_i' - u_{i^*}')/(2\Delta ab) \\ G_{III} = -Y_i'(v_i' - v_{i^*}')/(2\Delta ab) \end{cases} \quad (3\text{-}14)$$

where X_i', Y_i', Z_i' are the nodal forces at the crack front, i and w_i', u_i', v_i' are the corresponding displacements of nodal points l and l* (

Fig. 3-7).

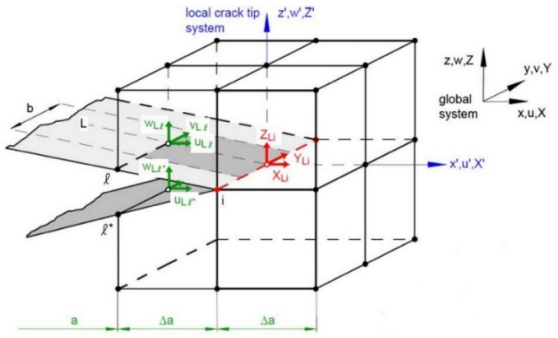

Fig. 3-7 Virtual crack closure technique (VCCT)

The VCCT is also implemented into FE code Abaqus as a procedure for determining the crack front propagation. As discussed by Krueger [137], Abaqus will automatically define shape of crack front once the crack front nodes are determined. In every analysis increment, strain energy release rates are evaluated by VCCT and the crack propagation will occurs if Eq. (3-5, 3-6, 3-7, 3-8) are satisfied. The crack propagation is achieved by releasing the constraint at the crack tip node.

It should be noted that VCCT is a linear elastic fracture mechanics based approach. It needs a starter crack for analysis. When the crack tip experiences plastic yielding, the above concepts, based purely on the theory of elasticity, are not valid. However, this limitation of the VCCT are of limited relevance to the current study since the delamination of composites are usually treated as elastic analyses and modelled by VCCT method [185-187]. This is even true for fatigue delamination in which the applied cyclic loading is relatively small. In addition, plastic zone size of a typical composite DCB used in this thesis (Section 6.1) is calculated to demonstrate whether the elastic theory is appropriate for the current study.

$$l_{\mathrm{p}} = \left(\frac{P}{\sigma_y b} - \frac{1}{\lambda}\right) + \frac{1}{\sigma_y b}\sqrt{P^2 + 2Pa\sigma_y b} \tag{3-15}$$

Where the l_{p}, P , σ_y, a is the plastic zone size, applied load, yield strength of resin (60 MPa assumed) and crack length respectively, and λ is a function of several material parameters (full details can be found in [188], which is beyond the scope of this thesis).

According to Fig. 3-8, for both static and fatigue load magnitudes, the plastic zone size are small enough compared to the crack length ($l_{\mathrm{p}} \leq a/50$), and therefore elastic theory is sufficient for this study.

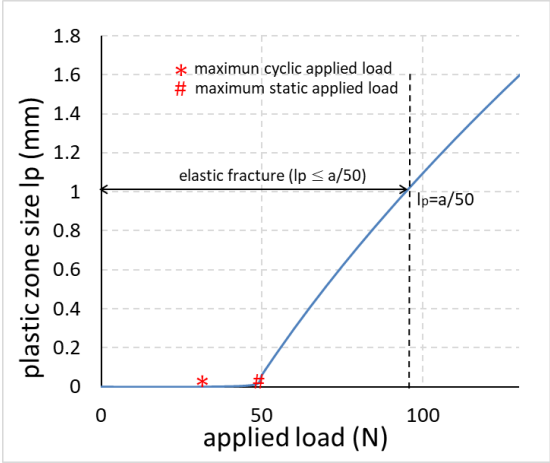

Fig. 3-8 plastic zone size vs. applied load curve for the DCB used in Section

Furthermore, study on [189] suggested that plastic dissipation remains a negligible value throughout the crack propagation phase for a yielding adhesively bonded joints (with thick adhesive layer). Thus, VCCT is chosen over J-integral method due to the numerical simplicity and effectiveness (without adaptive remeshing for moving delamination problems as used for J-integral method).

3.3 Cohesive Zone Model (CZM)

Some difficulties of the implementation of the VCCT into FE codes can to be overcome by using cohesive zone approach within a so-called cohesive element. In this research, cohesive elements are used to represent delamination propagation and bridging force generated by z-pins. Fig. 3-9 illustrate a typical bilinear traction-separation law.

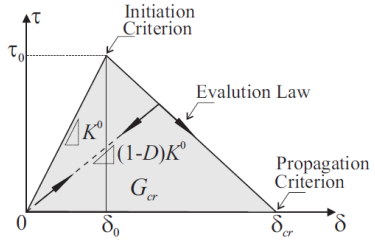

Fig. 3-9 Traction-separation law for typical cohesive element

The Traction-separation law is determined by three parameters, traction strength, τ_0, failure displacement at fracture (δ_{cr}), and the energy needed for opening the crack (G_{cr}).

For the initial part, linear elastic behavior is assumed, followed by the initiation and evolution of damage. The elastic behavior can then be written as:

$$\begin{Bmatrix} T_N \\ T_S \\ T_T \end{Bmatrix} = \begin{bmatrix} K_{NN} & K_{NS} & K_{NT} \\ K_{SN} & K_{SS} & K_{ST} \\ K_{TN} & K_{TS} & K_{TT} \end{bmatrix} \begin{Bmatrix} \delta_N \\ \delta_S \\ \delta_T \end{Bmatrix} \tag{3-16}$$

where the subscripts N, S and T is "normal", "shear" and "tear"; K_{ij} is the component of stiffness matrix.

When either the stress or strain within the cohesive zone satisfy a specified damage initiation criterion, damage evolution occurs and described by a damage parameter D. The reduction of the stiffness can be calculated below:

$$T = (1 - D)[T][\delta] \tag{3-17}$$

Once the area under the traction-separation curve (G_d) is identical to the fracture toughness (G_c), the local cohesive zone is completely failed and the cohesive element can be removed that corresponds to complete fracture of the interface between layers and is considered as delamination propagation.

Although CZM has been widely used in composite fracture analysis, the major drawback is that it requires the potential crack path be known prior to the analysis, so that CZM elements can be directly implanted along the path. This greatly limits the application of CZM for simulating arbitrary crack growth and multi-crack propagations. Another shortcoming of the CZM is that requests suitable parameters in nonlinear solvers to obtain convergent solutions (as discussed later in Section 6.2.1).

3.4 Nonlinear FEM in fracture analysis

Simulating crack propagation in composites is a nonlinear iteration process. The most commonly used solution technique in nonlinear finite element (FE) codes is the Newton-Raphson (NR) method [190]. In the NR procedure, the applied load is divided into small increments, and the displacement increment within each step is computed by using the tangent stiffness matrix. The resistant force can be calculated by accumulated displacement, and the out-of-balance force vector can be determined as the difference between the applied and the resistant forces. When both the out-of-balance force and the residual displacements are less than a specified tolerance, convergence is assumed to be obtained. If convergence criteria are not satisfied, the residual force vector is re-evaluated (the stiffness matrix is updated) and thus a new solution is obtained. This iterative procedure continues until the problem converges, then next load increment is applied. NR method is effective, but it is computationally expensive for large finite element codes, because the tangent stiffness matrix must be formed and solved at each iteration.

The most commonly used alternative to Newton is the modified Newton method [191], in which the tangent stiffness matrix is only updated occasionally. This method is attractive for mildly nonlinear problems involving softening behavior (such as contained plasticity with monotonic straining) but is not suitable for severely nonlinear cases. In addition, Quasi-Newton methods such as BFGS [192] and Crisfield [193], are also among the most widely used Newton type methods for improving the convergence properties with a modest computational effort. The tangent matrix is computed in the first iteration of each step and in subsequent iterations is obtained by a secant approximation rather than re-evaluating it at every iteration. Speeding up these iterative methods can be done by line search algorithm [194], which attempt to stabilize NR iterations by shrinking or expanding the current displacement increment to minimize the resulting out-of balance forces and/or residual displacements. The line search algorithm is effective if the prediction is far from the equilibrium, e.g., if strong nonlinearities take place.

4. Development of predictive models for Z-pinned laminates and joints

In this Chapter, a series of predictive models is established to predict the z-pin reinforced composites under mode I fatigue loading.

4.1 Modelling strategy of z-pinned laminates and joints under static loading

Early approaches applied nonlinear spring elements on the delamination surfaces to model the bridging behavior of z-pins [142-144]. Recently, Bianchi [145] extended the second approach to a multi-scale modelling approach, and the load-displacement relations are in good agreement with the experimental test. In this research, the prediction under static loading follows similar approach proposed by Bianchi [145], with some minor modification (VCCT implemented for the evaluation of crack driving force *G*). The multi-scale modelling strategy developed by Bianchi [145] includes two scales (Fig. 4-1).

At the meso-scale level, the bridging force exerted by an individual pin is obtained using a unit-cell model (by the finite element method or experimental test). The interface between upper and lower adherends is assumed completely failed and the pin bridging is the only feature connecting the two parts. After pull-out, the load-displacement curve was then idealised as a bilinear traction-separation law (TSL) of cohesive elements.

Fig. 4-1 Multi-scale modelling approach: (a) single pin model (b) multiple “single pin” models embedded in global model. Sketch is copied from Bianchi [145]

At the macro-scale, cohesive elements are applied to the pin region representing the bridging force

generated by individual pins. For the bonding area between adherends, Virtual Crack Closure Technique (VCCT) is used to evaluate the strain energy release rate, which is the crack driving force for the fracture mechanics based fatigue life prediction approach.

4.2 Constitutive model for individual Z-pin subjected to static mode I loading

Many constitutive models of single Z-pin which describe the traction load vs. crack opening displacement relation have been developed in open literature, including analytical models [143], [148], empirical models [142], [144]. Due to the complexity of the z-pin bridging nature, numerical models were also established as an alternative solution [149-151].

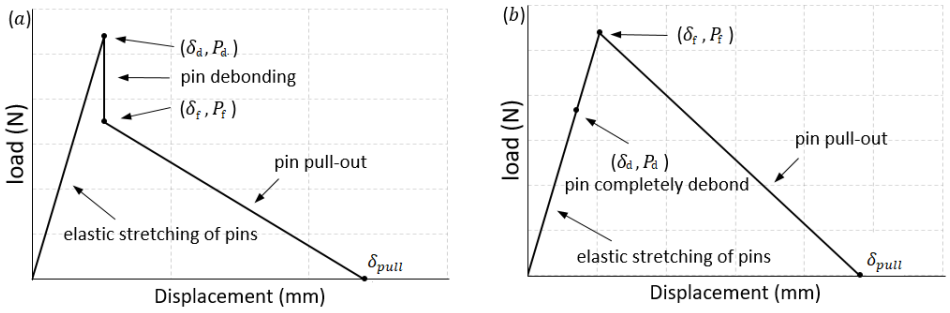

Fig. 4-2 Load-displacement curve of pin pull-out test (a) tri-linear curve (b) bi-linear curve

The scope of this research is limited to mode I loading, thus, pins pull-out test is performed, empirically or numerically. The typical results from experiment or numerical simulation under mode I loading can be simplified to tri-linear (Fig. 4-2a) or bi-linear (Fig. 4-2b) curve.

When a pinned structure is only subject to static loading, the choice of tri-linear or bi-linear bridging relationship does not affect the prediction significantly as long as the energy absorption (i.e. the area under the bridging curve) is close to the actual value. However, in fatigue analysis, the loading history is equally important as energy absorption. Thus, the choice of whether to use a tri-linear or bi-linear bridging law should depend on experimental observation.

A tri-linear constitutive model (Fig. 4-2a) between the bridging force and z-pin displacement can be described as follow:

$$P = \begin{cases} \frac{\delta}{\delta_d} P_d & (0 \le \delta \le \delta_d) \\ \frac{\delta_f - \delta}{\delta_f - \delta_d} P_d + \frac{\delta - \delta_d}{\delta_f - \delta_d} P_f & (\delta_d \le \delta \le \delta_f) \\ P_f + \frac{\delta_f - \delta}{\delta_{pull} - \delta_f} P_f & (\delta_f \le \delta \le \delta_{pull}) \end{cases} \quad (4\text{-}1)$$

where P the current bridging force, P_{d} the peak debonding load, P_{f} the peak frictional load, and their corresponding displacements (δ, δ_d, δ_f), and δ_{pull} the pull-out displacement of pin.

For the bi-linear case (Fig. 4-2b), after the interface is fully debonded, an increase of load is caused before pull-out due to the higher friction strength. The bi-linear constitutive model can be defined as:

$$P = \begin{cases} \frac{\delta}{\delta_f} P_f & (0 \le \delta \le \delta_f) \\ P_f + \frac{\delta_f - \delta}{\delta_{pull} - \delta_f} P_f & (\delta_f \le \delta \le \delta_{pull}) \end{cases} \quad (4\text{-}2)$$

The reason for the different load-displacement curves found in experiments and simulations is mostly due to the different debond strength. This is affected by many factors, inlcuding: the pin/laminate material, surface treatment, and environment conditions during pin insert process. For most metal z-pins founded in literature, the debond strength is lower than the friction strength, and therefore a bi-linear relation is preferred. However, laminate reinforced with carbon pins and pins with chemical surface treatments can experience higher debond strengths and consequently behave in a tri-linear relationship.

The cohesive law parameters used in FEA were then deduced from the average load vs. displacement data.

$$T_d = \frac{P_d}{A_{pin}} \quad \text{or} \quad T_f = \frac{P_f}{A_{pin}} \quad (4\text{-}3)$$

where A_{pin} is the cross section area for one pin, and the T is the bridging strength in the cohesive law and P_{d}, P_{f} are the peak debond and frictional loads, respectively.

In this research, empirical constitutive model which is based on the test results of pins pull-out test is developed and is implemented to FE analysis to simulate z-pinned DCB in Section 7.2. Numerical model is also developed for the prediction of z-pinned hat joint in Section 7.3.

Empirical model for single pin constitutive relation

To characterize the constitutive model of a single z-pin under mode I loading, a laminate with multiple z-pins was manufactured for a "pin pull-out test" (Fig. 4-3).

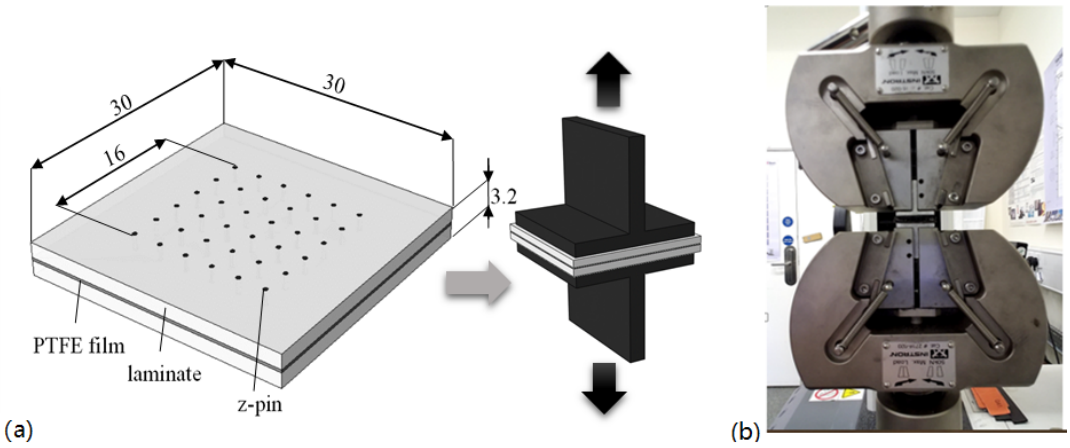

Fig. 4-3Mode I pin pull-out test (a) test specimens geometry and mounting jigs (b) test fixture in test machine

A thermal insulated film was inserted between the upper and lower Laminates to avoid any adhesive bonding between them so that only the pin bridging force is measured. Through-thickness tensile test was conducted (i.e. the "pin pull-out test") and the load obtained from the pull-out test was then divided by the total number of pins in the specimen to determine the average traction load per pin.

Numerical model for single pin constitutive relation

The bridging force exerted by a single pin under mode I loading can be estimated by FE analysis (Fig. 4-4). According to the microscopic observations of z-pinned material, a resin-rich pocket around the pin occurs due to pin insertion. Thus, the material surrounding the pin is assumed to behave as homogeneous and isotropic resin and is modelled using the elastic properties of the resin (as the same used in [145]). The interface between the upper and lower laminates is assumed be completely failed and the pin bridging the only feature connecting the two parts.

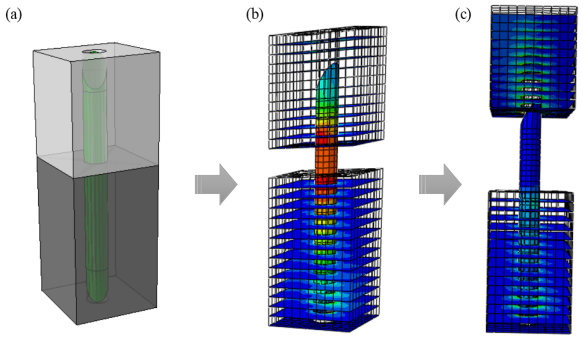

Fig. 4-4 Unit-cell model of single pin pull-out test (a) FE model, (b) stress on pin during frictional pull-out, (c) pin is completely pulled-out of the top stiffener

Before the pullout simulation, a temperature change from cure to room conditions was applied to simulate the curing process and the thermal residual stresses were then calculated and saved in the model as the initial condition. This initial contact stress causes friction resistance when a pullout load is applied. (i.e. maximum shear force proportional to the contact pressure). For the pullout simulation, a surface to surface contact is applied to the pin/laminate interface with a friction coefficient $\mu = 0.75$ (as the same used in Francesco's work [145]). Finally, a pull-out force is applied under the displacement controlled loading until the pin is completely pulled out.

There are several limitations to this model:

Firstly, this model assumed the pull-out resistance is considered being caused by the friction force only. This assumption are close to the bi-linear bridging law founded in experiment test. (When friction strength is higher than debond strength). As mentioned before, the debond strength affected by many factors such as the pin/ laminate material, surface treatment, and environment condition during pin insert process. Those factors are difficult to count in FE model and therefore this model is less accurate for carbon pins and pins which experience chemical surface treatment (debond strength higher than friction strength).

Secondly, the coefficient of friction cannot be determined by FE analysis and therefore experiment must be carried out to define the coefficient of friction before FE analysis. Finally, this model overestimates the stiffness during elastic phase since the plastic deformation of matrix occurs near pin

region are not considered in this FE model. Nonetheless, modelling the degradation of pin closure force as pin undergoes interfacial debond and frictional pull-out is of considerable value in understanding the micromechanics of the z-pin crack bridging.

4.3 Degradation law of single pin bridging force under fatigue loading

When a z-pinned structure is subjected to fatigue loading, the interface between the pin and resin is gradually worn out. Therefore, the bridging force generated by composite/z-pins interface is degraded with increasing fatigue cycles. A fatigue prediction that does not take account of this degradation will not be accurate, and the degradation must therefore be fully defined before the fatigue prediction.

To predict the fatigue life of pin-reinforced joint, degradation law of z-pin under fatigue loading is essential. Currently, there are two papers [122,128] that propose possible pin degradation laws based upon experimental data. Since the degradation laws in both papers [122,128] have limitations and present difficulties in application to the fatigue prediction procedure directly. A new degradation law is proposed which is based on damage mechanics model by Peerlings et al [152]. This degradation law was aimed to describe the high-cycle fatigue damage within the interface elements:

$$D = -\frac{1}{\alpha}\ln(1 - \frac{2\alpha c}{\beta+1}\varepsilon_a^{\beta+1}N) \tag{4-4}$$

where α, β, c are material parameters, and a constant strain amplitude ε_a was assumed.

To account for both cyclic displacement amplitude and mean displacement, the degradation law has now been modified to:

$$D = -\frac{1}{\alpha}\ln(1 - \frac{2\alpha c}{\beta+1}Nq^{\beta+1}r^d) \tag{4-5}$$

where α, β, c, d material parameters, μ and r are calculated by

$$q = \frac{\delta_a}{\delta_{pull}} \text{ or } q = \frac{\delta_a}{\delta_d} \tag{4-6}$$

$$r = \frac{\delta_m}{\delta_{pull}} \text{ or } r = \frac{\delta_m}{\delta_d} \tag{4-7}$$

where δ_a and δ_m are the cyclic displacement amplitude and mean displacement, respectively.

δ_{pull} is the failure displacement under static pull-out tests (frictional degradation law) and δ_d is the debond displacement (debond degradation law). The use of failure displacement normalizes the effect of pin length and therefore this law can be used in models with different pin lengths.

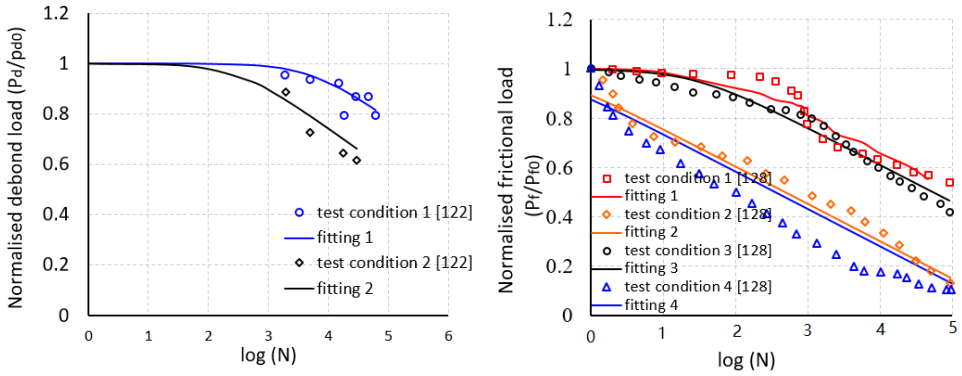

Fig. 4-5 Degradation law fitting (a) debonding data in [122] under two different displacement amplitude/ average displacement conditions (b) frictional data in[128] under four different displacement amplitude/ average displacement conditions. The detailed test conditions from [122] and [128] are shown in Table 4-1 and the smooth lines in the figures are the best fitted lines for determine the fitting parameters in eq. (4-5).

Table 4-1. Overview of the displacement controlled fatigue tests

Test condition	Experimental and input disp (mm)			Calculated ratios (eqs. 5-7)	
	δ_a	δ_m	δ_d	q	r
Debonding [16]					
Test 1	0.25	0.16	0.56	0.45	0.275
Test 2	0.41	0.25	0.56	0.72	0.44
Frictional [26]			δ_{pull}		
Test 1	0.1	0.15	4.5	0.022	0.033
Test 2	1.6	1.5	4.5	0.355	0.333
Test 3	0.1	3	4.5	0.022	0.667
Test 4	1.6	3	4.5	0.355	0.667

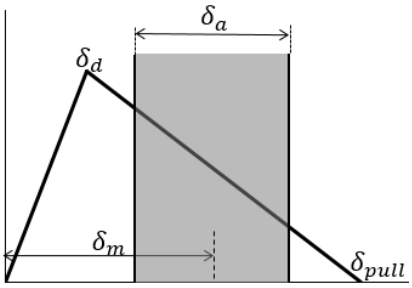

The normalized residual peak debond force and friction force (P_d/P_{d0} and P_f/P_{f0}) in [122] and [128] were transferred to the reduction parameter D as inputs in the fitting software:

$$D_d = 1 - P_d / P_{d0} \tag{4-8}$$

$$D_f = 1 - P_f / P_{f0} \tag{4-9}$$

where D_d , D_f are the accumulated reduction parameters calculated by the debond and frictional degradation laws, respectively.

The fitting parameters α, β, c, d for the debonding and frictional degradation laws have been calculated (Table 4-2) from the experimental data published in [122] and [128] (Fig. 4-5), by a numerical fitting code Auto2Fit. Auto2Fit is a powerful data analysis software, which is widely used in the areas of function optimization, equation solving, parameter estimation, and chart drawing. Typical Auto2Fit script and result are shown in Fig. 4-6 - Fig. 4-8.

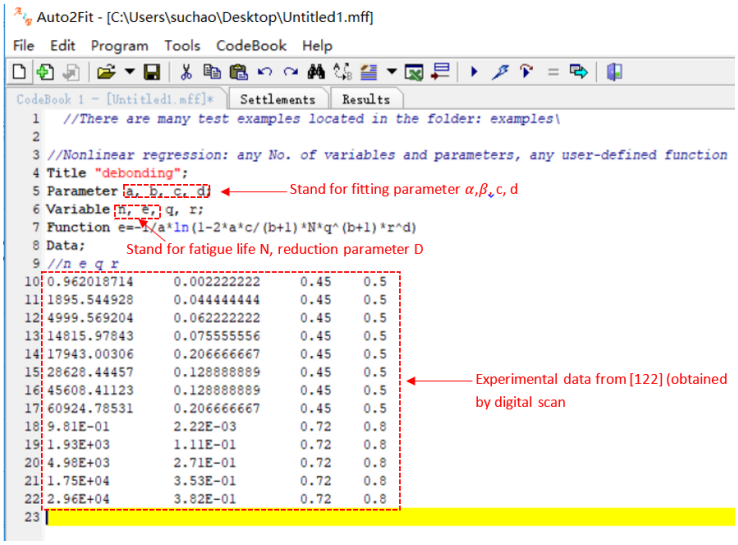

Fig. 4-6 Input script for fitting parameter calculation in Auto2Fit (debonding degradation)

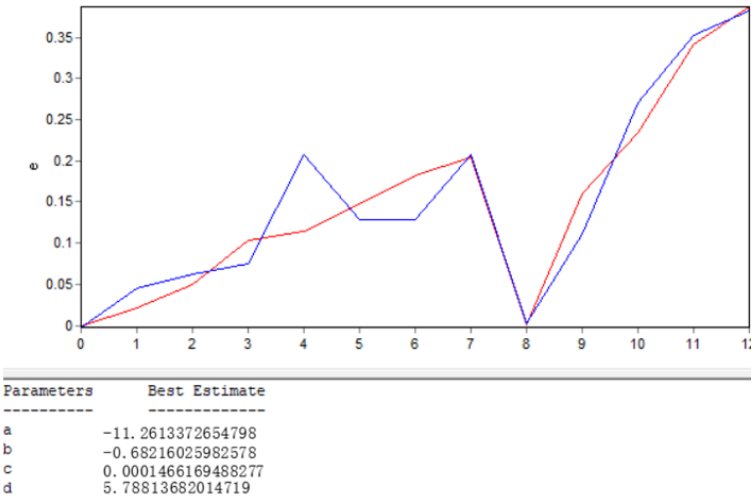

Fig. 4-7 Fitting result in Auto2Fit (debond degradation)

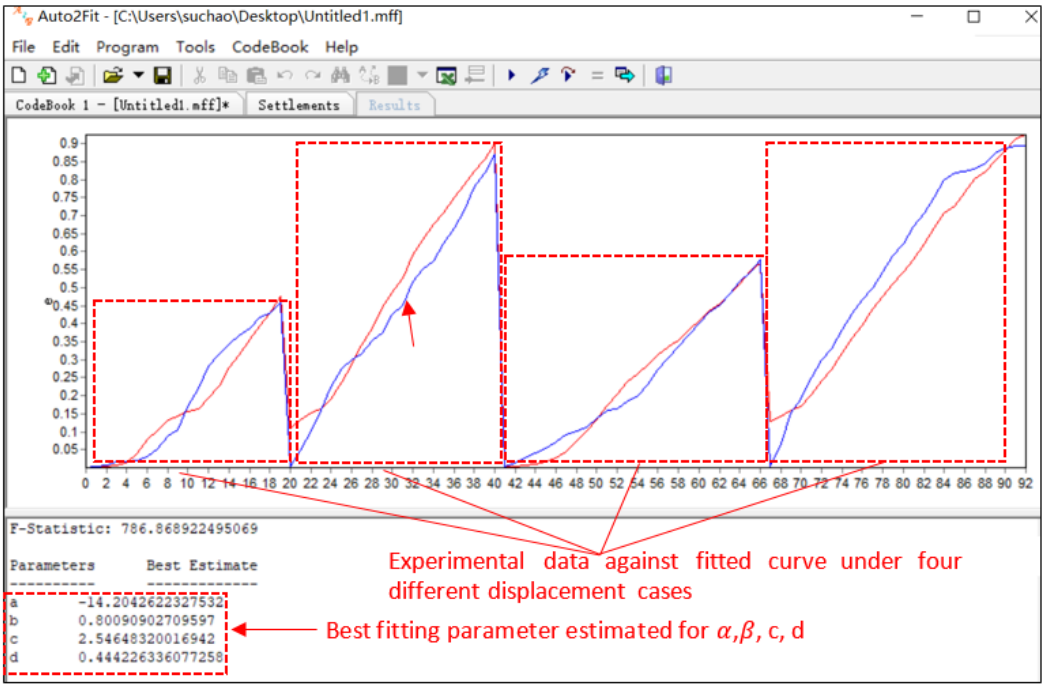

Fig. 4-8 Fitting result in Auto2Fit (frictional degradation)

The calculated values are presented in Table 4-2.

Table 4-2 Fitting parameters for degradation law

	α	β	c	d
Debonding [122]	-11.26	-0.68	0.000147	5.79
Frictional [128]	-14.19	0.79	2.51	0.443

These parameters can then be used in damage accumulation calculations. In i iteration, the number of cycles to failure N_{f_i} under displacement condition of q_i and r_i, is obtained by setting $D = 1$ and solving equation (4-5) for N, resulting in

$$N_{f_i} = \frac{(1-e^{-\alpha})}{\frac{2\alpha c}{\beta+1} q_i^{\beta+1} r_i^{d}} \tag{4-10}$$

Using expression (4-10) for the fatigue life, equation (4-5) can be rewritten in terms of the relative number of cycles N_i/N_{f_i}:

$$D_i = -\frac{1}{\alpha}\ln\left(1-(1-e^{-\alpha})\frac{N_i}{N_{f_i}}\right) \tag{4-11}$$

If a pin experiences damages D_i (i=1,…, k) for k sources, then the accumulated damage D_{acc} is calculated by

$$D_{acc} = -\frac{1}{\alpha}\ln\left(1-(1-e^{-\alpha})\sum_{i=1}^{k}\frac{N_i}{N_{f_i}}\right) \quad (4\text{-}12)$$

4.4 Constitutive model for individual z-pin subjected to fatigue mode I loading

To simplfy the single pin bridging behavior under fatigue loading, the prediction methodology described above assumes that debonding degradation behavior occurs first and is then followed by the frictional degradation (pin pull-out) behavior. The degradation of pin briding behaviour is described below.

Peak debond load degrades with increasing life cycles. The residual peak debond load P_{d} can be calculated by:

$$P_d = (1-D_d)\,P_{d0} \quad (4\text{-}13)$$

where D_{d} is the damage parameter calculated by the debond degradation law. The parameter in this law is fitted by pin's debond behavior observed in fatigue single pin pull-out test (Table 4-2).

According to the experimental data in [122], the slope of elastic stretching portion of the curve does not change during fatigue testing, indicating that the elastic modulus of the pins was not affected by fatigue. Thus, the corresponding displacements to the peak debonding force, δ_d also degrade with P_{d} proportionally:

$$\delta_d = (1-D_d)\,\delta_{d0} \quad (4\text{-}14)$$

The degradation of P_{d} and δ_d cause changes to the pin bridging law (i.e. the load vs. displacement response). A typical pin's bridging law under fatigue loading is illustrated by Fig. 4-9:

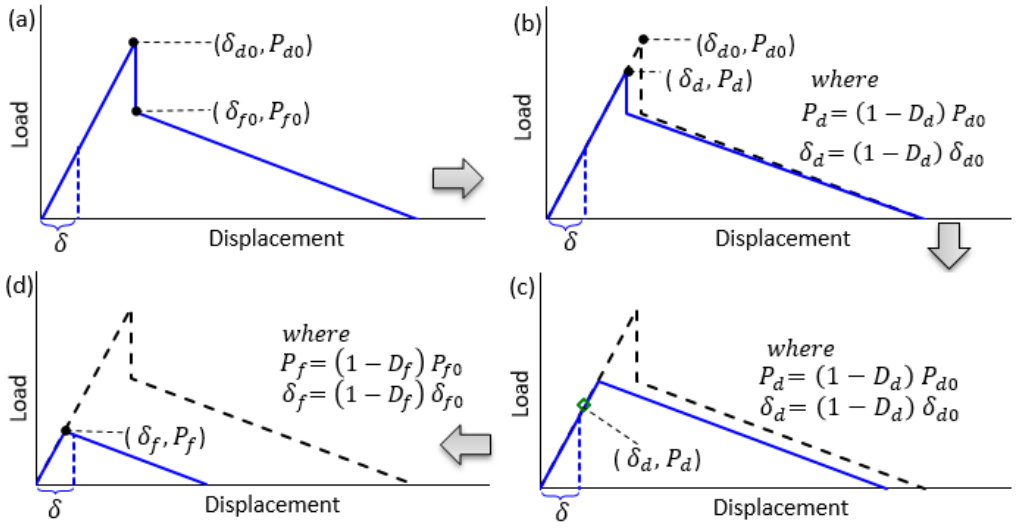

Fig. 4-9 Typical pin's bridging law under fatigue loading (a) initial stage (b) initially debonding degradation (D_{d}) of P_{d} and δ_d (c) continue debonding degradation (D_{d}) when applied displacement $\delta < \delta_d < \delta_{f0}$ (d) pin fully debonded, experience frictional degradation (D_{f})

The initial response is as shown in Fig. 4-9a, and this initially degrades as shown qualitatively by Fig. 4-9b. However, when the peak debond force P_{d} becomes lower than the frictional peak load P_{f} then the load displacement response becomes as shown in Fig. 4-9c. The pin is still assumed to experience further debonding degradation until the applied load exceeds peak debond force P_{d}, at which point the pin is fully debonded and begins to experience frictional degradation as shown in Fig. 4-9d. After that, the peak friction force P_{f} and failure displacement δ_{pull} degrade with increasing load cycles according to:

$$P_f = (1 - D_f)\, P_{f0} \tag{4-15}$$

$$\delta_{pull} = \left(1 - D_f\right) \delta_{pull\_0} \tag{4-16}$$

where D_{f} are the damage parameter calculated by frictional degradation law.

The full details of pin's bridging law under fatigue loading assumed in this work is illustrated by Fig. 4-10, which is calculated by excel code automatically.

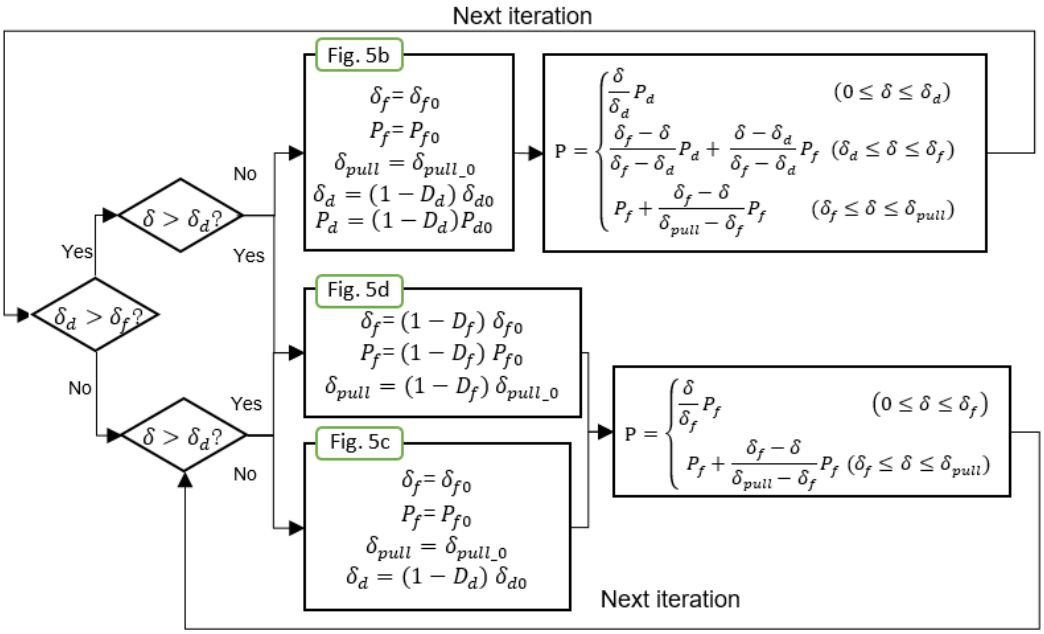

where δ, P the current applied displacement and bridging force

Fig. 4-10 Full details of pin's bridging law under fatigue loading

4.5 Fatigue life prediction framework

The prediction of fatigue crack propagation rate and life is achieved using the finite element method in conjunction with the measured crack growth rate in unreinforced laminate.

This procedure is illustrated in Fig. 4-11 and described as follows:

- Experimental tests of DCB specimens to generate crack growth rate data in mode I.
- Finite element analysis are used to obtain the strain energy release rate (G) as function of crack length (VCCT technique) under a specific load.
- Cohesive element at pin locations is used to represent the z-pin bridging forces. The input parameter within the FE model degraded with the load cycle number.
- The number of cycles to failure N_f was calculated by integrating a fatigue crack growth law (Paris law in this case) between initial and final crack lengths.
- The final crack length was calculated by the FE model when G reached the (static) fracture toughness G_{IC}

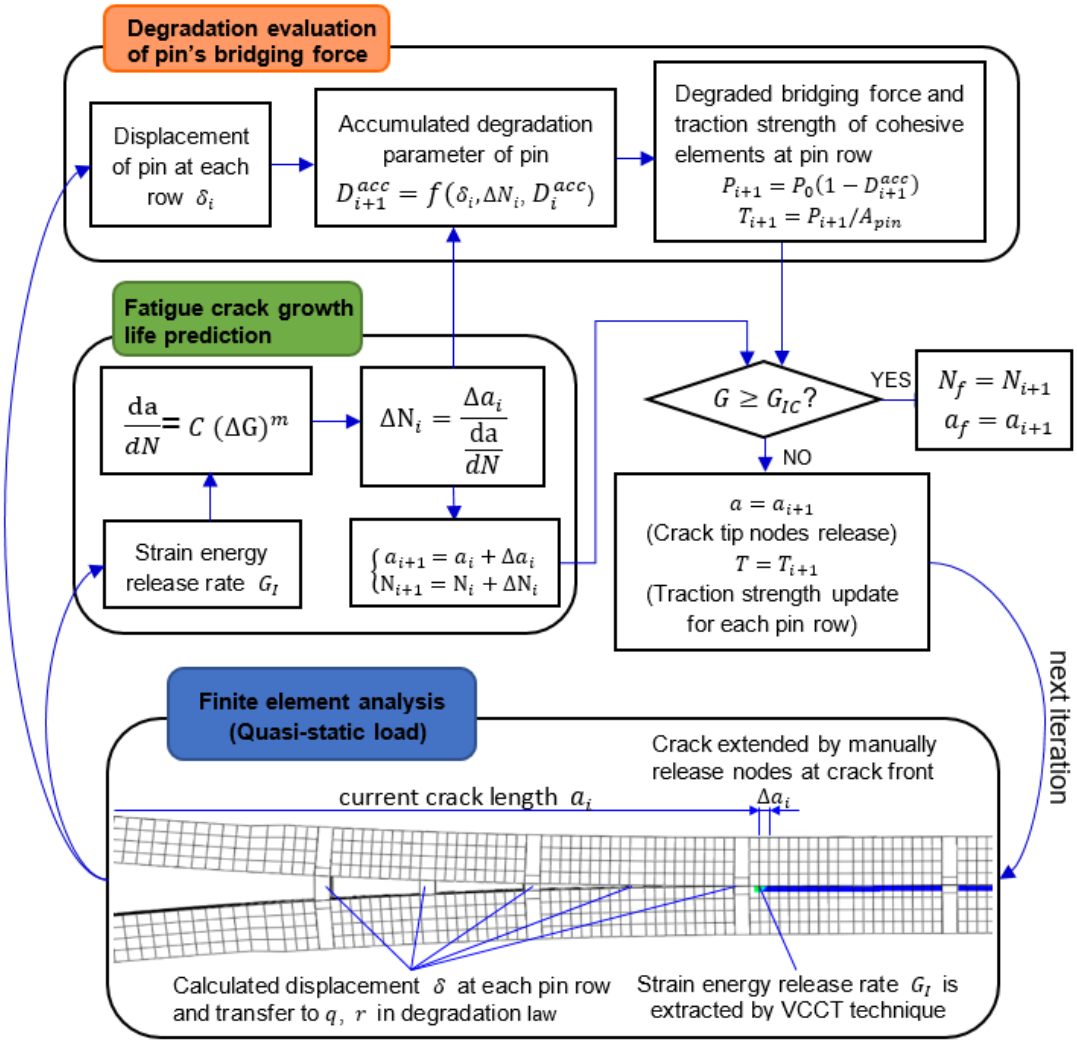

Fig. 4-11 Fatigue crack growth life prediction framework (for z-pinned laminate under mode I loading)

Since the degradation of bridging forces is also affected by the applied displacement amplitude, pin in different locations experienced different level of degradation (even though they have been subjected to the same number of cycle, *N*).

5 Experimental

In this section, pinned DCB specimens and pins pull-out test specimens are manufactured in Cranfield University's Composites Lab by technician and tested by the PhD candidate in Coventry University. The experiments were aimed to support validation of the prediction methodology developed in this PhD.

5.1 Specimen manufacture

5.1.1 Ply cutting and de-bulking for prepreg

Pinned DCB specimens were fabricated for both static and fatigue testing using AS7/8552 carbon-epoxy prepreg (supplied by Hexcel Composites Ltd) with a UD layup of $[0]_{24}$. The raw prepregs (Fig. 5-1a) were cut into small rectangular panel (Fig. 5-1b) and laid up in all 0° direction to form the UD stack sequence.

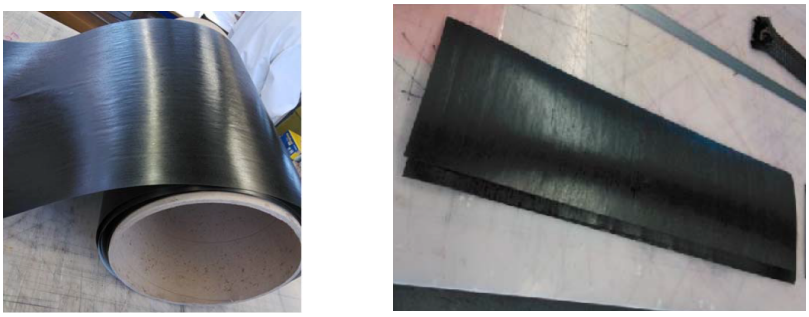

Fig. 5-1 Ply cutting from (a) Raw prepregs to (b) rectangular plane (500×220 mm)

During layup, UD prepregs were debulked every four plies to ensure there was no air bubble on the interface between each ply.

Fig. 5-2 De-bulking table for AS7/8552 prepreg

A thermal insulated film with a length of 50 mm was artificially inserted between two 12 ply laminate to create an initial delamination crack between the laminates. For the pin pull-out test specimens, the z-pins and prepregs were made of the same materials as were used for the DCB samples. A thermal insulated film was inserted between the upper and lower half of the laminate to avoid any adhesive bonding between the laminates.

5.1.2 Z-pinning process

The z-pins used were pultruded T300/BMI carbon fibers with diameter of 0.5mm, supplied in preforms (supplied by Aztex Inc) as shown in Fig. 5-3a. The length of the Z-pins used was enough to pin the required thickness each time. For both DCB and pins pull-out specimen, the z-pins were inserted using an ultrasonic hammer with the pin areal density of 2% defined by the percentage of the total preform or resulting laminate area covered by Z-pins.

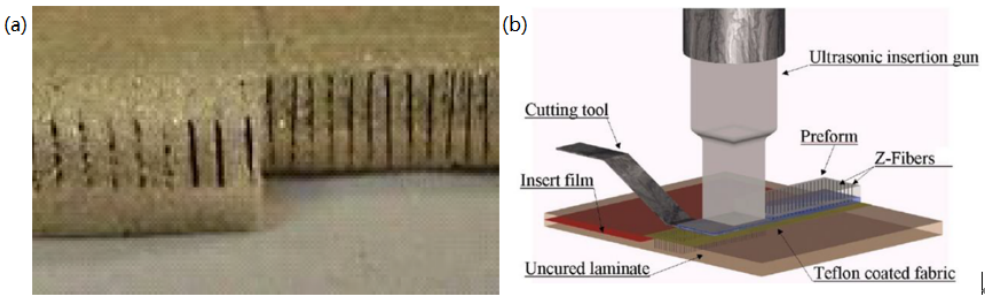

Fig. 5-3 (a) z-pin preforms and (b) ultrasonically assisted pinning (UAZ) process

Before insertion, a film of Teflon coated glass fabric is placed between the laminate and the Z-pin preform to prevent the z-pins from moving which led to pins misalignment. To soften the resin sufficiently to allow an easier passage through for the z-pins, the prepreg stack was heating up on a hot plate till the temperate increased to 60°. The z-pins were inserted through the uncured prepreg stack using the ultrasonically assisted pinning (UAZ) process.

5.1.3 Curing

Before curing, peel-ply and bleeder sheets were attached to the laminates with Teflon film to prevent them sticking to the laminate (Fig. 5-4). The peel-ply is used to achieve the required surface finish on

the laminates, and the bleeder sheets was used to absorb the excess resin from the laminates.

The top side of laminate was then covered by a porous continuous vent cloth which provides a path for volatiles to escape when the vacuum is applied and promotes a uniform distribution of vacuum. In the bottom side, a strip of the cork–rubber material is applied along each edge of the panel to prevent lateral motion of the panel. Finally, the prepreg was placed on an aluminium plate (Fig. 5-5a) and covered by a vacuum bag (Fig. 5-5b) and is ready for consolidating and curing in an autoclave (Fig. 5-5c).

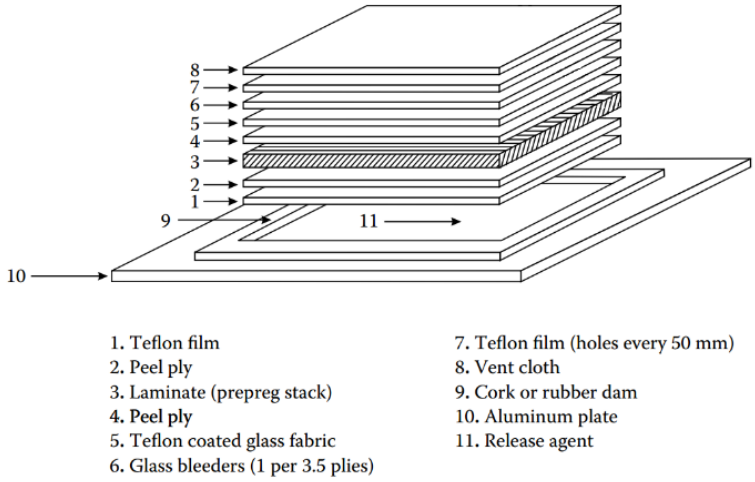

Fig. 5-4 The vacuum bag layup sequence for the prepreg composite

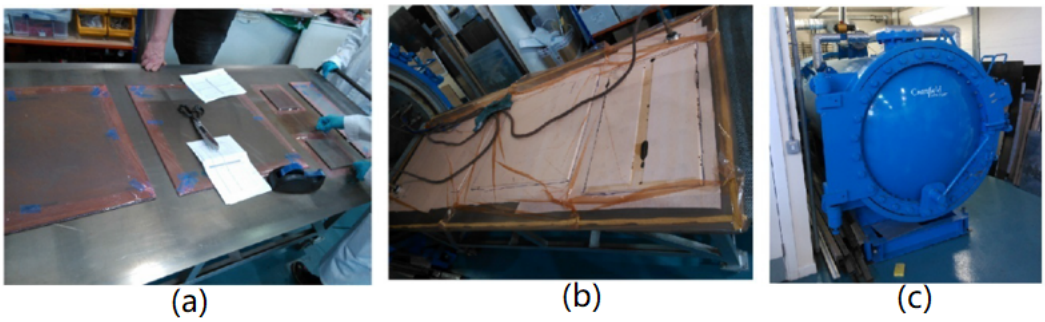

Fig. 5-5 (a) additional layup for curing (b) covered with vacuum bag (c) autoclave used in Cranfield University

During curing, the temperature was controlled and illustrated in Fig. 5-6.

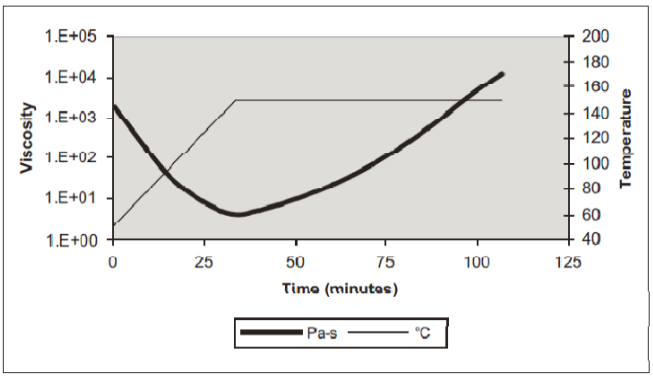

Fig. 5-6 Temperature control for curing

The cured specimens were then bonded with two T-shaped loading tabs made of aluminium alloy.

5.2 Specimen geometrics

The z-pinned DCB geometry is shown in Fig. 5-7. During specimen manufacture, the pin-reinforced area is 12 mm away from the initial crack tip and extending for 25 mm length covers the entire specimen width, with a pin spacing of 3.2mm.

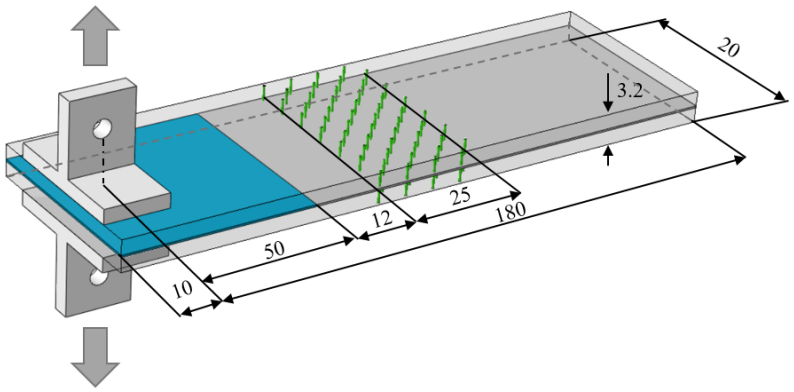

Fig. 5-7 Geometry and dimension of z-pinned DCB specimen

To characterize the mode-I bridging law of a single z-pin, a laminate with 6×6 z-pins was manufactured for a “pin pull-out test” (Fig. 5-8). The specimen was 30 mm×30 mm with a thickness of 3.2 mm.

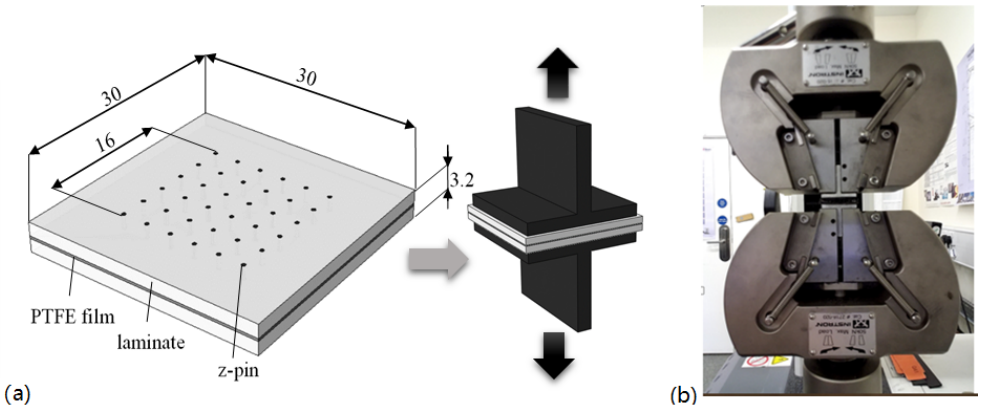

Fig. 5-8 Mode I pin pull-out test (a) test specimens geometry and mounting jigs (b) test fixture in test machine

A through-thickness tensile test was conducted (i.e. the "pin pull-out test") and the load obtained from the pull-out test was then divided by the total number of pins in the specimen (36) to determine the average traction load per pin.

5.3 Test method

Table 5-1 summarizes the tests performed in this work. Static tests of pinned DCB specimens and tensile pin pull-out tests were conducted on a 50 kN electro-servo mechanical machine (Instron 3369) under a displacement-controlled loading rate of 1 mm/min and 0.5 mm/min respectively.

The fatigue tests of pinned DCB were conducted under displacement-controlled load (3Hz) with a load ratio of 0.1. Two groups of fatigue tests were carried out in which the applied cyclic displacement amplitude was either 80% or 90% of the displacement at peak load under static test (d_{Pmax}). The reason for such high cyclic displacement amplitude selected is mostly due to the strong fatigue resistant on z-pinned region. An attempt has been made with 70% of d_{Pmax}, when the crack reach pin area, the propegation stoped for a entire week (more than 2,000,000). For each test condition, three samples were tested. To minimize the thickness effect on crack length as reported in Section 4.2, specimens with thickness of 1.70±0.02mm were selected for fatigue testing.

A separate compliance test was carried out to exclude the compliance of test machine. Furthermore, two tabs were adhesively bonded together and were tested to exclude the deformation of the

tab-to-specimen adhesive during the pin pull-out tests.

Table 5-1 Summary of tests

Specimen	Load	Test condition	No. of tests	Loading rate / Frequency	Specimen No.	Half thickness (mm)
Pin pull-out	Static	Displacement control	3	0.5 mm/min	SP1, SP2, SP3	1.68-1.85
Pinned DCB	Static	Displacement control	3	1 mm/min	S1, S2, S3	1.62-1.78
Pinned DCB	Fatigue	Maximum disp. = 22.7mm (80% d_{Pmax})	3	3 Hz	F1-1, F1-2, F1-3	1.70±0.02
Pinned DCB	Fatigue	Maximum disp. = 25.7mm (90% d_{Pmax})	3	3 Hz	F2-1, F2-2, F2-3	1.70±0.02

6. Validation of predictive models

In this chapter, VCCT modelling approach was first validated by unpinned DCB (Mode I) and ENF (Mode II) specimens in terms of load-displacement curve. To confidently predict fatigue crack growth life in future studies, strain energy release rate (G) must be accurately extracted by VCCT method. This was also verified in unpinned DCB and ENF by the simple beam theory in term of G vs. a relationship. By manually extending the crack length (nodal release method) in FE model, the value of G can be attained by the VCCT method for each crack length increment.

The CZM method was then validated in pin-reinforced DCB and ENF specimens by representing the bridging force generated by the pins at pin region. In this case, both VCCT and CZM are used to computing the delamination propagation. The predicted load vs. displacement curves were validated by the experimental data in literature.

Finally, unpinned specimens under fatigue loading is predicted by a conventional fracture mechanics based fatigue life prediction approach. The results were then compared with experimental data found in literature.

6.1 Unreinforced specimens under static loading

In this section, the mode I and mode II fracture mechanical tests (DCB, ENF) were modelled to predict the crack growth and load vs. displacement relation using crack propagation analysis with the VCCT method and B-K fracture criterion in ABAQUS /Standard. Experimental data for model validation are from Asp [153].

6.1.1 Geometry and model description

The geometries and boundary conditions of DCB and ENF is shown in Fig. 6-1, Fig. 6-2, respectively:

The length of the DCB specimen L=150mm, with initial crack length a_0=35mm, half specimen thickness h=1.55mm and width W=20mm.

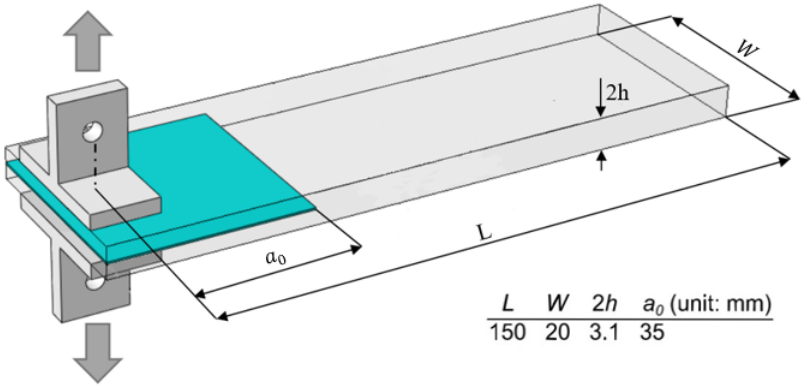

Fig. 6-1Boundary condition and geometry of DCB specimens

For the ENF specimen, specimen length L=100mm, with initial crack length a_0=35mm, half specimen thickness h=1.55mm and width W=20mm.

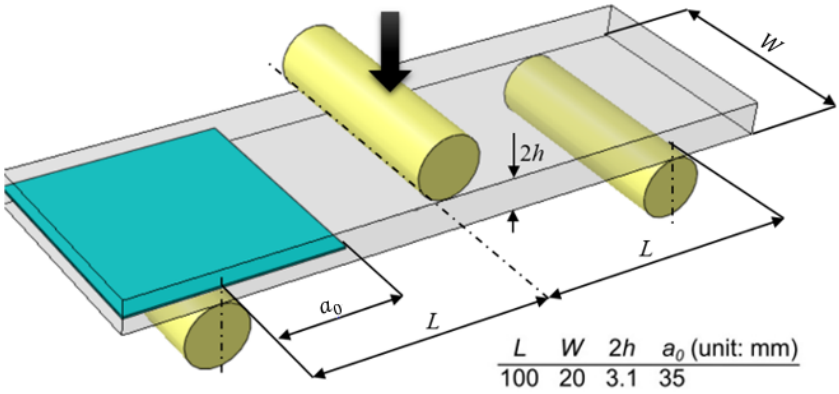

Fig. 6-2 Boundary condition and geometry of ENF specimens

Both DCB and ENF specimens consisted of two UD laminates made of toughened resin HTA/6376C carbon/epoxy prepreg, each laminate has 24 plies with the elastic material properties in Table 6-1.

Table 6-1 Material properties of HTA/6376C carbon/epoxy laminate [153]

E_{11}(GPa)	E_{22}=E_{33}(GPa)	G_{12}=G_{13}(GPa)	υ_{12}= υ_{13}	G_{IC}(J/m^2)	G_{IIC}(J/m^2)
146	10.5	5.25	0.3	238	883

In this ABAQUS simulation, the virtual crack closure technique (VCCT) is used to calculate the

applied strain energy release rate at the delamination crack tip. The "DEBOND" subroutine was used to activate crack propagation capability between two surfaces and release the crack tip nodes when the applied value exceeds the critical value, the toughness G_{IC}, or G_{IIC} in Table 6-1.

A mesh sensitivity study was carried out and the result shows convergence with a local mesh size of 0.5 mm in the longitudinal direction.

6.1.2 Simulation result

Load vs. displacement relationship

The load vs. displacement results for the DCB and ENF tests are shown in Fig. 6-3 and Fig. 6-4.

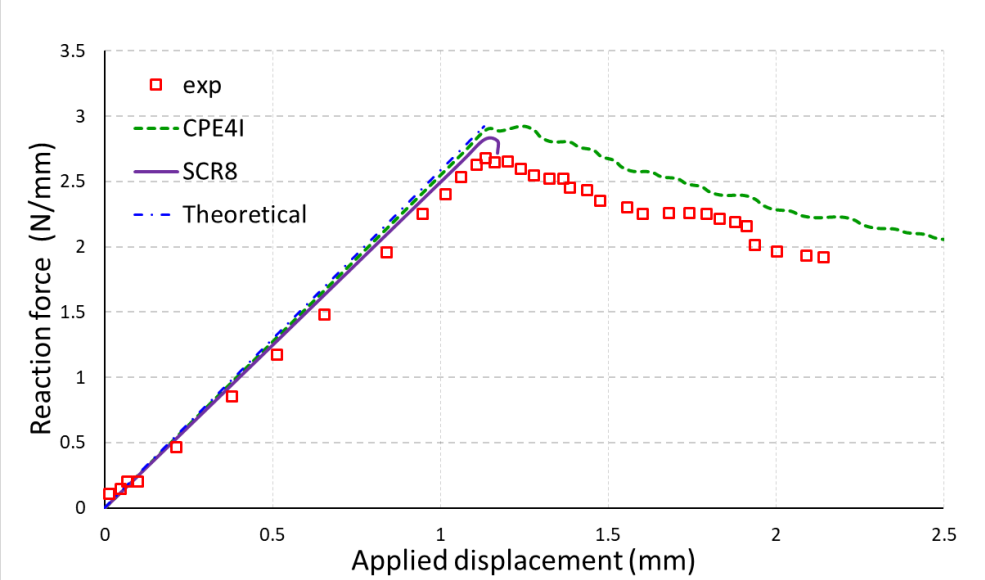

Fig. 6-3 Reaction force vs. applied displacement relationship in DCB test and modelling using different element types (Experiment data were taken from [153])

Generally, before the reaction force reaches its peak value, the agreement between FEA and experiment for DCB is very good, less good agreement for ENF (Fig. 6-4). In addition, theoretical solutions based on simple beam theory is also plotted and good agreement is achieved compared to the simulation results.

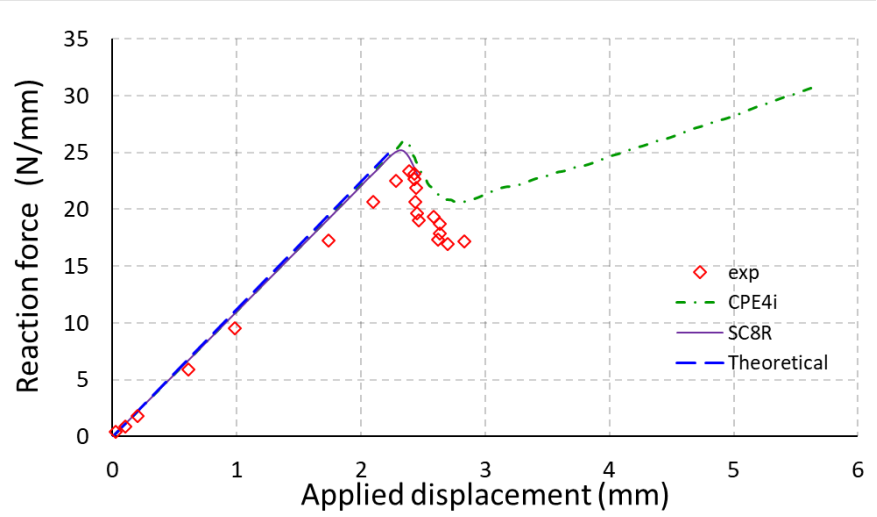

Fig. 6-4Reaction force vs. applied displacement relationship in ENF test and modelling using different element types (Experiment data were taken from [153])

According to the Fig. 6-4, the simulation and theoretical results gives higher stiffness compared to the experimental one. A possible reason is that the different elastic properties used in modelling and experiment. Despite the large difference in ENF, the general trend are similar to the experimental data.

Table 6-2 Maximum difference between FEA and experimental results

Element type	SCR8	CPE4I
DCB (before peak load)	3%	6%
DCB (after peak load)	9.9%	8.9%
ENF (before peak load)	14%	18%
ENF (after peak load)	15%	19%

The differences between the predicted load (during the initial linear portion of the test) and the experimental result are listed in Table 6-2.

After the peak load, delamination started to propagates; hence the modelling is sensitive to the G_{IC} or G_{IIC} value that were selected (Table 6-1). Thus, the large difference found after peak load is mostly due to the large scatter for both G_{IC} or G_{IIC} found in [153], (e.g. G_{IC}= 220±30 J/m^2 and G_{IIC} = 880±117 J/m^2).

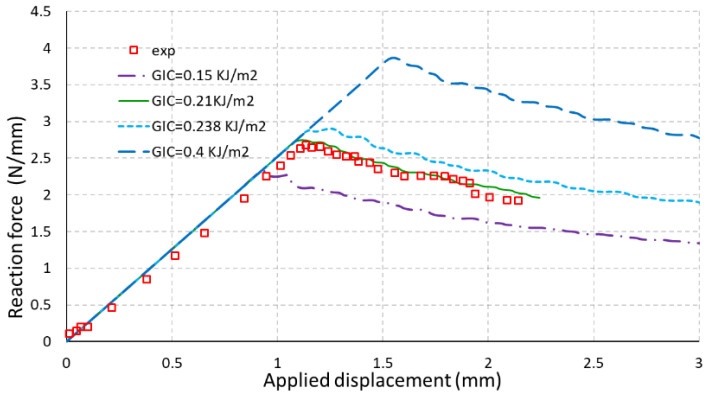

Fig. 6-5 Sensitivity study of G_{IC} value in DCB modelling (CPE4I element)

Fig. 6-5 is a sensitivity study of G_{IC} value used in the simulation, which shows that a reduced value of G_{IC} = 0.21 kJ/m^2 fit experimental result much better.

Crack extension vs. displacement relationship

In the ABAQUS simulation, the "DEBOND" subroutine was used to release the crack tip nodes. When G>G_{IC}. The crack extension-displacement results for the same DCB and ENF tests are shown in Fig. 6-6 and Fig. 6-7. The maximum differences between the predicted crack extensions and the experimental data for DCB and ENF are given in Table 6-3.

Table 6-3 Maximum difference between FEA and experimental results

	SCR8	CPE4I
DCB (average)	7.7%	8.3%
ENF (average)	5.6%	6.5%

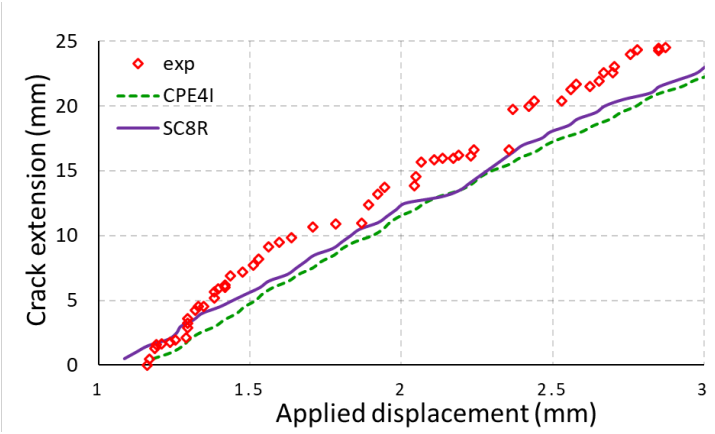

Fig. 6-6 Crack extension vs. applied displacement for DCB (Note: G_{IC} =250 J/m^2)

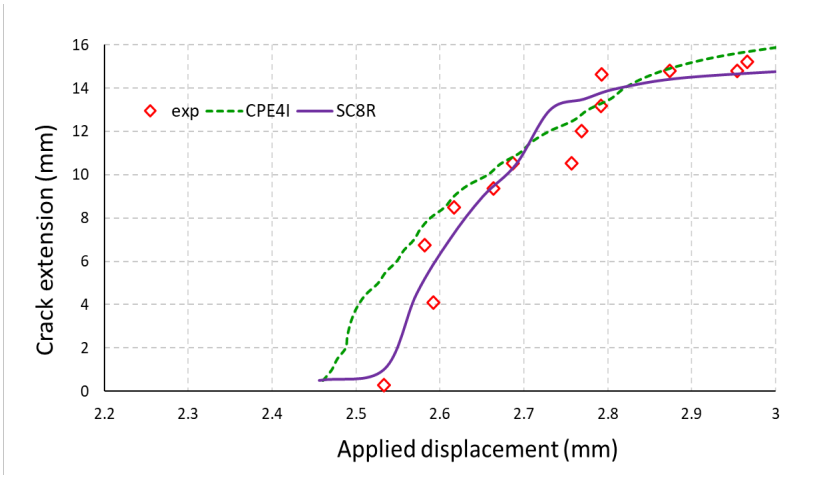

Fig. 6-7 Crack extension vs. applied displacement for ENF (Note: G_{IIC}=800 J/m^2)

General, both error of DCB and ENF are small, the results qualitatively show good agreement in trend. This also shows that continuum shell elements are capable of accurately capture nonlinear behavior during crack propagation.

Relationship of strain energy release rate vs. crack length

Strain energy release rate (G) vs. crack length (a) relation is the core data required to calculate the fatigue delamination growth life. In this FE simulation, a quasi-static load is applied to the specimens. By manually extending the crack length (nodal release method), the value of G was obtained for each crack length.

The strain energy release rate vs. crack length results for the DCB and ENF tests are shown in Fig. 6-8a and Fig. 6-8b. FE results are compared with a theoretical solution based on the Simple Beam Theory [155] as verification. Analytical expressions of are given in equation (6-1), (6-2):

$$G_I = \frac{12P^2a^2}{B^2E_sh^3} \tag{6-1}$$

$$G_{II} = \frac{9P^2a^2}{16B^2E_sh^3} \tag{6-2}$$

Where the applied load P is equal to 40 N and 300 N for the mode I and mode II test respectively, h is the single beam thickness, B is the width of specimen, and elastic modulus E_s= E_1=146 GPa for this composite material.

For the mode I simulation, continuum shell elements give the closest result (9.8%) compared with the theoretical solution, the difference increases to 13% for elements with incompatible modes.

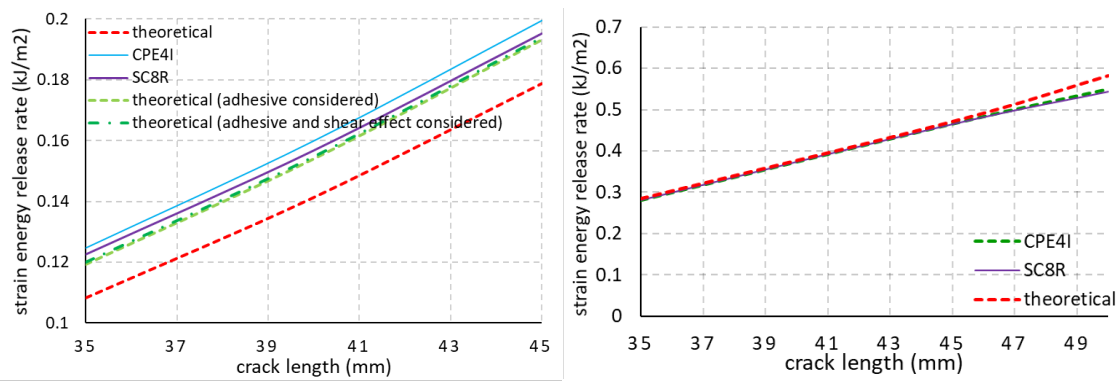

Fig. 6-8 G vs. a relationship for (a) DCB specimens and (b) ENF specimens

Such large difference is mainly due to above equation (SBT) neglect the involvement of the adhesive layer and the effect of shear deformation in the cracked portion of the specimen. By considering the stiffness effect of the adhesive layer, equation (6-3) is proposed in [156]:

$$G_I = \frac{12P^2a^2}{B^2E_sh^3}\left[1 + \frac{2}{Bh^{0.25}}\left(\frac{h}{a}\right) + \frac{1}{B^2h^{0.5}}\left(\frac{h}{a}\right)^2\right] \tag{6-3}$$

where $B = \sqrt[4]{3k/(E_1b)}$, $k = \frac{1}{\frac{1}{k_{adherend}} + \frac{1}{k_{adhesive}}}$ (k represent stiffness)

A more detailed equation which considers the shear effect also provided in [156]:

$$G_I = \frac{12P^2a^2}{B^2E_sh^3}\left\{1 + \frac{2}{Bh^{0.25}}\left(\frac{h}{a}\right) + \left[\frac{1}{B^2h^{0.5}} + \frac{E_1}{8G_{XZ}}\right]\left(\frac{h}{a}\right)^2\right\} \tag{6-4}$$

where G_{XZ} is the interlaminar shear modulus of the laminate.

The G vs. a relationship calculated by equations (6-3), (6-4) is then plotted in Fig. 6-8b. The difference is much smaller compared with original SBT method (Table 6-4).

For the mode II simulation, both SCR8 and CPE4I types of elements have a good agreement (less than 1%) compared with the theoretical solution.

Table 6-4 Difference between FEA and theoretical solutions for DCB and ENF specimens

	SCR8	CPE4I
DCB (SBT)	9.8%	13%
DCB (equation 6-3)	2.6%	5.8%
DCB (equation 6-4)	2%	5.2%
ENF (average)	<1%	<1%

In summary, both plane strain elements with incompatible modes, and continuum shell element have shown good agreement with experimental data.

6.2 Pin-reinforced specimens under static loading

6.2.1 Convergence study for nonlinear finite element analysis in ABAQUS

In delamination simulation, the changing of contact condition can result in extremely small time increments or convenience difficulties. This is even true for 3D models due to a large number of possible contact points. In order to achieve convergence, two default time incrementation parameters I_0 (default I_0=4) and I_R (default I_R=8) are modified to 8 and 10, respectively. Those two parameters have a direct effect on convergence since they can effectively avoid premature cutbacks of the time increment. The I_0 is the number of equilibrium iterations after which the check is made that the residuals are not increasing in two consecutive iterations. I_R is the number of equilibrium iterations after which the logarithmic rate of convergence check begins.

By altering the aforementioned parameters, crack propagation can be successfully simulated, with increment size range from 1.0e-05 to 1.0e-03. However, extremely small incremental size is occurred once the crack reach pin-reinforced area (range from 1.0e-12 to 1.0e-10). This is mostly due to the rapid soften behavior of cohesive element that representing z-pin's frictional pull-out behavior.

To alleviate the severe nonlinearity caused by pin's bridging behavior, the convergence tolerance parameter R_n^a is set to 0.008. The default value R_n^a = 0.5%, which is rather strict by engineering standards. Another modification is made for the cohesive traction-separation law in pin region as shown in Fig. 6-9. The modified traction-separation law have slightly mild soften behavior while the

area under the traction-separation curve (G_{IC}) keep unchanged. It is found that the slight change in soften behavior effectively reduce the solution cost (incremental size range from 1.0e-07 to 1.0e-05). In addition, line search algorithm is activated with default setting to accelerate the convergence of the iterative calculation.

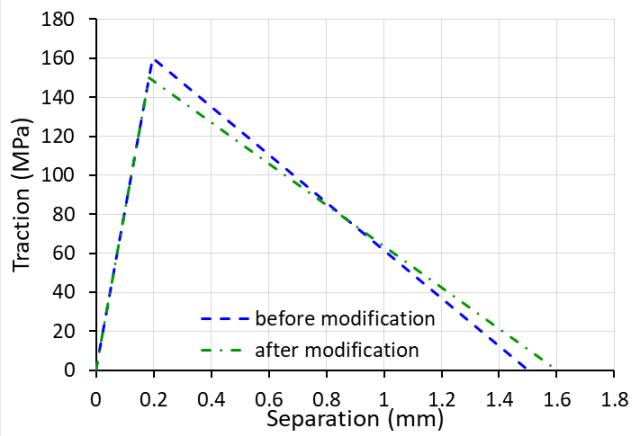

Fig. 6-9 The modified traction-separation law

Initially, the "BFGS" quasi-Newton method is selected since the full Newton method is computationally expensive. However, the current quasi-Newton method in ABAQUS is not supported by the parallel execution. To take the full advantage of High Performance Computing (HPC) Clusters, full Newton method is finally selected (8×8 cups and 1 gpu per task).

6.2.2 Pin-reinforced DCB (mode I)

A z-pined double cantilever beam (DCB) was modelled to calculate the load vs. displacement relationship. The result was then compared with the experimental result from [157] and numerical result from [145]. The DCB used in this analysis was made of 24 plies of the unidirectional prepreg of IMS/924 (Table 6-5)

Table 6-5 Material properties of DCB [145]

E_{11}(GPa)	E_{22}=E_{33}(GPa)	G_{12}=G_{13}(GPa)	υ_{12}= υ_{13}	G_{IC}(J/m^2)
138	11	4.4	0.34	250

The geometry of this DCB is the same as used in [145] (Fig. 6-10), with 180mm length and 20mm width. Each beam has the thickness of 1.55mm and the size of the initial disband crack is 50mm.

Fig. 6-10 double cantilever beam specimen geometry and dimension (unit: mm) [145]

Pin-reinforced area starts 5 mm from the initial crack tip lasting 25 mm in length and covering the entire specimen width. The diameter of the pin is 0.51mm, and the pin density in the pin area A_p = 2% with a pin pitch of 3.4mm (8 pins along length direction and 6 pins along width direction). One end of the beam is fixed, and a displacement controlled load of 16mm is applied at the other end.

For each adherend, continuum shell elements (SC8R) are used. The element size of free arm and bonded area varies from 0.8mm×0.8mm to 0.3mm×0.3mm. For the area close to pin, small mesh of 0.1mm×0.1mm is applied (Fig. 6-11).

In the interface between two beams, cohesive surface method is used to simulate crack propagation for both bonded area and pin-reinforced area. The laminate interaction property of the cohesive surface is the same used in [145] (Fig. 6-11).

In the pin-reinforced area, the bridging force generated by z-pin in the macro-scale structural model are represented by a bilinear traction-separation cohesive law (Fig. 6-12).

The cohesive parameters of this law are deduced from the pin pull-out force vs. displacement data obtained from [157]. It is expressed as

$$T(\delta) = \frac{P(\delta)}{A_{pin}} \tag{6-5}$$

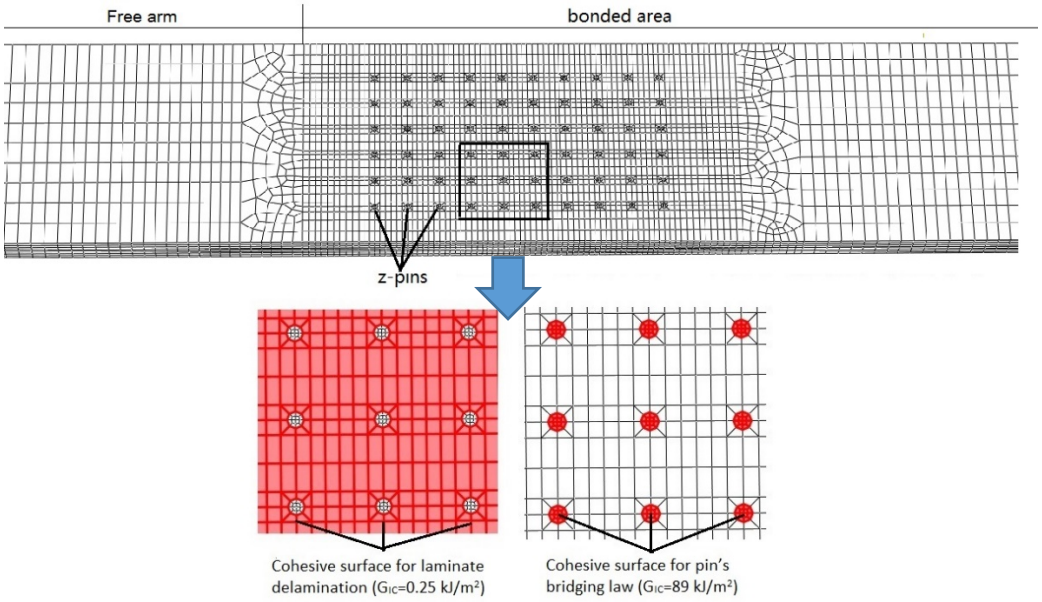

Fig. 6-11 FE model for the DCB (cohesive surface are used to represent laminate delamination and pin's bridging law)

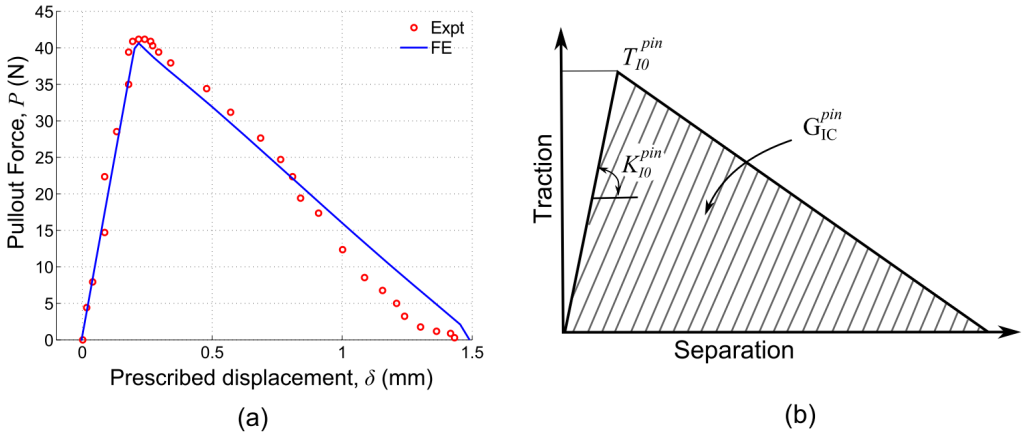

Fig. 6-12 (a) Pin pull-out force vs. displacement data from [157], (b) Typical bilinear traction-separation cohesive law

Where δ is the delamination opening displacement, A_{pin} is the total area of cohesive element cross section for one pin, $T(\delta)$ is the bridging stress in the cohesive law and $P(\delta)$ is the pin bridging force (derived from the experiment result or FE model).

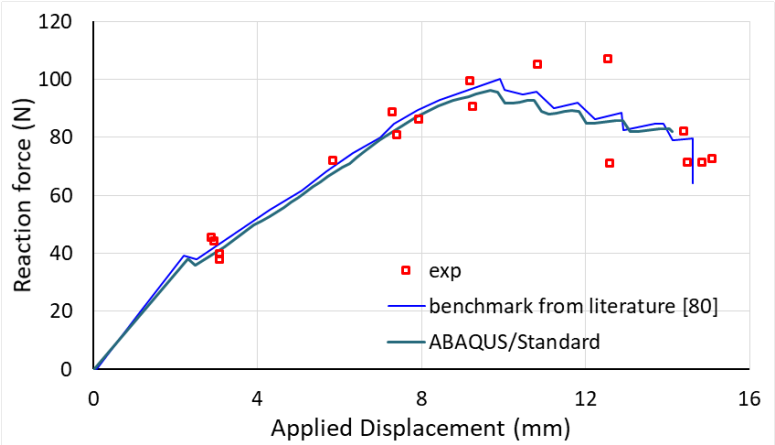

Fig. 6-13 FE and experimental results of reaction force vs. displacement curve of z-pinned DCB (Experiment data and benchmark results were taken from [145])

Table 6-6 cohesive parameter used in FE model

	Laminate bonding	Pin bridging
initial stiffnes K_0	1×10^{14} N/m^3	8.1×10^{11} N/m^3
cohesive strength $\mathbf{T}_0$	30 MPa	160 MPa
fracture toughness G_{IC}	0.25 kJ/m^2	89 kJ/m^2

As shown in Fig. 6-13, the simulation result shows good agreement compared with [145].

6.2.3 pin-reinforced ENF (mode II)

An ENF (end notch flexure) is modelled to calculate the load vs. displacement relationship. The material and geometry are the same as used in [145] (Table 6-7 and Fig. 6-14)

Table 6-7 Material properties of laminate used in the ENF specimen

$\boldsymbol{E_{11}}$(GPa)	$\boldsymbol{E_{22}}$=$\boldsymbol{E_{33}}$(GPa)	$\boldsymbol{G_{12}}$=$\boldsymbol{G_{13}}$(GPa)	$\boldsymbol{\upsilon_{12}}$= $\boldsymbol{\upsilon_{13}}$	$\boldsymbol{G_{IIC}}$(J/m2)
138	11	4.4	0.34	770

Fig. 6-14 The pinned ENF geometry [145] and boundary condition

One end of the beam is fixed and the other end is constrained in Z direction. A displacement controlled load of 6mm is applied at the mid of specimen. According to [157], z-pins have three type of possible failure mode occurs in the experiment, which is pullout, axial shear failure and transverse shear failure (Fig. 6-15). Which failure mode will occur is mainly depending on the diameter of the pin and the thickness of the laminate. If the pin diameter is small, the transverse rupture will occur (with low energy absorption). In this ENF modelling case, the pin is assumed to failure in the pull-out manner (the diameter of the pin is 0.51mm) according to the experiment results.

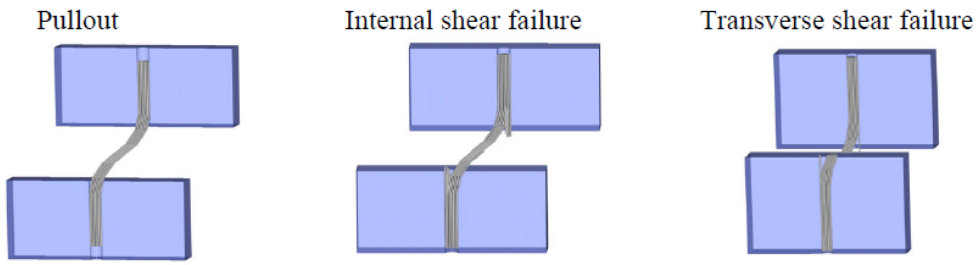

Fig. 6-15 Three possible failure modes of z-pins under mode II loading

The pin density in the pin area is Ap = 2% with a pin pitch of 3.1mm (8 pins along length direction).

Both VCCT and cohesive element method can be used to simulated the crack propagation. In this section, VCCT method is used to simulate the crack propagation and calculate the strain energy release rate G at crack tip, the cohesive elements is used to simulate pinned area as shown in Fig.6-16.

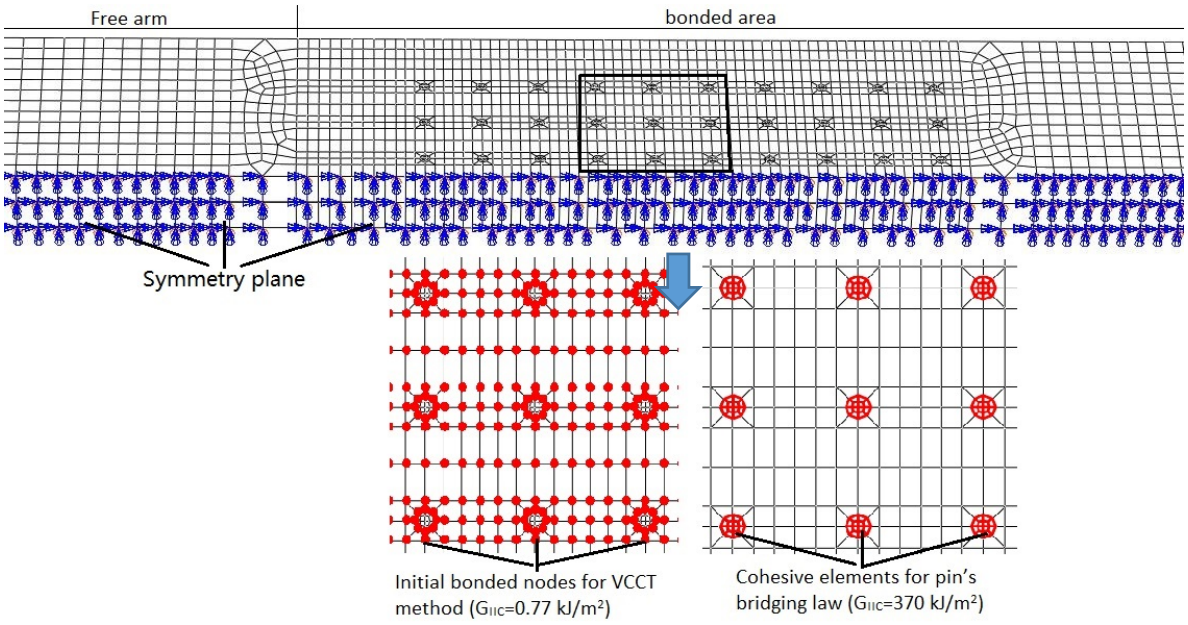

Fig. 6-16 FE model for pinned ENF (VCCT for laminate delamination and CZM for pin's bridging law)

The result was plotted in Fig. 6-17. Compared with the cohesive result, the vibration is very large, but if we ignore those noises, the VCCT result matches the experimental result well. In addition, that large vibration in VCCT could be the reason why one element in the thickness is not enough to resist hourglass effect while one element is sufficient for cohesive element method.

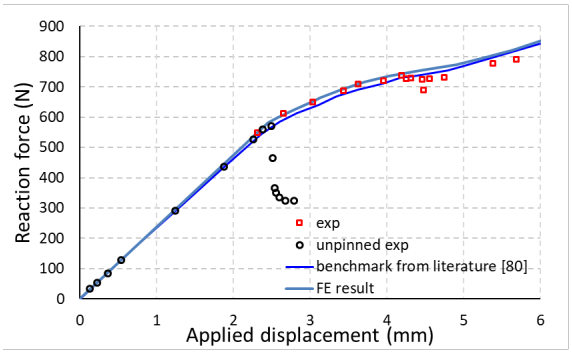

Fig. 6-17 load-displacement for pinned ENF model

6.3 Unreinforced specimens under fatigue loading

In this section, the fatigue life of unpinned DBC and ENF are predicted using a fracture mechanics based fatigue crack growth approach to life prediction, which uses the finite element method in conjunction with the fatigue crack growth rate laws. To validate this methodology, the fatigue life of

double cantilever beam (DCB) and end notch flexure (ENF) tests was predicted and the results were then compared with experimental data found in literature.

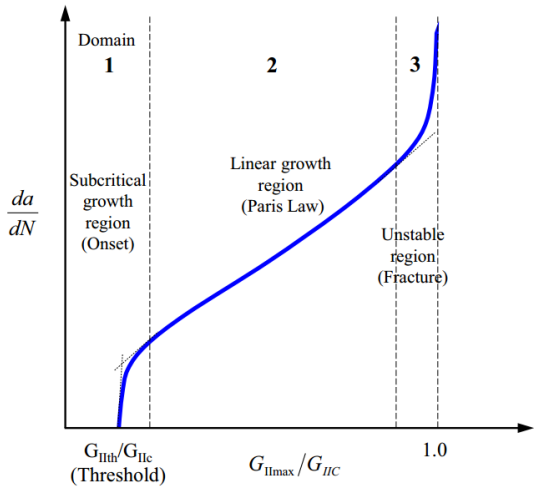

Fig. 6-18 Conceptual plot of fatigue crack growth rate laws

In this approach, the stable crack propagation phase (region 2 in Fig. 6-18) is assumed to be dominant, and the crack growth rate is governed by the strain energy release rate (G). An empirical crack growth law is applied to characterize crack growth life (e.g. Paris law), and by integrating the fatigue crack propagation rate, an estimation of crack propagation life of the joint can be obtained.

The detailed procedure is illustrated in Fig. 6-19 and described in section 2.2.3

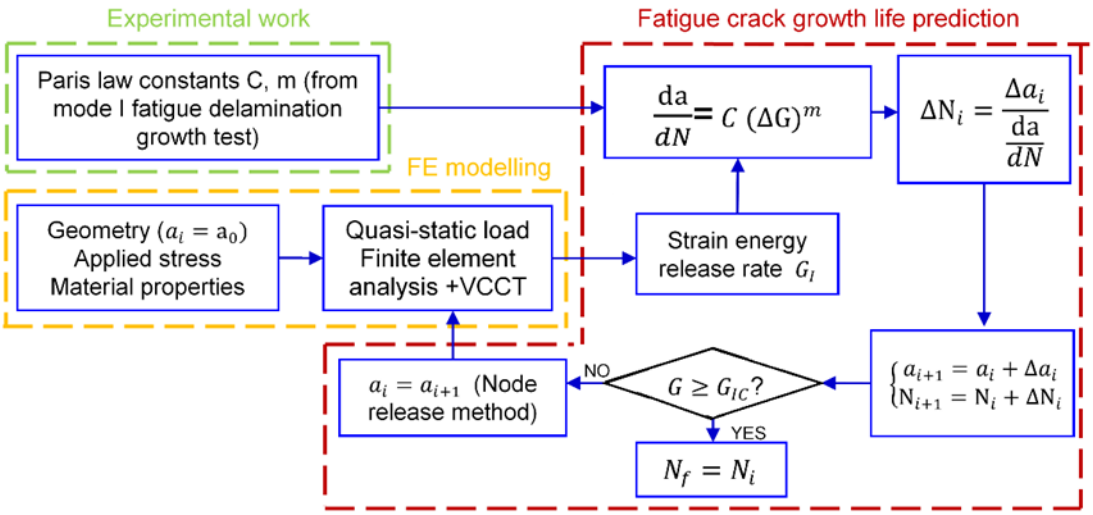

Fig. 6-19 Flow chart of procedures for fatigue crack growth life prediction; Three steps =(a)

experimental work, (b) FE modelling, (c) Fatigue crack growth life prediction

6.3.1 Unreinforced DCB (mode I)

The fatigue life of DCB was predicted based on the methodology and calculation procedure described in Fig. 6-19. 6-10 and the results were then compared with experimental data published in [159].

The DCB specimen was subjected to displacement control (maximum applied displacement 2.4 mm with R ratio = 0.1). The DCB specimen used in this paper has a total length of 145 mm, with initial crack length a_0=32.6 mm, half specimen thickness h=2 mm and width B=20 mm.

The specimen consisted of two [0_{12}] laminates made of HTA/6376C carbon/epoxy prepreg, with the elastic material properties given in Table 6-8 [159].

Table 6-8 Material properties of HTA/6376C carbon/epoxy prepreg from [159]

$\mathbf{E_{11}}$(GPa)	$\mathbf{E_{22}}$=$\mathbf{E_{33}}$(GPa)	$\mathbf{G_{12}}$=$\mathbf{G_{13}}$(GPa)	$\boldsymbol{\upsilon_{12}}$= $\boldsymbol{\upsilon_{13}}$
109.8	7.4	4.4	0.3

Based on the study in Chapter 4, elements with incompatible modes are efficient for bending analysis when used at sufficient refinement, and the strain energy release rate calculated by element with incompatible mode is consistent with higher order elements. Thus, in this Chapter, the CPS4I elements (2D plane stress element with incompatible mode) were used to calculate the G value. A mesh sensitivity study shows convergence with a mesh size of 0.5mm in the longitudinal direction (Fig. 6-21a).

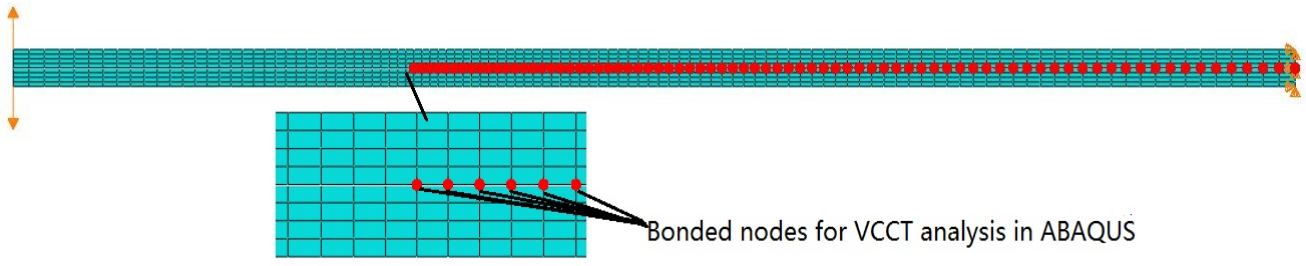

Fig. 6-20 DCB model in ABAQUS (VCCT method for laminates delamination)

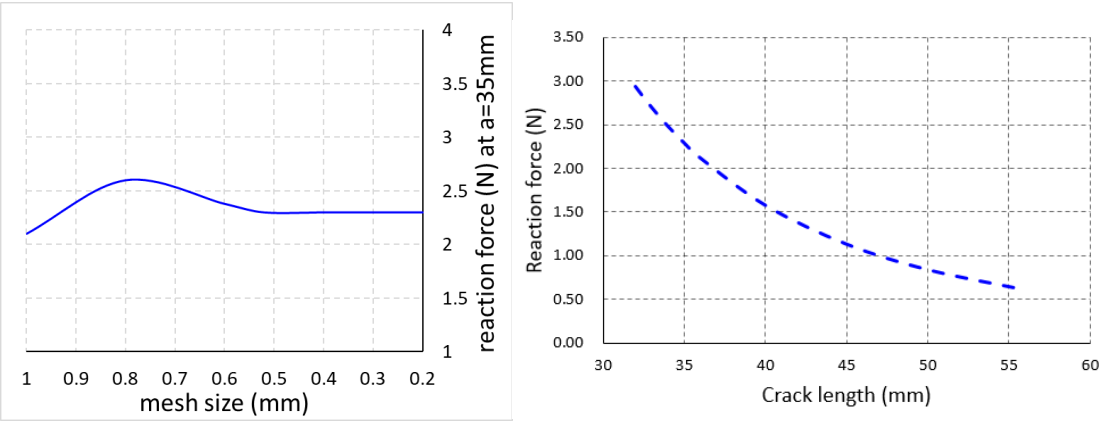

Fig. 6-21 (a) mesh sensitivity study, (b) reaction force vs. crack length curve under constant applied displacement of 2.4 mm

For this simulation, ABAQUS/Standard analysis is selected due to absence of static instabilities allowing successful convergence with a Standard analysis. The node release method is used to manually extend the crack length while the maximum tab displacement is held constant at 2.4 mm. The reaction force obtained at each crack length was then plotted and the results shown in Fig. 6-21b.

In the fatigue test, the specimen was subjected to displacement controlled cyclic loading with a load ratio R=0.1. When the crack propagates, the global resistance to the crack propagation is gradually weakened. Thus, the reaction force is decreased with increasing crack length.

To predict the fatigue crack growth life, the strain energy release rate (G) was obtained as a function of crack length using a VCCT analysis in ABAQUS. To verify the result (G vs. a curve), a simple equation derived from Euler beam theory is used to calculate the strain energy release rate [133]:

$$G_I = \frac{3P_{FE}\delta}{2ba} \tag{6-6}$$

where δ=2.4 mm, P_{FE} is reaction force at the loading ends calculated by FEA.

According to the Euler Beam Theory calculation, the strain energy release rate (G) decreases with crack extension (Fig. 6-22). Since good agreement is achieved, the G vs. a curve is ready to be used in the fatigue crack growth law.

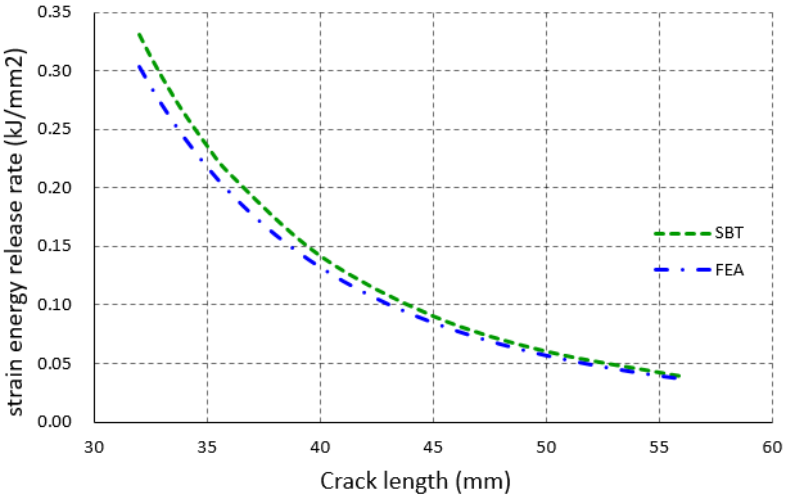

Fig. 6-22 Strain energy release rate vs. crack length curve under constant applied displacement of 2.4 mm

For the mode I fatigue crack growth data, Paris law parameters of C_1=0.7566 and m_1=4.7008 and C_2=6.3957 and m_2=6.2121 were selected to fit the experimental data from [159] and [160] (independent from the geometry used in this report) respectively. The experimental data and fitted curves are shown in Fig. 6-23.

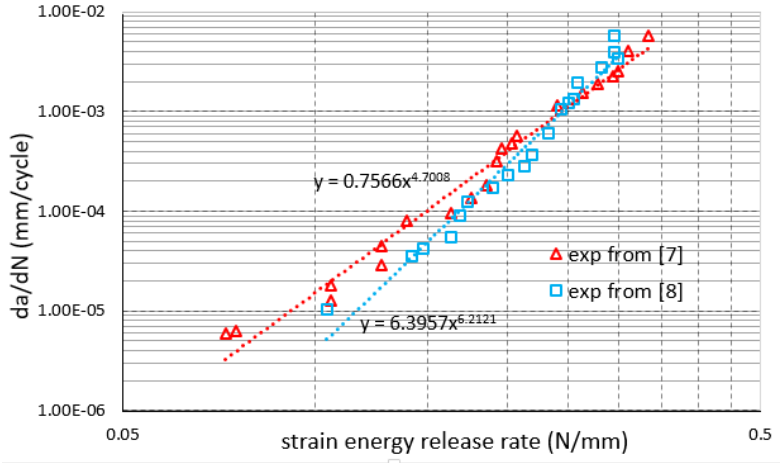

Fig. 6-23 Fatigue crack growth data [159, 160]

When the G vs. a curve and fatigue crack growth data are determined, the fatigue life is then calculated by equations:

$$\frac{\mathrm{da}}{dN} = C(\Delta G_i)^m \tag{6-7}$$

$$\Delta N_i = \frac{\Delta a_i}{\frac{da}{dN}} \tag{6-8}$$

$$N_i = N_{i-1} + \Delta N_i \tag{6-9}$$

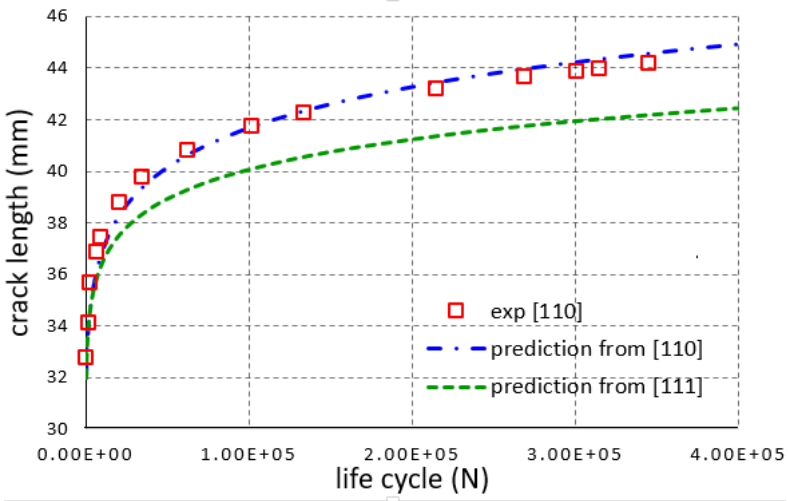

Fig. 6-24 Crack length vs. fatigue life curve in DCB test [159] and prediction results

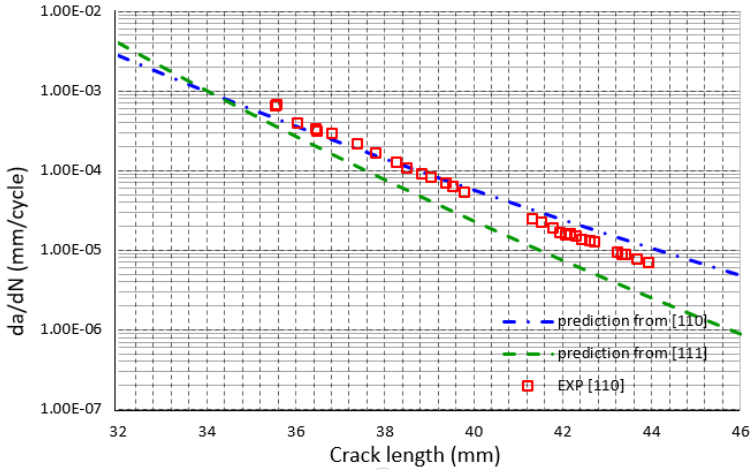

Fig. 6-25 Crack growth rate vs. crack length curve in DCB test [160] and prediction results

Fig. 6-24 shows good agreement between prediction (use crack growth data from [159]) and experiment. However, large difference was found between prediction (use crack growth data from [160]) and experiment due to the different *C* and *m* value used in [159] and [160].

Fig. 6-25 shows the fatigue crack growth rate vs. crack length relationship. The experimental crack growth rate data are obtained by the 7-point polynomial method, and *a* vs. *N* data from data set-1 [159] shows good agreement while prediction from data set-2 [160] show a distinct difference.

6.3.2 Unreinforced ENF (mode II)

The fatigue life of ENF was predicted based on FEA and fracture mechanics, and the results were then compared with experimental data published in [161]. The ENF specimen used in this paper has a total length of 120 mm, with initial crack length a_0=17 mm, half specimen thickness h=2.8 mm and width B=20 mm.

The specimen was made of T300/ REM with the elastic material properties in Table 6-9.

Table 6-9 Material properties of T300/ REM carbon/epoxy prepreg

$\mathbf{E_{11}}$(GPa)	$\mathbf{E_{22}}$=$\mathbf{E_{33}}$(GPa)	$\mathbf{G_{12}}$=$\mathbf{G_{13}}$(GPa)	$\mathbf{G_{23}}$(GPa)	$\boldsymbol{\upsilon_{12}}$= $\boldsymbol{\upsilon_{13}}$	$\boldsymbol{\upsilon_{23}}$
130	11	4.96	3.48	0.3	0.49

In this simulation, CPS4I elements were used to calculate the G value. A mesh sensitivity study shows convergence with a mesh size of 0.5mm in the longitudinal direction.

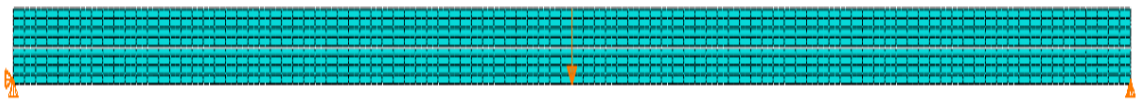

Fig. 6-26 The ENF model in ABAQUS

The simulated fatigue test of the ENF specimen was subjected to load control (maximum applied 1055N) and node release method is used to manually extend crack length while the maximum load remains 1055N. The strain energy release rate (G) obtained at each crack length was then plot against theoretical solution [134] in Fig. 6-27.

$$G_{II} = \frac{9P^2a^2}{16b^2h^3E_1} \tag{6-10}$$

According to Fig. 6-27, good agreement is achieved between FE method and theoretical solution (less than 5%) and therefore the G vs. a curve is ready to be used in the fatigue crack growth law.

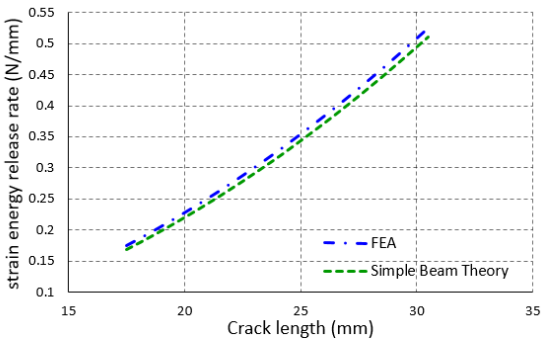

Fig. 6-27 *G* vs. *a* curve under constant applied load of 1055N

For the fatigue crack growth data tested in [161], there are 4 groups of data (two groups under 1055N load and two groups under 650N load) recorded and the data seem to exhibit a significant scatter as compared to the typical metallic material. Paris law parameters of C=0.022 and m=2.9435 was selected from the best fitting curve for the experimental data.

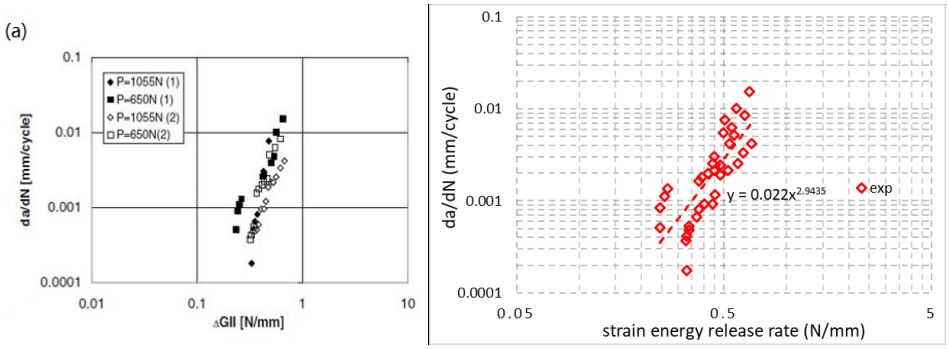

Fig. 6-28 Fatigue crack growth data from [161] (a) and digital scan (b) with a R ratio of 0.1

When the *G* vs. *a* curve and fatigue crack growth data are determined, the fatigue life is then calculated by equations (6-7) - (6-9).

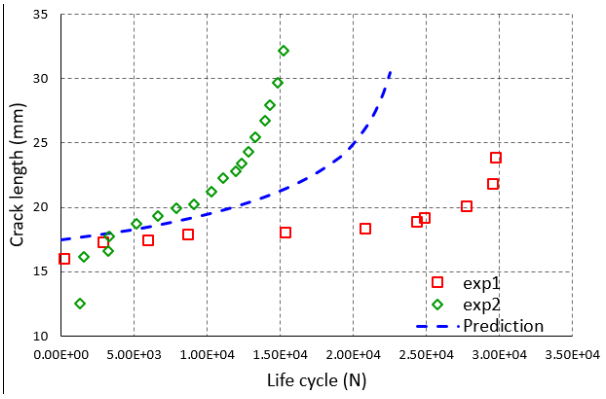

Fig. 6-29 Crack length vs. fatigue life curve in ENF test [161] and prediction results

Fig. 6-29 shows crack length vs. fatigue life relationship while Fig. 6-30 shows the fatigue crack growth rate vs. crack length relationship.

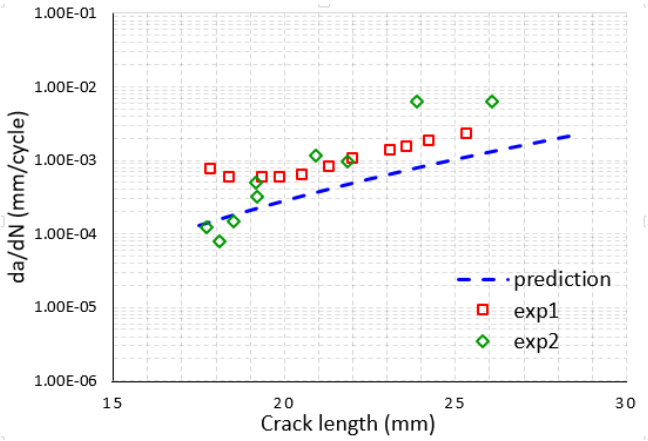

Fig. 6-30 Crack growth rate vs. crack length curve in ENF test [161] and prediction results

The difference between experimental results and prediction in Fig. 6-30 is considerably smaller as compared to *a* vs. *N* curve in Fig. 6-29. In *a* vs. *N* curve, the fatigue life is accumulated based on every crack increment. Thus, the difference is also accumulated.

The reason for this difference could be the large scatter found in fatigue crack growth data. However, both prediction curves are in the middle of two experimental results which seem to be a reasonable prediction.

6.4 Summary

FE model of unpinned DCB (pure mode I loading) and ENF (pure mode II loading) under static loads has been developed using various element types. The Load vs. displacement relationship, crack extension vs. displacement are validated by experimental data whereas strain energy release rate vs. crack length relationship was verified by theoretical solution.

In addition to unpinned specimen, FE model of pin-reinforce DCB and ENF have been developed by continuum shell element. The model have been validated under static loads by comparing model results with experiments. Key simulation skills (VCCT, CZM) were also validated.

The fatigue delamination growth life of unpinned DCB and ENF have been predicted based on FEA

and fracture mechanics. The work in this chapter is aimed to validate the traditional fracture mechanics based fatigue life prediction approach (for unpinned specimen), which is further expanded to pinned structures detailed in Chapter 6 and 7.

Predicted results of both crack length vs. fatigue life and fatigue crack growth rate vs. crack length relationship have been plotted against the experimental data published in [159-161] as validation. Good agreement has been achieved for the DCB case while the prediction of ENF show a distinct difference due to large scatter of fatigue crack growth data published in [161].

7. Prediction of z-pinned composites under mode I fatigue loading

7.1 Introduction

A hybrid method combining liner elastic fracture mechanics and nonlinear damage mechanics is developed in this paper to predict the fatigue crack growth life of a z-pinned DCB and a z-pin reinforce stiffener-to-skin joint under the mode I loading. This procedure is illustrated in Fig. 4-11 and detailed explained in Section 4.5.

The modelling details are described in Section 4.1. The strain energy release rate is evaluated by virtual crack closure technique in finite element analyses, and cohesive elements are applied to the pin region representing the bridging force generated by individual pins.

The constitutive model for individual Z-pin under static loading is stated in Section 4.2. Empirical constitutive model which is based on the test results of pins pull-out test is developed and is implemented to FE analysis to simulate a z-pinned DCB in Section 7.2. Numerical model is also developed for the prediction of a z-pin reinforce stiffener-to-skin joint in Section 7.3.

A degradation law is proposed in Section 4.3 to describe debonding and frictional degradation of single pin's bridging force under the mode I fatigue loading, which is based on the damage mechanics approach with empirical fitting parameters. The proposed degradation law has been further modified so that it is capable of accumulating damage under variable amplitude of displacement during fatigue loading. The constitutive model for individual Z-pins subjected to fatigue mode I loadings is fully defined in Section 4.4 and is illustrated in Fig. 4-10.

7.2 z-pinned laminate (DCB geometry)

7.2.1 Specimen geometry, material properties, test condition and model description

Pinned DCB specimens were fabricated for both static and fatigue testing using AS7/8552 carbon-epoxy prepreg with a UD layup of $[0]_{24}$. The material properties are given in Table 7-1, and the specimen geometry is shown in Fig. 7-1. During specimen manufacture, a thermal insulated film with a length of 50 mm was inserted at the mid-plane to create an initial delamination crack between

the adherends.

The z-pins were made of carbon fiber-bismaleimide (BMI). The pin-reinforced area is 12 mm away from the initial crack tip and extending for 25 mm length covers the entire specimen width. The diameter of each pin is 0.51mm, with a pin pitch distance of 3.2 mm resulting in the pin areal density is 2%.

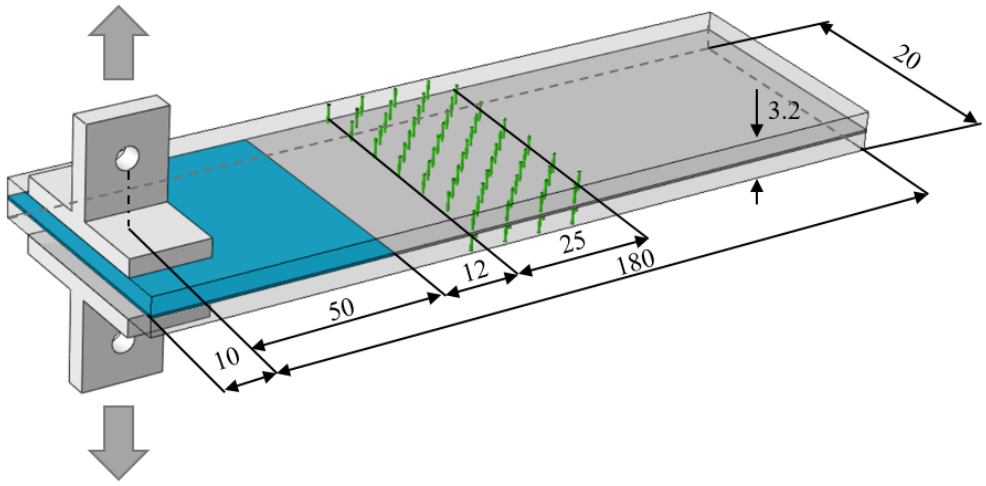

Fig. 7-1Geometry and dimension of z-pinned DCB specimen

Table 7-1 Material properties and Paris law constants of AS7/8552 [162]

E_{11}(GPa)	E_{22}=E_{33}(GPa)	G_{12}=G_{13}(GPa)	υ_{12}= υ_{13}	G_{IC}(J/m^2)	C	m
145	10	5	0.34	280	2.0E+06	13.14

Table 7-2 Summary of tests

Specimen	Load	Test condition	No. of tests	Loading rate / Frequency	Specimen No.	Half thickness (mm)
Pin pull-out	Static	Displacement control	3	0.5 mm/min	SP1, SP2, SP3	1.68-1.85
Pinned DCB	Static	Displacement control	3	1 mm/min	S1, S2, S3	1.62-1.78
Pinned DCB	Fatigue	Maximum disp. = 22.7mm (80% d_{Pmax})	3	3 Hz	F1-1, F1-2, F1-3	1.70±0.02
Pinned DCB	Fatigue	Maximum disp. = 25.7mm (90% d_{Pmax})	3	3 Hz	F2-1, F2-2, F2-3	1.70±0.02

Table 7-2 summarizes the tests performed in this work. Static tests of pinned DCB specimens and tensile pin pull-out tests were conducted on a 50 kN electro-servo mechanical machine (Instron 3369)

under a displacement-controlled loading rate of 1 mm/min and 0.5 mm/min respectively.

The fatigue tests of pinned DCB were conducted under displacement-controlled load (3Hz) with a load ratio of 0.1. Two groups of fatigue tests were carried out in which the applied cyclic displacement amplitude was either 80% or 90% of the displacement at peak load under static test (d_{Pmax}). For each test condition, three samples were tested. To minimize the thickness effect on crack length as reported in Section 4.2, specimens with thickness of 1.70±0.02mm were selected for fatigue testing.

A separate compliance test was carried out to exclude the compliance of test machine. Furthermore, two tabs were adhesively bonded together and were tested to exclude the deformation of the tab-to-specimen adhesive during the pin pull-out tests.

Model description

The FE software package ABAQUS v6.14 was used for the analysis. A z-pinned double cantilever beam (DCB) was modelled (Fig. 7-2) quasi-statically to calculate the strain energy release rate vs. crack length curve. The Virtual Crack Closure Technique (VCCT) is used to calculate the response of the adhesive bonding, and the Cohesive Zone Method (CZM) is used to model the reponse of the pinned locations.

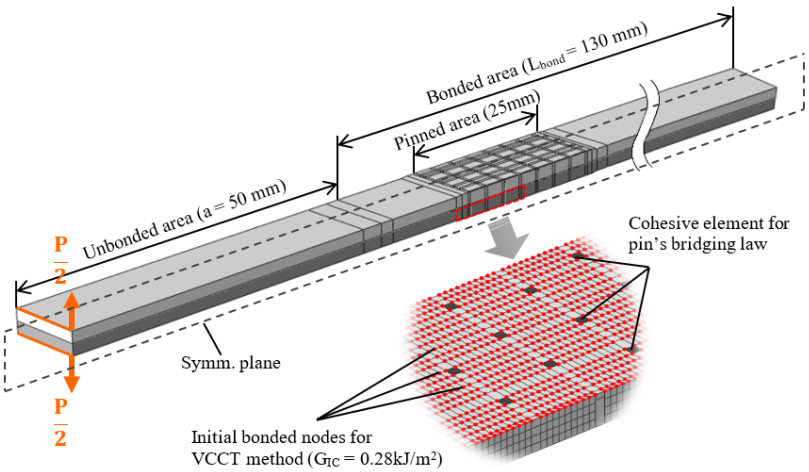

Fig. 7-2 FE model for half of the DCB specimen

8-node linear continuum shell elements with reduced integration (designated as CS8R in ABAQUS)

were used for the laminate and 8-node cohesive element (COH8) for the pin locations. The element size of unbonded and bonded area varies from 0.8 mm×0.8 mm to 0.3mm×0.3mm, respectively. For the area close to the pins, smaller mesh of 0.2 mm×0.2 mm is applied. Owing to the symmetric geometry, only half of the DCB is modelled.

The bonded area is governed by the intrinsic toughness (G_{IC}) of the laminate material (matrix), whereas the pinned locations are governed by the pin's load vs. displacement response which was based on test results of three tests of pins pullout.

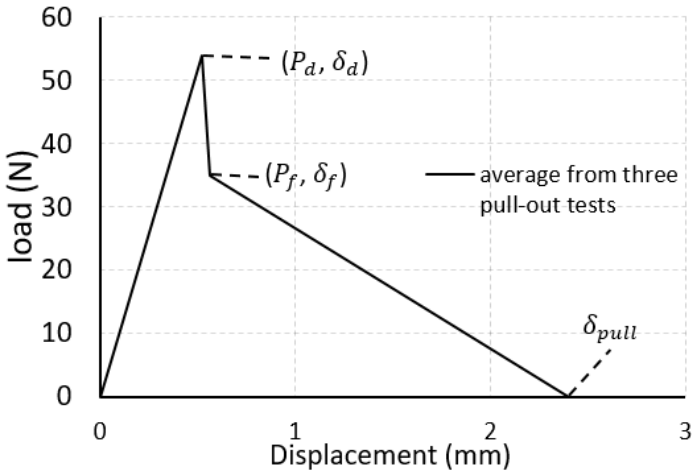

Fig. 7-3 Schematics of (a) Average single pin load vs. displacement relation from pull out test (b) tri-linear traction-speration law used in cohesive element in pin region

A tri-linear relationship (Fig. 7-3) between the bridging force and z-pin displacement is selected:

$$P = \begin{cases} \frac{\delta}{\delta_d} P_d & (0 \le \delta \le \delta_d) \\ \frac{\delta_f - \delta}{\delta_f - \delta_d} P_d + \frac{\delta - \delta_d}{\delta_f - \delta_d} P_f & (\delta_d \le \delta \le \delta_f) \\ P_f + \frac{\delta_f - \delta}{\delta_{pull} - \delta_f} P_f & (\delta_f \le \delta \le \delta_{pull}) \end{cases} \quad (7\text{-}1)$$

Where P the current bridging force, P_d the maximum debonding force, P_f the maximum friction force, and their corresponding displacements (δ, δ_d, δ_f), and δ_{pull} the pull-out displacement of pin.

The first stage is the elastic stretching of the pins and follow by debonding of the pins, and lastly frictional pull-out of the debonded pins. The cohesive law parameters were then deduced from the

average load vs. displacement data.

$$T_d = \frac{P_d}{A_{pin}} \quad \text{or} \quad T_f = \frac{P_f}{A_{pin}} \tag{7-2}$$

where A_{pin} is the cross section area for one pin, and the T is the bridging strength in the cohesive law and P_{d}, P_{f} are the peak debond and frictional loads, respectively.

Crack length is a key parameter in fatigue analysis. As reported in Section 4.2, crack propegation under static loading could be affected by the pin condition. This effect could be more significant under fatigue loading. Thus, to account for this variation, the prediction methodology assumed each pin row has a separate bridging law parameters, and damaged pin are considered as half pin. Thus, the peak bridging force in each row can be calculate as:

$$P_d = \frac{n_{eff}}{n_{nom}} P_{d0} \text{ or } P_f = \frac{n_{eff}}{n_{nom}} P_{f0} \tag{7-3}$$

Where n_{nom} is the nominal number of pins in a pin row , n_{eff} is the number of effective pins in a pin row.

Two extreme scenarios are used to predict the upper and lower bounds of fatigue life of pinned specimens, instead of one single model. The first case assuming every pin are perfectly inserted, with n_{eff} =7. The second case are using worst pin condition of each pin row observed from specimens after static tests (S1-S3), with average n_{eff} =5.2.

To reduce the simulation time, a square cross section element was used to represent pin's bridging effect, instead of octagonal cross section cohesive elements. As long as the total area of cohesive elements for a single pin remains the same, the bridging force per pin is equivalent. Since the pins are very small, the geometric effect of the cross-section of the pins can be neglected.

7.2.2 Results and discussion

Pin pull-out tests under static load

The compliance of test machine and deformation of the tab-to-specimen adhesive are excluded by

separate compliance tests. The load-displacement curves of three tests of pins pull-out are shown in Fig. 7-4. The results from SP1 and SP3 shows a simular trend which can be represented by a tri-linear bridging law, whereas the SP2 gives higher frictional traction load after pins' debonding. The observation after tests revealed that pins in SP2 have relatively large misalignment, which effectively increased the average embedded lengths and induce a transition from mode I opening to mode II sliding, and hence increase the traction load.

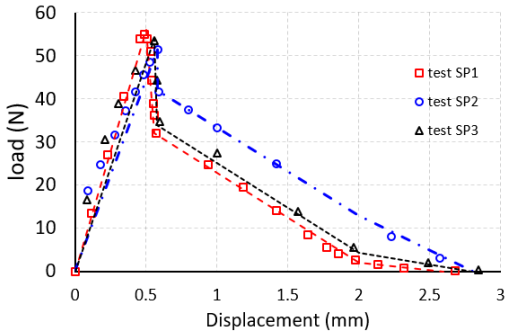

	Stiffness (N/mm)
SP1	111.3
SP2	96.1
SP3	87.8

Fig. 7-4 load-displacement curve of pin pull-out test

Static tests and simulation results of pinned DCB specimens

The load-displacement curves under static tests are shown in Fig. 7-5a. Large difference was found between three tests results, specially after the elastic phases. This is due to the difference in thickness (half thickness of 1.62mm, 1.70mm and 1.78 mm, as measured by digtal caliper). FE models with different thicknesses were build with the same cohesive law of pins. All of FE models shows good agreement compared with experiment data.

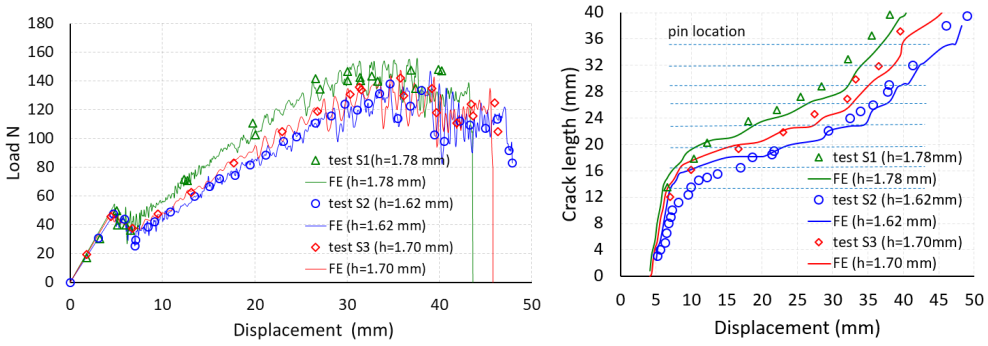

Fig. 7-5 Experiment and modelling results of DCB under static load: (a) load-displacement curves under static loading, (b) crack length vs. displacement curve

The crack length vs. displacement curve of three tests are shown in Fig. 7-5b. The largest difference of crack length between S1 and S2 under same applied displacement is about 10 mm, which indicated that the difference in specimen thickness significantly affects the crack propegation of z-pinned DCB. The predicted curves are also plotted in Fig. 7-5b. For all three cases, FE model underestimated the crack growth at later stage (up to 5mm), which could have been caused by the difference of pins' condition, since the insertion condition of pins pull-out test specimen are different from the massive fabrication.

Fatigue tests and prediction results of z-pinned DCB

To validate the proposed prediction methodology, two test groups (group 1, 2) were tested which was subjected to two different cyclic applied displacement (80% d_{Pmax} and 90% d_{Pmax} , respectively). The first group is tested under relatively small cyclic applied displacement, thus, most of pins are expected to experience debonding degradation as discussed in Section 2.4. For the second group, large applied displacement is likely to cause pin fully debond and therefore experience frictional degradation.

For the test group 1 (F1-1, F1-2 and F1-3), predicted upper and lower bounds of crack length vs. fatigue life curve is shown in Fig. 7-6a.

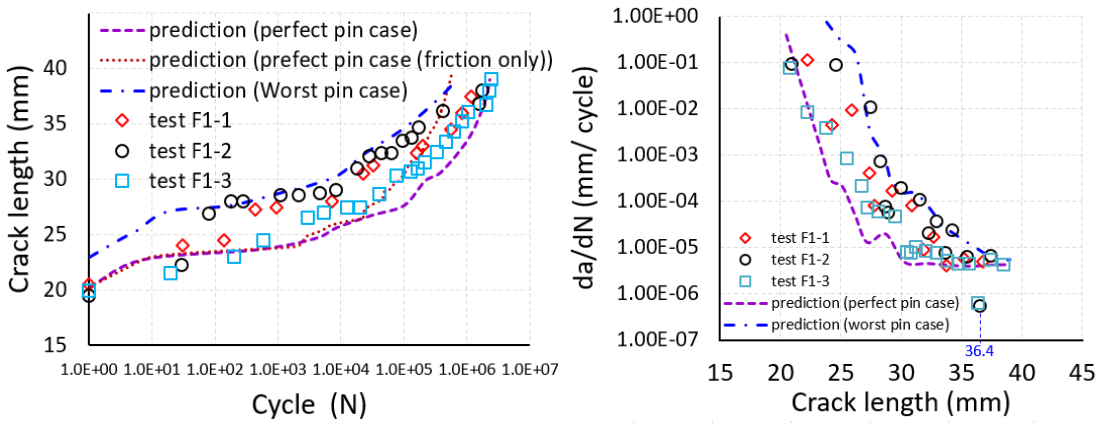

Fig. 7-6 Test group 1 (80% d_{Pmax}): experimental and predicted fatigue behaviour under maximum applied displacement of 22.7mm (a) crack length vs. cycle curve, (b) crack growth rate (da/dN) vs. crack length curve

The upper boundary (prefect case) predicts a slightly lower fatigue life compared with experimental

results at the early crack growth stage (<23 mm), after which the upper and lower boundary demonstrated good coverage with all the three test results. The d*a*/d*N* vs.crack length curve is plotted in Fig. 7-6b. The fatigue resistance of the specimens were gradually enhanced until crack reach around 30 mm whereas the large-scale bridging zone is completely formed.The steady-state of fatigue crack growth rate is about 2.2E-5 mm/cycle).

Pins' conditions are never perfect, hence it is expected that the upper bound of crack growth rate is lower than the experimental results. Nevertheless, the stable crack growth phase for all three cases are very close to the upper boundary, which suggest that the predicted perfect case overestimate the steady-state of crack growth rate. This is mostly due to the fitting parameters for the debonding and frictional degradation laws are obtained from [122] and [128] respectively. Since both pull-out specimens in [122] and [128] are simular to this work (CFRP / carbon fiber pin), the agreement between the prediction and experiment is reasonably good. A more accurate results can be predicted if the degradation laws are based on the identical laminate/ pin combination as used in experimental tests.

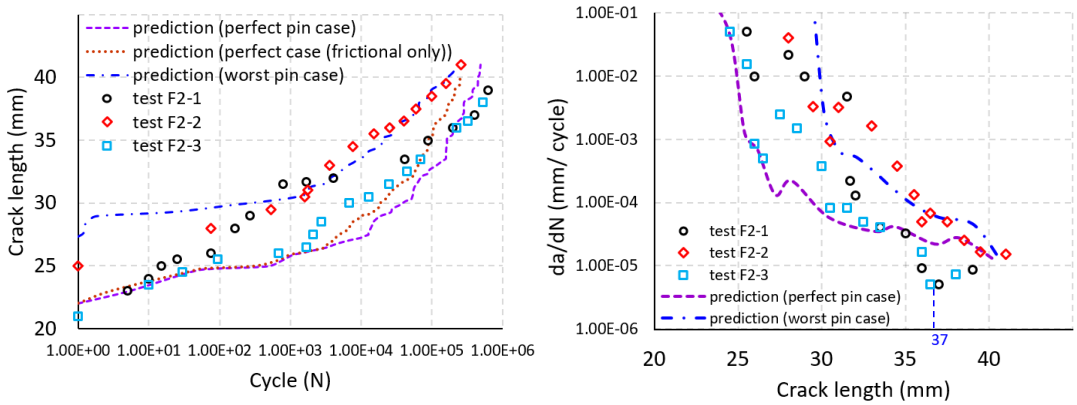

Fig. 7-7 Test group 2 (90% d_{Pmax}): experimental and predicted fatigue behaviour under maximum applied displacement of 25.7mm (a) crack length vs. cycle curve, (b) crack growth rate (d*a*/d*N*) vs. crack length curve

The test results and predicted bounds of test group 2 (F2-1, F2-2 and F2-3) are plotted in Fig. 7-7. Due to the relatively larger applied displacement, specimens failed before the fatigue crack growth rate reached a stable value. According to both figures, specimen F2-1 and F2-2 experience a quicker crack

propegation when the crack reaches 30 mm - 35 mm, compared to the lower bounds. This is mostly due to the misaligned pin breaked before completely degradation occur, providing the pins were subjected to relatively large applied displacement. This is more evident for first four pin row as shown in Fig. 7-8a for specimen F2-2.

Fig. 7-8 (a) F2-2 specimen after fatigue test (first four pin rows mostly breaked due to large applied displacement) (b) position of a pin at a = 36 mm resulting in abnormal data point in experiment results (Fig. 6b and Fig. 7b)

For static loading, the debonding stage of z-pin behaviour was often neglected during failure prediction, since it only provides a negligible contribution to the energy absorption. However, for fatigue loading, complete debonding of the pin is unlikely to occur in a very short period when the applied cyclic displacement is relatively small. Since z-pins are free to slide during the frictional pullout stage, the interface between the pin and matrix will wear out which lead to a more rapid fatigue-induced damage accumulation, compared to the debonding stage.

A prediction of upper boundary considering only frictional degradation was plotted in Fig. 7-6a and Fig. 7-7 Test group 2 (90% d_{Pmax}): experimental and predicted fatigue behaviour under maximum applied displacement of 25.7mm (a) crack length vs. cycle curve, (b) crack growth rate (da/dN) vs. crack length curve.

At the early crack growth stage (<26 mm), the prediction is very close to the one considering both debond and frictional degradation. This is due to the large displacement applied in first two pin rows, which lead to fully debond in very short period. After this, the difference between two predictions gradually increased up to 1.8 times (25.7mm applied displacement) and 4 times (22.7mm applied

displacement). This also suggest that the bonding behavior will sustain 75% of the total fatigue cycle under lower applied displacement.

It is worth noting that there is an abnormal point in Fig. 7-6b for both F1-2 and F1-3 cases whereas the crack length reach 36.4 mm. The crack growth rate at this point is ten times slower then the steady-state. Simular trend was found in Fig. 7-7b for F2-1 and F2-3 test specimens. It is appeared that the edge of those specimens are very close to z-pin. Thus, it becomes energetically more favorable for the crack to deviate from the path and meander through the pin region (Fig. 7-8b), providing the strain energy release rate is relatively small. This damage is found in the edge of 6th pin row (at a=29mm). According to the Fig. 7-9 (a=36mm) , the 6th pin row is just start to carry main part of load (Stage 2) which is consistent with the abnormal position in Fig. 7-6b and Fig. 7-7b.

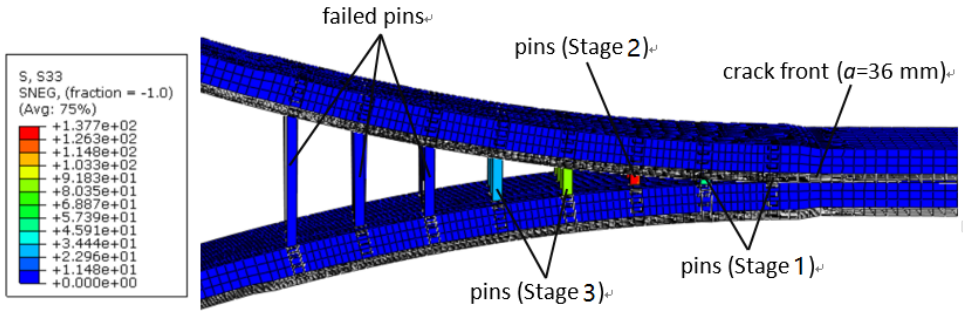

Fig. 7-9 Simulation results of deformed DCB when crack reach 36mm (deformation scale factor =3.0)

For the 22.7 mm applied displacement case, predicted degradation of each pin rows (perfect case) is presented in Fig. 7-10.

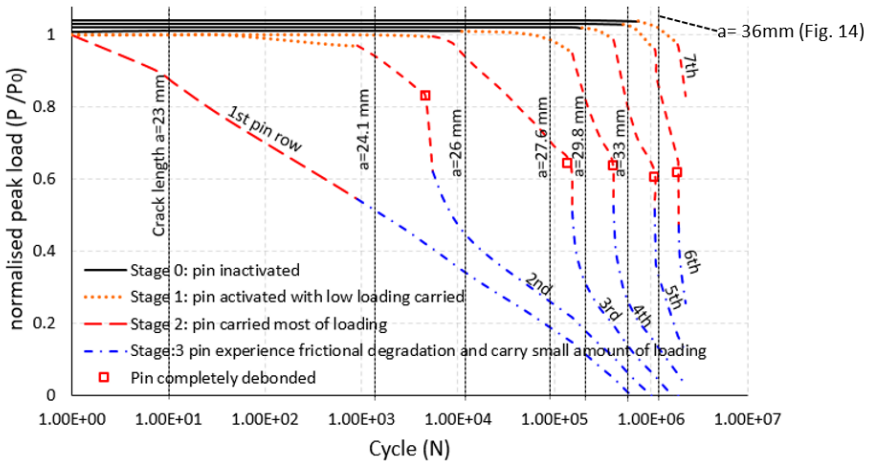

Fig. 7-10 Degradation of each pin rows under fatigue loading (perfect case)

During the fatigue crack propagation, pin experiences 4 stage: before crack reach pin location, pin is inactivated (Stage 0); When the crack pass pin location, pin experiences elastic stretching and carries small part of load (Stage 1); Pin experiences elastic stretching and carries main part of load (Stage 2); Pin fully debonded and carries small part of load (Stage 3). Under Stage 1, relatively small displacement is applied to the debonding degradation law, and therefore the degradation is very slow. When the pin starts to carry large part of load (Stage 2), relatively large displacement is applied to the debonding degradation law leds to a moderate degradation rate. After pin fully debonded (Stage 3), frictional degradation law is applied and therefore the residual peak load degrades rapidly.

The crack length corresponded to the fatigue life is also indicated by vertical line in Fig. 7-10. In the beginning (a <24 mm), only 3 pin rows were activated. The number of activated pin rows gradually increased to a steady-state (5 pin rows) after the fatigue crack reached 29.8mm. This is consistent with the da/dN vs. crack length curve (Fig. 7-6b) for crack length a =30mm where the fatigue crack growth rate reached a constant value, the crack tip entered the so-called “steady state of pin bridging ” zone.

7.3 Z-pin reinforced stiffener-to-skin joint

In this section, the fatigue life prediction methodology developed in Chapter 4 was expanded to a pin-reinforced composite hat joint subjected to a cyclic tensile (pull-off) load applied to the hat stiffener. It should be noted that composite hat joint is typically subjected to mixed mode loading in real aerospace application. Although VCCT and CZM can simulate debonding under mixed mode loading, mixed mode fatigue analysis require more data (e.g. mixed mode fatigue crack growth data for the laminate and single pin bridging law under mixed mode fatigue loading) which is not provided in the reference paper [121].

The simulation results for this special loading/geometry case reveals that only the first pin row (close to the corner) experienced relatively large mode II loading, and the rest of pins are subjected to mode I dominated loading ($G_I/G_{II} \geq 0.95$). Since the first pin row will fail quickly due to relatively large mode II loading, it contribute negligible bridging effect during fatigue analysis. Thus, to simplify the

fatigue life prediction procedure, the mode II strain energy release rate was treated as equivalent mode I component by a power law type mixed mode equation (as detailed in Section 7.3.2).

7.3.1 Specimen geometry, material properties, test condition and model description

The specimen geometry studied was chosen to match an example available in published literature in order to facilitate validation of the FE model. The data published by Hun Ji and Jin-Hwe Kweon [121] was selected as a suitable test study due to their clear description of their experimental details and presentation of extensive results. Their experimental data (some of which is presented in the chapter) has been used for model validation purposes only.

The geometry of the hat joint is shown in Fig. 7-11 (which has been reproduced from [121]). The specimens was made of unidirectional carbon-epoxy prepreg, USN-125B. The lay-up of the skin and stiffener were $[45/90/-45/0/45/0/-45]_{2S}$ and $[45/0/0/-45/90]_{2S}$, respectively. The nominal thickness of a layer after curing was 0.120 mm and the thickness of skin and stiffener were 3.36 mm and 2.4 mm respectively.

Fig. 7-11 Specimen configuration of pin-reinforced hat joint [121]

The elastic material properties for this material were presented by Nguyen et al at ICA-2016 [163], and are listed in Table 7-3.

Table 7-3 Material Property of USN-125B carbon-epoxy prepreg[163]

$\mathbf{E_{11}}$(GPa)	$\mathbf{E_{22}}$=$\mathbf{E_{33}}$(GPa)	$\mathbf{G_{12}}$=$\mathbf{G_{13}}$(GPa)	$\boldsymbol{\upsilon_{12}}$= $\boldsymbol{\upsilon_{13}}$

142	8.4	5.34	0.298

Fig. 7-12 Pinning pattern to prevent resin channels [121].

The specimens were reinforced by STS 304 stainless steel pins of 0.51mm diameter and 5.7mm length (pin area density A_p = 2%). To prevent resin channels being introduced by a straight pin line, the pins were positioned at an inclined angle of $22.5°$ with respect to the direction of the fibres, as shown in Fig. 7-12.

To improve the adhesion of the pins in the substrate, chemical surface treatments were applied before the insertion. The effect of this treatment upon the surface microstructure can be seen in Fig 7-13.

Fig. 7-13 SEM photographs of pins [121]. (a) without surface treatment. (b) with surface treatment.

The test setup used by Hun Ji and Jin-Hwe Kweon [121] is shown in Fig. 7-14. Both ends of the specimen were clamped, and the remaining length 160 mm of the specimen, between the clamping points was free to deform. Their fatigue tests were conducted using load control with the R ratio of 0.5, and the fatigue load applied to the joints was set between 55% and 90% of the maximum static strength of the joint.

Fig. 7-14 Photograph of test setup reproduced from [121].

Model description

In order to reduce the simulation time, only one half of the joint was modelled with a symmetrical boundary condition (Fig. 7-15).

Both the hat stiffener and skin were modelled as continuum shell elements (SC8R) to provide accurate bending response. After a mesh refinement study, a variable element size was used to accurately represent the behavior in the regions of interest without incurring an excessive computational cost. The element size of the unbonded area varies from 1.5 mm × 2 mm to 0.4 mm × 2 mm. For the bonded area, a finer mesh of 0.3 mm × 0.5 mm is applied.

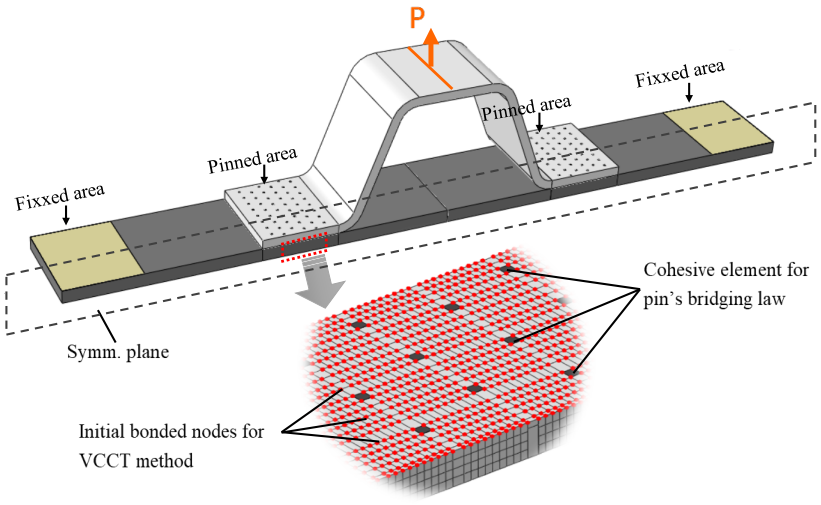

Fig. 7-15 FE model for pinned hat joint using half model. Note: Bonded areas are modelled by bonded nodes and VCCT to find G; Pins are modelled by Cohesive Zone Modelling (CZM).

Crack propagation in the interface between two adherends can be model by either VCCT or CZM approaches. However, to predict fatigue life by a fracture mechanic based approach, the strain energy release rate (G) must be determined. Thus, VCCT is selected to simulate crack propagation in the bonded area and CZM is used to represent the pins' bridging effect (Fig. 7-15). The fracture toughness (G_c) values in this analysis are 250 J/m^2 for mode I and 770 J/m^2 for mode II (using nominal values in [145]).

To reduce the computational time, square cross section elements were used to represent the pin's bridging effect in the meso-model, instead of circle cross section cohesive elements. As long as the total area of cohesive elements for a single pin remains the same, the bridging force per pin is equivalent. Since the pins are very small, the geometric effect can be neglected.

7.3.2 Results and discussion

Constitutive model for individual Z-pin subjected to mode I static loading

The typical results from pull-out test can be simplified to either a tri-linear (Fig. 4-2a) or a bi-linear (Fig. 4-2b) relation due to different bonding strength of pin/matrix interface. In this section, steel pins are used which can be represented by the bi-linear constitutive model.

The constitutive model used in this section is therefore modelled by a unit-cell FE model as illustrated in Fig. 4-4 . For the FE method, several parameters are required to calibrate with the experimental result before analysis (e.g. friction coefficient, stiffness). Unfortunately, those calibration data is not available in [121], and creating a simulation without these experimentally derived values is not useful as a predictive tool.

To obtain a reasonable bridging law, these parameters therefore been taken from other published papers [15], [164]. The values were then adjusted (by a small amount) so that the global pin-reinforced joint failed at the same (static) ultimate load as in [121], i.e. the values used in simulation have been reverse engineered to calibrate the model to Hun Ji and Jin-Hwe Kweon's experimental results [121].

According to both the published experimental photographs and the unpinned FE simulation result, the

failure mode is dominated by pull-out. To simplify the model, the pin is assumed to experience mode I loading only, and the detailed procedure is described below:

The friction coefficient used in this model is 0.75, which is the same as used in [145]. The material property of pin is the same as used in [164] for the steel pin. According to the experimental observation, a resin-rich pocket around the pin occurs due to pin insertion. Thus, the material surrounding the pin is assumed as homogeneous and isotropic using resin elastic property. The interface between upper and lower laminate is assumed completely failed and the pin bridging the only feature connecting the two parts.

In this model, a surface to surface algorithm was used to calculate the normal contact stress and the Coulomb friction.

$$\mathrm{F}_f \leq \mu \mathrm{F}_n \tag{7-4}$$

where F_f is the force of friction exerted by each surface on the other, μ is the coefficient of friction and F_n is the normal force exerted by each surface on the other.

A temperature change from cure to room conditions was applied to simulate the curing process and the thermal residual stresses were then calculated and saved in the model as the initial condition. Finally, a pull-out force is applied under the displacement controlled loading until the pin is completely pulled out. The result of the unit cell pull-out simulation is then plotted in Fig. 7-16.

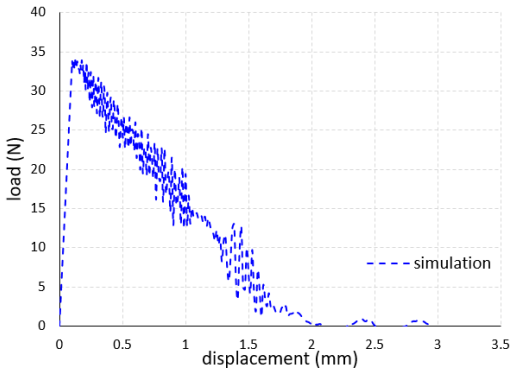

Fig. 7-16 The result of single pin pull-out test simulation

The stiffness of the simulation is very high (350 kN/m) and the displacement corresponding to P_f is

therefore very small (0.1mm). However, according to the experiment finding in most published papers, the stiffness lies in the range 100-200 kN/m and the displacement is 0.3-0.6mm. Most of these papers claim that the deformation is due to elastic stretch of pin and matrix, but according to the hand calculation, elastic deformation of pin and matrix is much smaller than 0.3-0.6mm.

Although a detailed investigation of this phenomenon is beyond the scope of this research project, one possible explanation possible reason is the area close to pin have plastic deformation. Another possible explanation could be non-linear debonding behavior of pin/matrix interface. Since no publications paper give a sufficiently robust explanation of this phenomenon, it is difficult to develop a model which incorporates this behavior during simulation. The stiffness value has therefore been selected based on experimental finding published in [164] for steel pin.

The peak frictional load P_f, stiffness and displacement were then represent by traction-separation law of cohesive element (Table 7-4) in the global structure:

$$\mathrm{T}(\delta) = \frac{P(\delta)}{A_{pin}} \tag{7-5}$$

where δ is the delamination opening displacement, A_{pin} is the total cross sectional area of the cohesive element for one pin, $\mathrm{T}(\delta)$ is the bridging stress in the cohesive law and $P(\delta)$ is the pin bridging force (derived from the unit-cell model).

Table 7-4 Cohesive parameters for pin-reinforced hat joint

$\boldsymbol{K_{pin}}(\mathbf{N/mm^3})$	$\boldsymbol{T_{pin}}$ **(MPa)**	$\boldsymbol{\delta}$ (mm)
740	131	2.03

Fig. 7-17 Joint failure [121] (complete pullout of half of the pin from the top-hat section)

The simulation reveals that the failure involves the complete pullout of half of the pin from the top-hat section, while the half of the pins inside flat skin is almost unmoved as shown in Fig. 4-1. This is mainly because the skin is thicker than the stiffener, and consequently there is greater friction holding the pin into the skin. Hun Ji and Jin-Hwe Kweon's experimental results [121] also show the same behavior, as shown in Fig. 7-17 which is reproduced from their paper.

Prediction of hat stiffener joint under static load

The load-displacement curves were then compared against the experiment results of [121]. The predicted peak load of both pinned/ unpinned specimens shows good agreement with those obtained experimentally [121], but the experimentally measured stiffness of the structure is only half that of the finite element prediction.

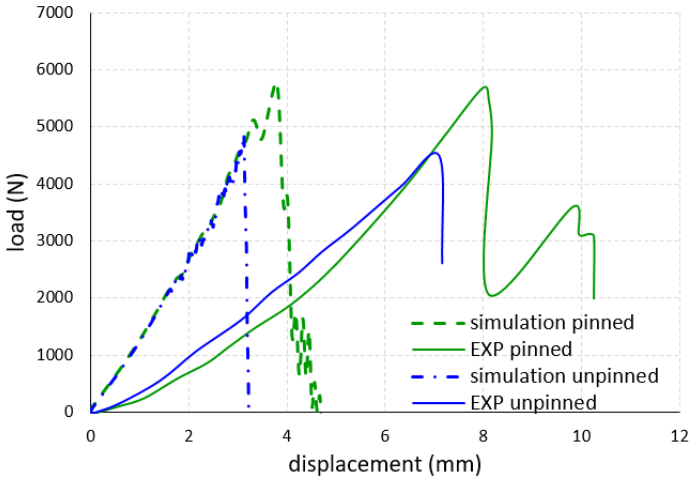

Fig. 7-18 load-displacement curve of pinned/unpinned hat joint

The stiffness of load-displacement curve mainly depends on three factors: geometry, elastic material properties and the boundary condition. The geometry of hat joint is exactly the same used in [121], and the boundary condition is very simple (pull out in stiffener and clamped on both side of skin). The material property is obtained from another paper in the open literature, which is trustworthy. Having double-checked the validity of all aspects of the FE model, an explanation was sought for this apparent discrepancy between the simulation and the experiment.

To demonstrate the deformed shape when applied displacement reach the 7.5mm (as plotted in Fig.

7-18 from [121]), the finite element analysis was re-run with an infinite value of fracture toughness in FE model. The deformed shape of the FE mesh is presented in Fig. 7-19 and this can be compared with the picture of the deformed shape from the experimental photograph of Hun Ji and Jin-Hwe Kweon in [121] which is reproduced in Fig. 7-19, and the crack stage highlighted reveals that this joint is close to shortly before failure. A clear difference can be found between those two pictures, which suggested the experimental photograph is not identical to the load- displacement curve plotted in [121].

Some materials have been removed due to 3rd party copyright. The unabridged version can be viewed in Lancester Library - Coventry University.

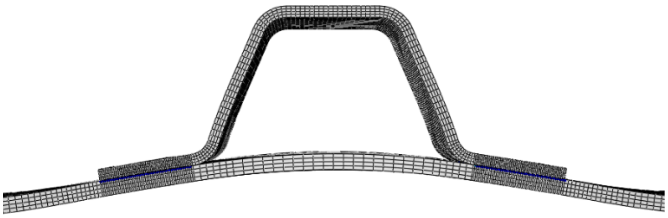

Fig. 7-19 Deformed hat joint (a). from experiment [121] (b) from FE (applied a displacement of 7.5mm in stiffener)

Furthermore, analysis of the FE simulation suggested that in order to apply 7.5mm displacement without failure, the model I fracture toughness value would need to be higher than 8000 J/m^2, which is unrealistic considering typical composite value (250 J/m^2 - 400 J/m^2). Further investigation is carried out by a digital scan of the experimental photograph in [121].

Some materials have been removed due to 3rd party copyright. The unabridged version can be viewed in Lancester Library - Coventry University.

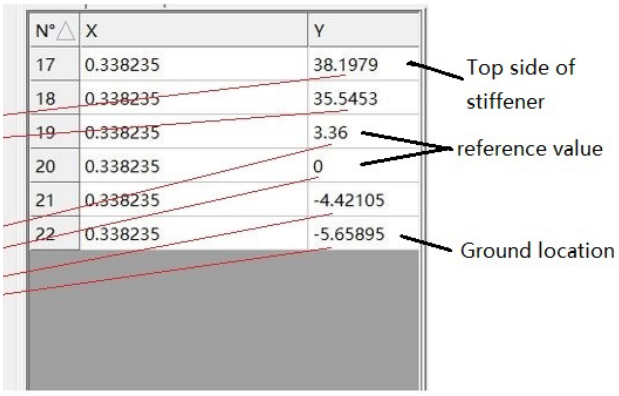

Fig. 7-20 Digital scan of deformed joint from [121]

The author uses the thickness of skin (3.36mm) as a reference and estimated the height of specimen after deformation: $H_{deformed} = 38.19 + 5.65 = 43.84$ mm. The displacement of stiffener can be

calculated by

$$\delta_{stiffener} = \mathrm{H}_{deformed} - H_{total} = 43.84\text{-}39.71 = 4.13 \text{ mm}$$

This value is very close to the author's prediction (3.87mm) and far from 7.5mm as plotted in the load-displacement curve.

There are many reasons could lead to the large difference between the displacement reported by Hun Ji and Jin-Hwe Kweon [121] and that which is calculated from their photograph. It is possible that the displacement recorded in crosshead differs from the displacement of the stiffener (for example if the loading rig had not been compliance compensated).

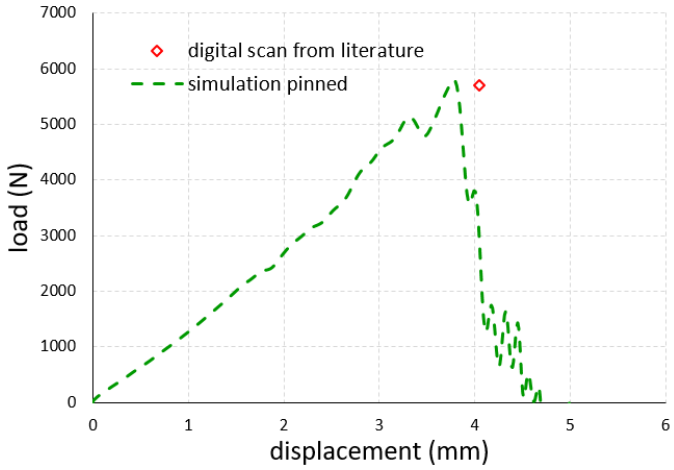

Fig. 7-21 Simulation of pinned hat joint against digital scan from [121]

Since the purpose of the current comparison between FE and experimental results is to validate the behavior of the joint, we consider that in light of the very good agreement between the simulation and the displacement of stiffener calculated from the digital scan, the FE model of pinned hat joint can be considered as validated and ready to be used in fatigue analysis.

Fatigue life prediction (considering friction degradation only)

For metal pins, the bonding behaviour can be ignored under static loading due to the lower debond force (P_d). Thus, a fatigue life prediction will be first carried out assuming that the pins only have frictional resistance during pull-out. The detailed procedure is shown in Fig. 7-23.

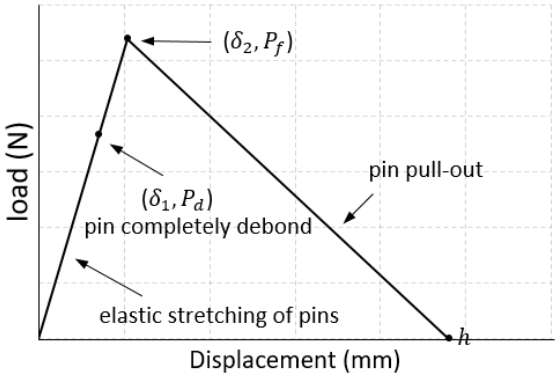

Fig. 7-22 Bi-linear Load-displacement curve of pin pull-out test

To predict fatigue life, the VCCT method is used to calculate strain energy release rate (G). The failure mode of the hat joint are dominated by mode I loading, to simplify the fatigue life prediction procedure, the mode II strain energy release rate obtained was then added to the mode I component by a power law type mixed mode equation:

$$G_I' = G_I + \frac{G_{II}}{G_{IIC}} G_{IC} \tag{7-6}$$

The equation simplifies the prediction from a mixed mode fatigue life prediction to a mode I prediction, and therefore only mode I fatigue crack growth data is required for the prediction. Since the fatigue crack growth data is not provided in [121], a normal carbon-epoxy value of C=12.922, M=6.5875 is used (data are chosen from [165] under mode I loading test). A sensitivity study is carried out to show that fatigue crack growth data from different composite material [159], [165-[167] will eventually led to a maximum difference of $\pm$30% in fatigue life. Considering the large scatter in common *S-N* curve, the difference is acceptable. A constant load is applied during fatigue test, the load selected in this simulation is 92%, 82%, and 72.5% of ultimate load in [121].

The experimental results available in [121] are S-N based curves, which include the stages of crack initiation and propagation in the total fatigue life. In contrast, the procedure in this chapter is based upon a fracture mechanics approach (a vs. N curve) which only consider the fatigue life of crack propagation.

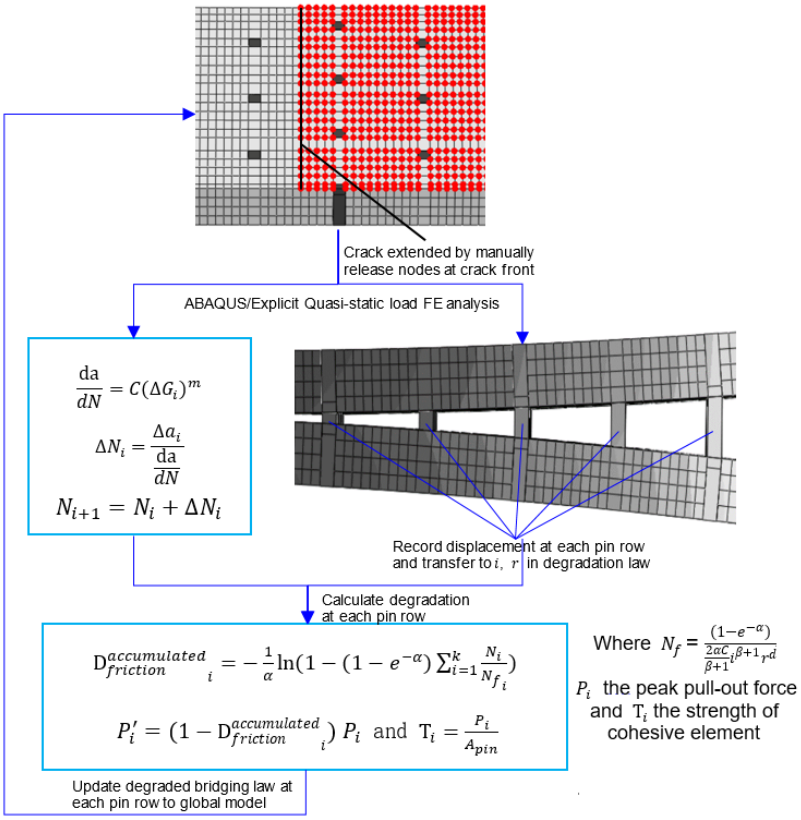

Fig. 7-23 Flow chart for fatigue life prediction of pin-reinforced hat joint

For unpinned hat joint, a large fraction of fatigue life are spent on crack initiation (e.g. 80%), and follow by quick crack propagation. Therefore, the difference of failure life between *S-N* curve and a-N curve is large.

However, the maximum fatigue force applied in pinned hat joint are 92%, 82%, and 72.5% of ultimate load under static test (5450 N, 4860 N and 4310 N respectively). For first two loading case, the applied force are larger than the ultimate strength of the unpinned specimen (4550 N), which means the crack is propagated as a static failure (i.e. before the predicted fatigue crack growth life). Thus, the fatigue life *N* in *S-N* curve should match *a-N* curve providing the prediction is reasonable.

For the lowest loading case (4310 N), a fraction of fatigue life is spent on crack initiation. According to the S-N data for unpinned specimens (Fig. 7-24), the crack will initiate within 1000 cycle which is a very small fraction compared to the failure life, thus, the *a-N* curve should give close results to *S-N* curve.

Fig. 7-24 S-N data from experimental test [121]

Based on the analysis above, the failure life in *S-N* curve was then transferred to the fatigue life while *a*=20mm (the end of crack propagation) for the purpose of validation.

The predicted fatigue life *N* were then plotted in Fig. 7-25 against crack length *a*.

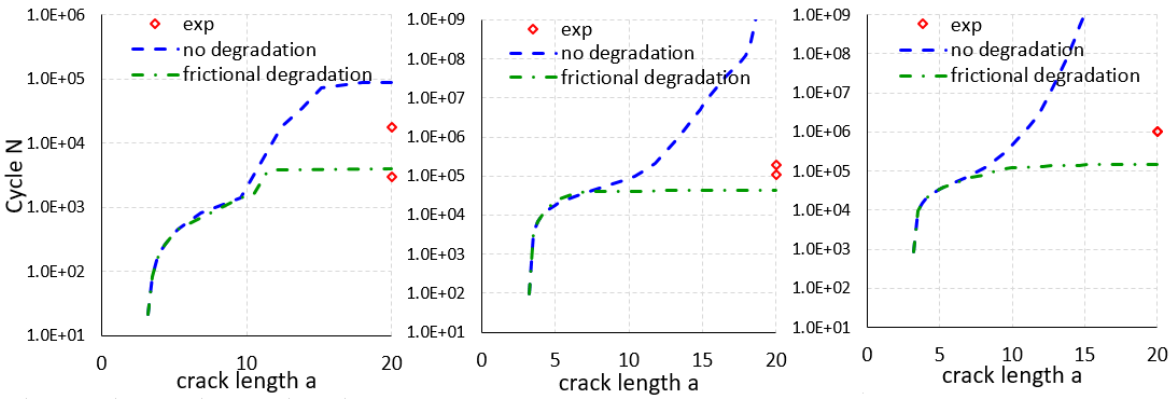

Fig. 7-25 *a* vs. N curve for (a) 92%, (b) 82%, (c) 72.5% of ultimate load

For all three loading cases, the predictions without a degradation law give unrealistic results (10 times higher than experimental data in the first case and thousands of times higher for later two cases).

The prediction with the frictional degradation law gives much closer results compared to the prediction without the degradation law. For 92% loading case, *N*= 3.98E+03 is in the range of experiment results (*N*= 3.01E+03~1.75E+04). For 82% ultimate load, *N*= 4.43E+04 is approximately 3 times smaller than experiment results (*N*= 1.06E+05~1.95E+05). For 72.5% ultimate load, *N*= 1.48E+05 is approximately 6 times smaller than experiment results (*N*= 1.0E+6).

Table 7-5 overview of prediction results

Fatigue load	*N* in experiment	Prediction (no degradation)	Prediction (friction only)
92% ultimate load	3.01E+03~1.75E+04	9.06E+04	3.98E+03
82% ultimate load	1.06E+05~1.95E+05	1.76E+09	4.43E+04
72.5% ultimate load	1.0E+6	3.36E+10	1.48E+05

In summary, the analysis without a pin degradation law will result in an unreasonably long predicted fatigue life. The prediction with frictional degradation law correctly predict the failure life at 92% ultimate load and underestimate approximately 3, 6 times fatigue life for 82% and 72.5 ultimate load respectively. Whilst the fatigue life is significantly under-predicted at the lower loads, at least the result is conservative and could be applied as a “lower bound” for design purposes.

A possible reason for large difference under 82% and 72.5% ultimate load is the debonding behavior. For the 92% loading case, due to the large applied displacement the pin will fully debond at early stage, and therefore the pin only experiences frictional behavior. This is why the prediction for 92% loading case is in the range of experiment data.

However, for lower loading case, the debond might not occur in early stage. Thus, the pin will experience the debonding degradation until it is fully debonded, and will only then undergo frictional degradation. According to [122], debonding degradation of pin/ interface is much slower than friction degradation under small fatigue loading. In order to attempt to improve the accuracy of the predictions at lower cyclic loads, another prediction was carried out which considered both debonding and friction degradation.

Fatigue life prediction (friction +debonding)

In order to improve upon the accuracy of the fatigue life prediction, a fatigue analysis was implemented which considered the effectof of both pin friction and debonding. The degradation law proposed for the bonding behavior is of a similar form to that used for frictional degradation only.

According to [164], the debond strength of the steel pin after surface treatment is about 7MPa. Since [121] also use the same surface treatment, the same strength value is used here. The debond force is

calculated by:

$$P_d = \tau_d \pi d_p l_p \tag{7-7}$$

where d_p and l_p are the diameter and length of pins, τ_d is the debond strength of pin/ interface.

$$\delta_d = \frac{P_d}{K} \tag{7-8}$$

where the K is same value used in section 4.3.

The calculated debond force for the hat joint is 26.9N which is smaller than the frictional failure force obtained in FE analysis (33N).

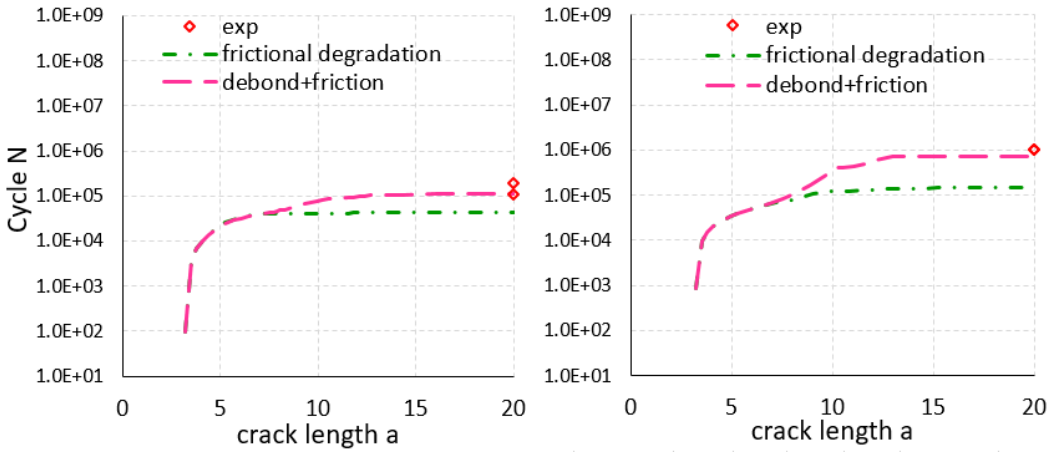

Fig. 7-26 Crack length vs. fatigue life curve under (a) 82% (b) 72.5% ultimate loading

The fatigue life prediction was then carried out with debond and friction degradation law. For the 90% loading case, the pin debonds at an early stage and therefore the debond behavior has negligible influence on fatigue life. Thus, only 82% and 72.5% loading case were carried out. The prediction results with both debond and friction degradation law were then plotted in Fig. 7-26. This time, both loading cases show good agreement compared with experimental results.

The *S-N* curve was also plotted against experimental data, good agreement was achieved for "friction+debond" prediction.

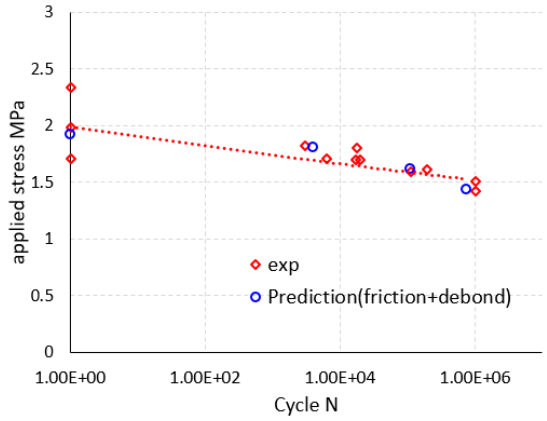

Fig. 7-27 *S-N* curve of pinned hat joints

Table 7-5 Overview of the fatigue life prediction

Fatigue load (% of ultimate load)	*N* in experiment	Prediction (friction only)	Prediction (friction and debonding)	Fraction of debond in total life
92%	3.01E+03~1.75E+04	3.98E+03	4.28E+03	7.1%
82%	1.06E+05~1.95E+05	4.43E+04	1.09E+05	59.4%
72.5%	1.0E+6	1.48E+05	7.45E+05	80.1%

Table 7-5 is a summary of prediction results. According to Table 7-5, when 82% ultimate load is applied, the bonding behavior can carry 59% of total fatigue life, and when 72.5% ultimate load is applied, the bonding behavior will sustain 80% of total fatigue cycle. Therefore, under cyclic loading that is not close to the static failure strength of the material, the bonding behavior cannot be ignored. This result also reveals that improving the bonding property can significantly improve fatigue performance under relatively small fatigue loading.

7.4 Conclusions

A method for predicting the fatigue life of pin-reinforced composites has been developed and applied to a pin-reinforced double cantilever beam and a pin-reinforced hat joint. An empirical degradation law based on damage mechanic has been proposed to describe the reduction of pin's bridging force under mode I fatigue loading. This law can account for damage accumulation of each pin row that is subjected to different displacement amplitude.

Pins bridging law under fatigue loading is fully defined assuming that the frictional peak load and

displacement will only be degraded when the pin is fully debonded. According to the prediction results, the bridging law only degrades with frictional behavior underestimates the fatigue life, especially for small applied displacement. This also highlight the importance of considering debonding behaviour during fatigue life prediction of pin-reinforced structure.

For z-pinned DCB, experimental validation is performed as well as the static pins pull-out tests which define the constitutive model of individual z-pin under static loading, as described in Chapter 5. Predictions show reasonablely good agreement with test results in term of crack length vs. fatigue life and fatigue crack growth rate vs. crack length relation under two different applied displacements. Assessing perfect pin insertion will give upper bound of life, whereas consider worst pin condiction will give lower bound of life prediction.

For z-pinned hat joint, a unit-cell model was developed to calculate the bridging force generated by a single pin. Since most of the necessary material properties were not provided in the benchmark paper used for model validation [121], other published values for similar laminate/pin behaviour have been obtained from the literature.The predictions show good agreement against experiment data across a range of cyclic loading amplitudes.

According to those prediction results, an accurate model of the pin briding behavior (particularly an appropriate degradation law) is crucial to the fatigue prediction procedure. It is noteworthy that the bonding behavior of pin/interface takes an increasingly important role under relatively small fatigue loading.

8. Conclusions and Suggestions for Further Work

8.1 Summary of work carried out in this PhD project

The work described in this Thesis has achieved the main objective of developing a methodology to predict the fatigue life of pin-reinforced bonded composite laminate and joints. The following paragraphs describe the main tasks that were undertaken in order to achieve this objective.

- Current literature has been reviewed (Chapter 2) to understand the current joint types and joining techniques, including mechanical fastening, adhesive bonding and hybrid joining technique, and their performance under the static and fatigue loadings. For pin reinforced bonded joints, several methods had already been developed to predict the behavior of z-pinned laminates and joints under static loads, but very little open literature was found for predicting the fatigue life of through-thickness reinforced structures that are realistic to be implemented into design analysis. Thus, the contribution of this PhD is to expand the progressive damage mechanics based approach for predicting the z-pin bridging force reduction under the fatigue load and to make the novel step of combining this with a fracture mechanics approach for predicting the disbond crack fatigue life of pin reinforced bonded joint. The theories of fracture mechanics and FE techniques used in this study are reviewed in Chapter 3.
- Key modelling skills (e.g. the VCCT, CZM) have been learnt and modelling methodologies developed based on the theoretical work described above. Model validation under static loads has been carried out for both unpinned and pinned specimen (Chapter 4), i.e. the relationships of load vs. applied displacement, crack extension vs. applied displacement and crack front strain energy release rate vs. crack extension were all used as comparators between model predictions and test results found in published literature. Most of them show good agreement (less than 5% error).
- Established fatigue crack growth life prediction methodology was applied to unpinned specimens (Chapter 4). The fatigue life of unpinned specimens (both DCB and ENF) has been validated by published test results, and reasonable agreement is achieved.
- Test specimens (single pin pull out and pinned DCB) were fabricated and tested (Chapter 5) in order to validate the models developed.
- A fatigue degradation law has been proposed by the candidate to describe the debonding and frictional pullout phases of a single pin's bridging force under mode I fatigue loading, which

is based on the damage mechanics approach with empirical fitting parameters (Chapter 6). The degradation law is shown to be capable of accurately capturing the pin's degradation behaviour under static loading (both the debonding and frictional pullout phases) compared to test results in the open literature. The proposed degradation law has been further modified so that it is capable of accumulating fatigue damage under varying displacement conditions experienced by each row of pins in the crack bridging zone during fatigue loading. The pin's bridging law under fatigue loading has been fully defined which assume that the peak frictional load and displacement only degrade once the pin fully debonded.

- The methodology to predict the fatigue life of pin-reinforced bonded joints has been developed and applied to a pin-reinforced DCB model and pin-reinforced hat stiffener joint (Chapter 7). For the DCB model, experimental validation tests are performed and the static single pin bridging law is directly deduced from pin pull-out tests. Two different fatigue loading levels are tested and the predictions show good coverage with test results in terms of crack length vs. fatigue life curve and fatigue crack growth rate vs. crack length curve. For the hat joint model, three different loading levels were considered and good agreement is achieved between the prediction and the test results presented in literature.
- The inevitable variation of pin insertion quality found in large scale fabrication was considered by two extreme scenarios: perfectly inserted pins and a percentage (according to quality control result) of imperfect pins which were assumed to be redundant. These two scenarios were considered to predict the upper and lower bounds of pinned specimen fatigue life.

8.2 Conclusions

The following sections summarise conclusions that can be drawn regarding both the general methods and techniques used in this project, and the specific complexities and details of the particular problem considered in this thesis.

8.2.1 Modelling of z-pin crack bridging effect

For pinned specimens, the rapid soften behavior of cohesive element at pin location can result in extremely small incremental size or convergence difficulties in ABAQUS/Standard analysis. Convergence study have been carried out to choose right parameters in nonlinear FE analysis. In addition, the traction-separation law in pin region have been slightly modified to reduce the solution

cost. The VCCT method was used to extract the strain energy release rate in the delamination crack tip. It was found that this novel combination of using CZM and VCCT worked well in this simulation.

8.2.2 Scatter factors of pinned specimen for large scale fabrication

Two scatter factors were found in the experimental tests of DCB specimens (Chapter 7), which signicantly affected the crack propagation rate under fatigue loading:

The first is that the specimen thickness ranged from 1.62 mm to 1.78 mm. Based on the test result of crack length vs. applied displacement, the largest difference of crack length under the same applied displacement is about 10 mm. This difference was found to be more distinct under fatigue loading than static loading, and therefore this must be considered for fatigue prediction.

The second factor is the difference of the pins' condition (i.e. manufacturing quality). Compared to a single pin pull-out test, the multiple-pins tests have averaged the effect of the pins' misalignment. In reality, the pin insertion condition will vary for large scale industrial fabrication. In this study, missing pins, shorter and thinner pins were found in the DCB specimens after the tests. Missing pins are mostly due to pin breaking before insertion, while shorter and thinner pins were resulted from internal transverse /shear damage during the pin insertion process. These two factors are considered in Chapter 7 by using two extreme scenarios to predict the upper and lower bounds of the fatigue life. The upper bound assumes every pin is perfectly inserted whereas the lower bound uses the worst pin condition of each pin row based on observations from specimens after fatigue tests.

8.2.3 Pin's bridging law under static loading

The bridging law exerted by an individual pin can be obtained from experimental tests or a unit-cell FE model. For the z-pinned hat joint model as described in Chapter 7, the static single pin bridging law was modelling by a unit-cell model with several limitations:

Firstly, the model assumed the pull-out resistance is caused only by the friction force. This assumption is close to the bi-linear bridging law observed in experimental tests, and is a good assumption when the friction strength is higher than debond strength. However, the debond strength is affected by many

factors which are difficult to count in FE model and therefore this model is less accurate for carbon pins and pins which experience chemical surface treatment such that the debond strength is higher than the friction strength.

Secondly, experiments must be carried out to define the coefficient of friction as an input parameter to the FE analysis. In addition, the unit-cell model overestimates the stiffness during elastic phase since the plastic deformation of the matrix material which occurs near pin region is not considered.

Nonetheless, modelling the degradation of the pin closure force as pin undergoes interfacial debond and frictional pull-out is of considerable value in understanding the micromechanics of the z-pin crack bridging.

8.2.4 Pin's bridging law under fatigue loading

When the pin-reinforced structure is subjected to fatigue loading, the pins are expected to experience both debonding and frictional degradation. The prediction methodology proposed here assumes that bond degradation occurs first and is then followed by the frictional degradation (i.e. pin pull-out). Based on the prediction results presented in Chapter 7, life prediction without a pin degradation law will result in unreasonable failure life (up to 1000 times longer than experimental data). Life prediction which only considers the frictional degradation law underestimates the fatigue life by a factor of approximately 3-6 for lower loading case.

The prediction with both friction and debonding degradation law shows good agreement compared with experiment data. According to the prediction, the pin bonding remains functional for a large fraction of total fatigue cycle (e.g. 80%) especially where the applied displacement is relatively small. In contrast, the frictional degradation (i.e. pin pull out) occurs relatively rapidly one the pin has debonded. Similar trends were found in reinforced joints (Chapter 7), which suggests that it is critical to accurately account for the pins' bonding degradation during fatigue analysis.

8.3 Future works

There are several potential ways to further improve the fatigue life prediction methodology proposed

in this thesis:

- The pin bridging law under fatigue loading developed in this thesis assumes that the frictional peak load and displacement are only degraded once the pin was fully debonded. However, a comprehensive experimental investigation would provide a better understanding of the friction/ debond behavior under fatigue loading. If such investigations indicate that frictional degradation occurs before the pin/interface is fully debonded, then the bridging law should be adjusted accordingly.
- The current methodology is limited to the mode I dominated joints (e.g. T joint, hat joint). However, it could be expanded to a wide range of mixed mode joints providing the degradation law of pin's bridging force under mixed mode fatigue loading is characterised and fully understood by experimental study.
- The fitting parameters for the debonding and frictional degradation laws are currently derived from two separate papers [15, 25]. A more accurate result could be predicted if the degradation laws are based on the identical laminate/ pin combination as used in the experimental tests. Furthermore, only two combination of pin's average / amplitude displacement have been tested in [15] to determine the debonding degradation law. Better fitting parameters could be obtained if more data were available.
- The bonding behavior of the pins is usually ignored under static loading due to its negligible contribution to the energy absorption. However, the degradation of bonding strength is much slower than the degradation of friction under fatigue loading. According to the prediction in Chapter 6, the bonding behavior will sustain a large fraction of total fatigue cycle (e.g. 80%) especially in cases where the applied displacement is relatively small.

  Thus, in order to improve the fatigue performance of z-pinned bonded joints, it is recommended to study bonding quality and develop methods to improve the bonding quality (e.g. surface treatment) in manufactured joints. Furthermore, the fatigue performance of any given joint design could also be maximized by developing design guidance that only allows the pins to be subjected to small displacements. This will improve fatigue performance significantly.

  Whilst the extent of any improvement would need to be validated by experimental results, it is anticipated that an improvement in pin bonding behavior, and appropriate constraints upon

the duty cycles to which such joints are subjected will lead to potentially significant improvements in the fatigue life of pin-reinforced joint structures.

REFERENCES

[1] http://www.defenseindustrydaily.com/Grant-Thornton-on-US-Aerospace-Component-MA-2008-05334/

[2] https://epoxy-europe.eu/en/spotlight/high-flying-epoxies/

[3] Kruse T. Bonding of CFRP primary aerospace structures: overview in the technology status in the context of the certification boundary conditions addressing needs for development. In: Proceedings of the 19th international conference on composite materials (ICCM/19). Montreal; 2013. p. 5635–43.

[4] U.S. Department of Transportation – Federal Aviation Administration (FAA). Advisory circular 20-107B subject: composite aircraft structure. FAA; 2010.

[5] Casas-Rodriguez JP, Ashcroft IA, Silberschmidt VV. Damage in adhesively bonded CFRP joints: sinusoidal and impact-fatigue. Compos Sci Technol 2008;68(13):2663–70.

[6] Ashcroft IA, AbdelWahab MM, Crocombe AD, Hughes DJ, ShawSJ. The effect of environment on the fatigue of bonded composite joints. Part 1: testing and fractography. Compos Part A 2001;32(1):45–58.

[7] Datla NV, Papini M, Schroeder JA, Spelt JK. Modified DCB and CLS specimens for mixed-mode fatigue testing of adhesively bonded thin sheets. Int J Adhes Adhes 2010;30(6):439–47.

[8] Pethrick RA. Design and ageing of adhesives for structural adhesive bonding – a review. Proc IMechE Part L: J Mater: Des Appl 2015;229:349–79

[9] Sachse, R, Picket, AK, Käß, M, Middendorf P. Numerical simulation of fatigue crack growth in the adhesive bondline of hybrid CFRP joints. In: Proceedings of the conference on the mechanical response of composites (ECCOMAS). Bristol; 2015.

[10] Kruse T, Körwien T, Heckner S, Geistbeck M. Bonding of primary aerospace structures – crackstopping in composite bonded joints under fatigue. In: Proceedings of the 20th international conference on composite materials (ICCM/20). Copenhagen; 2015

[11] Stelzer S, Ucsnik S, Pinter G. Composite-composite joining with through the thickness reinforcements for enhanced damage tolerance. Mater Sci Forum 2015;825–826:883–90

[12] Shakirov, A, Sergei B. Sapozhnikov Member, IAENG, Sergei D. Vaulin, Experimental and FE analysis of Bonded Single-lap Joints Strengthened by Self-tapping Screws, Proceedings of the World Congress on Engineering 2015 Vol II WCE 2015, July 1 - 3, 2015, London, U.K.

[13] Heimbs S, Nogueira A, Hombergsmeier E, May M, Wolfrum J. Failure behaviour of composite

T-joints with novel metallic arrow-pin reinforcement. Compos Struct 2014;110:16–28.

[14] Löbel T, Kolesnikov B, Scheffler S, Hühne C. Enhanced tensile strength of composite joints by using staple-like pins: working principles and experimental validation. Compos Struct 2013; 106: 453–60

[15] F. Pegorin, K. Pingkarawat, A.P. Mouritz, Comparative study of the mode I and mode II delamination fatigue properties of z-pinned aircraft composites, Materials and Design 65 (2015) 139–146 Contents

[16] Myung-Gyun Ko, Jin-Hwe Kweon ,Jin-Ho Choi, Fatigue characteristics of jagged pin-reinforced composite single-lap joints in hygrothermal environments, Composite Structures 119 (2015) 59–66

[17] Lin CY, Chen WS. Stiffness of composite laminates with z-fiber reinforcement. In: Proceedings of the 40th AIAA/ASME/ASCE/AHS/ASC structures, structural dynamics, and materials, vol. 99; 1999. p. 918–24

[18] Cox, B.N., Sridhar, N., 2002. A traction law for inclined tows bridging mixed-mode cracks. Mech. Compos. Mater. Struct. 9, 299–331.

[19] Grassi, M., Zhang, X., 2003. Finite element analyses of mode I interlaminar delamination in Z-fibre reinforced composite laminates. Compos. Sci. Technol. 63 (12), 1815–1832.

[20] P.N. Parkes a, R. Butler, Static strength of metal-composite joints with penetrative reinforcement, Composite Structures 118 (2014) 250–256

[21] W. Tu, P.H. Wen, Optimisation of the protrusion geometry in Comeld™ joints, Composites Science and Technology 71 (2011) 868–876

[22] Allegri, G., Zhang, X., 2004. Delamination/debond growth in Z-fibre reinforced composite T-joints: a Finite element simulation. In: Proceedings of the ECCM- 11 Conference, Rhodes, Greece, May 31–June 3

[23] F. Bianchi, X. Zhang, Composites Science and Technology 71 (2011) 1898–1907.

[24] F. Bianchi, X. Zhang, Composites Science and Technology 72 (2012) 924–932.

[25] F.L. MATTHEWS (1990), “Composite Materials in Aircraft Structures, Chapter 9”

[26] D5766/D5766-02a Standard Test Method for Hole Tensile Strength of Polymer-matrix Composite Laminates, volume 15.03. ASTM International, 2007

[27] D6484/D6484M-04 Standard Test Method for Compressive Strength of Polymer- matrix Composite Laminates, volume 15.03. ASTM International, 2004.

[28] D6742/D6742-02 Standard practice for Filled-hole Tension and Compression Testing of Polymer-matrix Composite Laminates, volume 15.03. ASTM International, 2007.

[29] D5961/D5961M-05e1 Standard Test Method for Bearing Response of Polymer-matrix Composite Laminates, volume 15.03. ASTM International, 2005.

[30] D6873-03 Standard practice for Bearing Fatigue Response of Polymer-matrix Composite Laminates, volume 15.03. ASTM International, 2003.

[31] Military Handbook – MIL-HDBK-17-3F: Composite Materials Handbook. Vol. 3. Polymer–Matrix Composites Materials Usage, Design, and Analysis US. Department of Defense.

[32] Portanova MA. Standard methods for unnotched tension testing of textile composites. NASA CR 198264 1995. December.

[33] Portanova MA, Masters JE. Standard methods for open hole tension testing of textile composites. NASA CR 198262 1995. December.

[34] Portanova MA. Standard methods for filled hole tension testing of textile composites. NASA CR 198263 1995. December.

[35] Portanova MA. Standard methods for bolt-bearing testing of textile composites. NASA CR 198266 1995. December

[36] Camanho PP, Lambert MA. Design methodology for mechanically fastened joints in laminated composite materials. Composite Science Tech 2006; 66(15): 3004–20.

[37] Ireman T, Nyman T, Hellbom K. On design methods for bolted joints in composite aircraft structures. Compos Struct 1993; 25(1-4):567–78.

[38] Zhang JM. Design and analysis of mechanically fastened composite joints and repairs. Eng Anal Boundary Elements 2001; 25(6):431–41.

[39] Dano M-L, Kamal E, Gendron G. Analysis of bolted joints in composite laminates: strains and bearing stiffness predictions. Compos Struct 2007; 79(4):562–70.

[40] Arnold WS, Marshall IH, Wood J. Optimum design considerations for mechanically fastened composite joints. Compos Struct 1990; 16(1-3): 85–101.

[41] Matuszewski J. Fastener guidelines for composite materials. Mater Technol (UK) 2004; 19(4):203–10.

[42] Pierce B. Selecting the right fastener for use in plastics. Am Fastener J 1998; 5:32–3.

[43] Kagan VA, Weitzel SP. Basic principles in materials selection for mechanical fastening of

thermoplastics. J Reinforced Plastics Compos 2003; 22(16):1455–65.

[44] Cooper C, Turvey GJ. Effects of joint geometry and bolt torque on the structural performance of single bolt tension joints in pultruded GRP sheet material. Compos Struct 1995;32(1-4):217–26.

[45] Sun HT, Qing X, Chang F-K. The response of composite joints with bolt- clamping loads, part II: model verification. J Compos Mater 2002;36(1): 69–91.

[46] Khashaba UA, Sallam HEM, Al-Shorbagy AE, Seif MA. Effect of washer size and tightning torque on the performance of bolted joints in composite structures. Compos Struct 2006;73(3):310–7.

[47] McCarthy MA, Lawlor VP, Stanley WF, McCarthy CT. Bolt-hole clearance effects and strength criteria in single bolt, single lap, composite joints. Compos Sci Technol 2002;62(10-11):1415–31.

[48] L.R. Pitrone, S. R. Brown, “Environmental Durability of Adhesively Bonded Joints,” Adhesively Bonded Joints: Testing, Analysis, and Design, ASTM STP 981, W, S, Johnson, ED. , American Society for Testing and Materials, Philadelphia, 1988,pp. 289-303

[49] F.L. MATTHEWS, P.F. KIL TY and E.W. GODWIN, 1982. “A review of the strength of joints in fiber reinforced plastics”, Composites, vol.13, no.1, pp. 29–37.

[50] Goland M, Reissner E. The stresses in cemented joints. J Appl Mech 1944;11:A17–A27.

[51] Sancaktar E, Lawry P.Aphotoelastic study of the stress distribution in adhesively bonded joints with prebent adherend. J Adhes 1980;11: 233–41.

[52] Hart-Smith L, Bunin B. Selection of taper angles for doubles, splices and thickness transition in fibrous composite structures. Douglas Paper 7299, McDonnell Douglas Corporation; 1983.

[53] Adams R, Atkins R, Harris J, Kinloch A. Stress analysis and failure properties of carbon-fiber reinforced-plastic/steel double lap joints. J Adhes 1986;20:29–53.

[54] Goland M, Reissner E. The stresses in cemented joints. J Appl Mech 1944;11:17–27.

[55] Hart-Smith LJ. Adhesive bonded single lap joints. Hampton, VA: Langley Research Center; 1973 (NASA report CR-112236).

[56] Oplinger DW. Effects of adherend deflectıons in single lap joints. Int J Solids Struct 1994;3:2565–87.

[57] Adams RD, Peppiatt NA. Effect of Poisson's ratio strains in adherends on stresses of an idealized lap joint. J Strain Anal 1973;8:134–9.

[58] Adams RD, Peppiatt NA. Stress analysis of adhesive-bonded lap joints. J Strain Anal 1974;9:185–96

[59] Adams RD. Theoretical stress analysis of adhesively bonded joints. In: Mathews FL, editor. Joining of fiber-reinforced plastics. Amsterdam: Elsevier; 1987. p. 185–226 [chapter 5].

[60] Vinson JR, Sierakowski RL. Joints. The behavior of structures composed of composite materials. In: Przemieniecki JS, Oravas GAE, editors. Mechanics of structural systems series. Dordrecht, The Netherlands: Martinus Nijhoff Publishers; 1985. p. 239–83 [Chapter 8].

[61] Wooley GR, Carver DR. J Aircraft 1971; 8:817.

[62] Adams RD, Harris JA. Influence of local geometry on the strength of adhesive joints. Int J Adhes Adhes 1987;7(2): 68–80.

[63] Adams RD, Atkins RW, Harris JA, Kinloch AJ. Stress analysis and failure properties of carbon-fibre reinforced plastic/steel double lap-joint. J Adhes 1986; 20:29–33.

[64] Barker RM, Hatt F. Analysis of bonded joints in vehicular structures. AIAA Journal 1973;11(12):1650.

[65] Lin C-C, Lin Y-S. Finite element model of single-lap adhesive joints. International Journal of Solids and Structures 1993;30(12):1679.

[66] Andruet RH, Dillard DA, Holzer SM. Two and three dimensional geometrical nonlinear finite elements for analysis of adhesive joints. International Journal of Adhesion and Adhesives 2001;21(1):17.

[67] Hart-Smith LJ. Design methodology for bonded-bolted composite joint. Technical Report AFWAL-TR-81-3154. Douglas Aircraft Company; 1982.

[68] Gang Li, Fatigue performance characterization of a composite butt joint configuration, Composites: Part A 51 (2013) 43–55 Contents

[69] Kelly G. Load transfer in hybrid (bonded/bolted) composite single-lap joints. Compos Struct 2005;69:35–43.

[70] Kelly G. Quasi-static strength and fatigue life of hybrid (bonded/bolted) composite single-lap joints. Compos Struct 2006;72:119–29.

[71] Kweon J-H, Jung J-W, Kim T-H, Choi J-H, Kim D-H. Failure of carbon compositeto-aluminum joints with combined mechanical fastening and adhesive bonding. Compos Struct 2006;75:192–8.

[72] Di Franco G, Fratini L, Pasta A. Analysis of the mechanical performance of hybrid (SPR/bonded) single-lap joints between CFRP panels and aluminum blanks. Int J Adhes Adhes 2013;41:24–32.

[73] Marannano G, Zuccarello B. Numerical experimental analysis of hybrid double lap aluminum-CFRP joints. Compos B Eng 2015;71:28–39.

[74] Chan WS, Vedhagiri S. Analysis of composite bonded/bolted joints used in repairing. J Compos Mater 2001;35:1045–61.

[75] Maofeng Fu, Fatigue of hybrid (adhesive/bolted) joints in SRIM composites, International Journal of Adhesion & Adhesives 21 (2001) 145}159

[76] Paroissien E, Sartor M, Huet J, Lachaud F. Hybrid (bolted/bonded) joints applied to aeronautic parts: analytical two-dimensional model of a single-lap joint. J Aircr 2007;44(2):573–82.

[77] Bois C, Wargnier H, Wahl J, Le Goff E. An analytical model for the strength prediction of hybrid (bonded/bolted) composite joints. Compos Struct 2013;117:354–61.

[78] Hoang-Ngoc CT, Paroissien E. Simulation of single-lap bonded and hybrid (bolted/bonded) joints with flexible adhesive. Int J Adhes Adhes 2010;30 (3):117–29.

[79] Kelly G. Load transfer in hybrid (bonded/bolted) composite single-lap joints. Compos Struct 2005;69(1):35–43.

[80] Anders Sjo ¨gren , Leif E. Asp, Effects of temperature on delamination growth in a carbon/epoxy composite under fatigue loading, International Journal of Fatigue 24 (2002) 179–184

[81] Chen HS. The static and fatigue strength of bolted joints in composites with hygrothermal cycling. Compos Struct 2001;52:295–306.

[82] Counts WA, Johnson WS. Bolt bearing fatigue of polymer matrix composites at elevated temperature. Int J Fatigue 2002;24:197–204.

[83] Starikov R, Schon J. Fatigue resistance of composite joints with countersunk composite and metal fasteners. Int J Fatigue 2002;24(1):39–47.

[84] Jingchao Wei, The effect of interference fit size on the fatigue life of bolted joints in composite laminates, Composites: Part B 53 (2013) 62–68 Contents

[85] Ishii K, Imanaka M, Nakayama H, Kodama H. Evaluation of the fatigue strength of adhesively bonded CFRP/metal single and single-step double-lap joints. Compos Sci Technol 1999;59:1675–83.

[86] Zeng Q, Sun CT. Fatigue performance of a bonded wavy composite lap joint. Fatigue Fract Eng Mater Struct 2004;27:413–22.

[87] H.S. da Costa Mattos, Failure analysis of adhesively bonded joints in composite materials, Materials and Design 33 (2012) 242–247

[88] Yi-Ming Jen, Fatigue life evaluation of adhesively bonded scarf joints, International Journal of Fatigue 36 (2012) 30–39

[89] S.M.R. Khalili, Experimental study of the influence of adhesive reinforcement in lap joints for composite structures subjected to mechanical loads, International Journal of Adhesion & Adhesives 28 (2008) 436– 444

[90] Z. Yang, K. Zhang, Y. Ma, and Y. Li, Orthogonal test research on the effect of curing technology on the fatigue life of adhesive bonding of CFRP and aluminum alloy, Advanced Materials Research, vol. 181-182, pp. 534–539, 2011

[91] Johnson WS, Mall S. Influence of interface ply orientation on fatigue damage of adhesively bonded composite joints. J Compos Technol Res 1986;8:3–7.

[92] De Goeij WC, Van Tooren MJL, Beukers A. Composite adhesive joints

[93] Ashcroft IA, Abdel Wahab MM, Crocombe AD, Hughes DJ, Shaw SJ. The effect of environment on the fatigue of bonded composite joints. Part 1: testing and fractography. Composites A 2001;32:45–58.

[94] Mall S, Ramamurthy G, Rezaizdeh MA. Stress ratio effect on cyclic debonding in adhesively bonded composite joints. Compos Struct 1987; 8:31–45.

[95] Erpolat S, Ashcroft IA, Crocombe AD, Abdel Wahab MM. Fatigue crack growth acceleration due to intermittent overstressing in adhesively bonded CFRP joints. Composites A 2004;35:1175–83.

[96] Mall S, Ramamurthy G. Effect of bond thickness on fracture and fatigue strength of adhesively bonded composite joints. Int J Adhes Adhes 1989;9:33–7.

[97] S. Azari, M. Papini, J.K. Spelt, Effect of adhesive thickness on fatigue and fracture of toughened epoxy joints – Part I: Experiments, Engineering Fracture Mechanics 78 (2011) 153–162

[98] V. Shenoy, I.A. Ashcroft, G.W. Critchlow A.D. Crocombe, M.M. Abdel Wahab, Strength wearout of adhesively bonded joints under constant amplitude fatigue, International Journal of Fatigue 31 (2009) 820–830

[99] Paris P, Erdogan F. A critical analysis of crack propagation law. J Basic Eng, Trans ASME 1963:528–34

[100] M.M. Abdel Wahaba, I.A. Ashcroftb, A.D. Crocombea, P.A. Smitha, Finite element prediction of fatigue crack propagation lifetime in composite bonded joints, Composites: Part A 35 (2004) 213–222

[101] M.F.S.F. de Moura, Development of a cohesive zone model for fatigue/fracture characterization of composite bonded joints under mode II loading, International Journal of Adhesion & Adhesives 54 (2014) 224–230 Contents

[102] Mouritz, a. P. (2007). Review of z-pinned composite laminates. Composites Part A: Applied Science and Manufacturing, 38(12), 2383–2397

[103] Darbyshire HF. Report, Report No.: BDX-613-144. Bendix Aerospace-

Electronics Company, 1970.

[104] Bradshaw FJ, Dorey G, Sidey GR. Impact resistance of carbon fiber reinforced plastics. Technical Report, Report No.: 72240. Royal Aircraft Establishment, Farnborough, 1973.

[105] L. C. Dickinson, G. L. Farley, and M. K. Hinders, "Translaminar Reinforced Composites: A Review," Journal of Composites Technology and Research, Vol. 21, Issue 1, 1999, pp. 3-15.

[106] Boyce JS, Freitas GA, Magee CL, Fusco TM, Harris JJ, Kunkle E. Ultrasonic fastening system and method. Patent WO 98/29243 1998

[107] Q.Song, Y.Li, J. QI, Study on an automatic multi-pin insertion system for preparing Z-pin composite laminates, Chinese Journal of Aeronautics, 2014:27(2): 413-419

[108] Dantuluri, V., Maiti, S., Geubelle, P. H., Patel, R., & Kilic, H. (2007). Cohesive modeling of delamination in Z-pin reinforced composite laminates. Composites Science and Technology, 67(3-4), 616–631. doi:10.1016/j.compscitech.2006.07.024

[109] Partridge IK, Cartié DDR. Delamination resistant laminates by Z-Fiber pinning: Part I manufacture and fracture performance. Compos Part A Appl Sci Manuf 2005;36:55–64.

[110] Cartié DDR, Partridge IK. Delamination behaviour of Z-pinned laminates. In: Proceedings of the 12th international conference on composite materials, 5–9 July 1999, Paris.

[111] Liu H-Y, Yan W, Yu X-Y, Mai Y-W. Experimental study on Z-pinned DCB mode I delamination. Struct Integr Fract 2004.

[112] Dai S-C, Yan W, Liu H-Y, Mai Y-W. Experimental study on Z-pin bridging law by pullout test. Compos Sci Technol 2004;64:2451–7.

[113] Cartié DDR. Effect of Z-FibresTM in the delamination behaviour of carbon fibre/ epoxy laminates [PhD thesis]. Cranfield University; 2000.

[114] Cartié DDR, Laffaille J-M, Partridge IK, Brunner AJ. Fatigue delamination behaviour of unidirectional carbon fibre/epoxy laminates reinforced by ZFiber pinning. Eng Fract Mech 2009;76:2834–45.

[115] Byrd LW, Birman V. The estimate of the effect of Z-pins on the strain release rate, fracture and fatigue in a composite co-cured Z-pinned double cantilever beam. Compos Struct 2005;68:53–63.

[116] Yan W, Liu H-Y, Mai Y-W. Mode II delamination toughness of Z-pinned laminates. Compos Sci Technol 2004;64:1937–45.

[117] Freitas G, Magee C, Dardzinski P, Fusco T. Fibre insertion process for improved damage tolerance in aircraft laminates. J Adv Mater 1994;25:36–43.

[118] Cartie DDR. Effects of z-fibres on the delamination behaviour of carbon fibre/epoxy laminates. PhD Thesis, Cranfield University, 2000

[119] Chang P, Mouritz AP, Cox BN. Properties and failure mechanisms of pinned composite lap joints in monotonic and cyclic tension. Compos Sci Technol 2006;66(13):2163–76.

[120] Heimbs S, Nogueira AC, Hombergsmeier E, May M, Wolfrum J. Failure behaviour of composite T-joints with novel metallic arrow-pin reinforcement. Compos Struct 2014;110:16–28.

[121] Hun Ji, Jin-Hwe Kweon, Fatigue characteristics of stainless steel pin-reinforced composite hat joints, Composite Structures 108 (2014) 49–56

[122] Zhang AY, Liu HY, Mouritz AP, Mai YW. Experimental study and computer simulation on degradation of z-pin reinforcement under cyclic fatigue. Compos A Appl Sci Manuf 2008;39(2):406–414.

[123] Pegorin, F. et al., 2015. Influence of z-pin length on the delamination fracture toughness and fatigue resistance of pinned composites. Composites Part B: Engineering, 78, pp.298–307.

[124] Son HG, Park YB, Kweon JH, Choi JH. Fatigue behaviour of metal pin-reinforced composite single-lap joints in a hygrothermal environment. Compos Struct 2014;108:151–60

[125] Myung-Gyun Ko, Fatigue characteristics of jagged pin-reinforced composite single-lap joints in hygrothermal environments, Composite Structures 119 (2015) 59–66 Contents

[126] P. Chang, A.P. Mouritz, Properties and failure mechanisms of pinned composite lap joints in monotonic and cyclic tension, Composites Science and Technology 66 (2006) 2163–2176

[127] A-Ying Zhang, Hong-Yuan Liu, Adrian P. Mouritz, Yiu-Wing Mai, Experimental study and computer simulation on degradation of z-pin reinforcement under cyclic fatigue, Composites: Part A 39 (2008) 406–414

[128] F. Warzok, G. Allegri, M. Gude, S.R. Hallett, Experimental characterisation of fatigue damage in single Z-pins, Composites: Part A xxx (2016) xxx–xxx

[129] J. R. Reeder, J. H. Crews, Mixed-Mode Bending Method for Delamination Testing, AIAA J. 28 (1990) 1270–1276.

[130] Benzeggagh ML, Kenane M. Measurement of mixed-mode delamination fracture toughness of

unidirectional glass/epoxy composites with mixed mode bending apparatus. Compos Sci Technol 1996; 56:439–49.

[131] Reeder JR. 3D mixed mode delamination fracture criteria – an experimentalist's perspective. In: Proceedings of American Society for Composites, 21st annual technical conference, Dearborn, MI, United States, 17–20 September; 2006.

[132] Kanninen, M. F. and Popelar, C. H., Advanced Fracture Mechanics (Oxford University Press, Oxford, 1985).

[133] ATSM D5528, Standard Test Method for Mode I Interlaminar Fracture Toughness of Unidirectional Fiber-Reinforced Polymer Matrix Composites, Designation: D 5528 – 01 (Reapproved 2007)

[134] ATSM D7905, Standard Test Method for Determination of the Mode II Interlaminar Fracture Toughness of Unidirectional Fiber-Reinforced Polymer Matrix Composites, Designation: D7905 / D7905M - 14

[135] ASTM D6671=D6671M - 06, Standard Test Method for Mixed Mode I-Mode II Interlaminar Fracture Toughness of Unidirectional Fiber Reinforced Polymer Matrix Composites, Annual book of ASTM standards, West Conshohocken, ASTM 15.03, 2012.

[136] Rybicki E.F., Kanninen M.F. A Finite Element Calculation of Stress Intensity Factors by a Modified Crack Closure Integral. Eng Fract Mech 9:931–938, 1977.

[137] Krueger R. The virtual crack closure technique: history, approach and applications. ICASE report no. 2002-10, NASA/CR-2002-211628, 2002.

[138] P. Robinson and S. Das, Mode I DCB testing of composite laminates reinforced with z-direction pins: A simple model for the investigation of data reduction strategies. Engineering Fracture Mechanics 2004; 71(3): 345–364.

[139] L.K. Jain and Y.-W. Mai, On the effect of stitching on mode I delamination toughness of laminated composites. Composites Science and Technology 1994; 51(3): 331–345.

[140] L. Tong and X. Sun, Bending effect of through-thickness reinforcement rods on mode II delamination toughness of ENF specimen: Elastic and rigid-perfectly plastic analyses. Composites Part A: Applied Science and Manufacturing 2007; 38(2): 323–336.

[141] M. Grassi, B. Cox and X. Zhang, Simulation of pin-reinforced single-lap composite joints. Composites Science and Technology 2006; 66(11-12): 1623–1638.

[142] W. Yan, H.-Y. Liu and Y.-W. Mai, Numerical study on the mode I delamination toughness of

z-pinned laminates. Composites Science and Technology 2003; 63(10): 1481–1493.

[143] Allegri G, Zhang X. On the delamination and debond suppression in structural joints by Z-fibre pinning, Composites: Part A 38 (2007) 1107–1115

[144] Ratcliffe JG, O'Brien TK. Discrete spring model for predicting delamination growth in Z-fiber reinforced DCB specimens. NASA/ TM-2004-213019, May 2004.

[145] F. Bianchi, Numerical Modelling of Through-Thickness Reinforced Structural Joints, Cranfield University 2012

[146] Jain LK, Mai Y-W. Analysis of Stitched Laminated ENF Specimens for Interlaminar Mode-II Fracture Toughness. International Journal of Fracture 1994;68:219-244.

[147] Mohamed G, Allegri G, Yasaeec M, Hallett SR, Cohesive element formulation for z-pin delamination bridging in fibre reinforced laminates, International Journal of Solids and Structures 132–133 (2018) 232–244

[148] Allegri G, Yasaee M, Partridge I, Hallett S, 2014. A novel model of delamination bridging via z-pins in composite laminates. Int. J. Solids Struc 51 (2014) 3314–3332

[149] Bianchi F, Zhang X. A cohesive zone model for predicting delamination suppression in z-pinned laminates. Compos Sci Technol 2011;71:1898-907.

[150] Bianchi F, Zhang X, Predicting mode-II delamination suppression in z-pinned laminates, Composites Science and Technology 72 (2012) 924-932.

[151] Cui H, Li Y, Koussios S, Zu L, Beukers A. Bridging micromechanisms of Z-pin in mixed mode delamination. Compos Struct 2011;93(11):2685-95.

[152] Peerlings RHJ, Brekelmans WAM, De Borst R, Geers MGD, Gradient-enhanced damage modelling of high-cycle fatigue, Int. J. Numer. Meth. Engng 2000; 49:1547-1569.

[153] L.E. Asp, The effects of moisture and temperature on the interlaminar delamination toughness of a carbon/epoxy composite. Composites Science and Technology 1998; 58(6): 967–977.

[154] Abaqus Theory Guide, 3.2.1 Solid element overview

[155] M. Alfano, F. Furgiuele, L. Pagnotta, and G. H. Paulino, Analysis of Fracture in Aluminum Joints Bonded with a Bi-Component Epoxy Adhesive, Journal of Testing and Evaluation, Vol. 39, No. 2

[156] Zhengwen Jianga, Shui Wana, Zhipeng Zhonga, Minghong Li, Kongjian Shen, Determination of mode-I fracture toughness and non-uniformity for GFRP double cantilever beam specimens with an adhesive layer, Engineering Fracture Mechanics 128 (2014) 139–156

[157] D.D.R. Carti´ e, B.N. Cox and N.A. Fleck, Mechanisms of crack bridging by composite and metallic rods. Composites Part A: Applied Science and Manufacturing 2004; 35(11): 1325–1336.

[158] ABAQUS 6.14 documentation, bending analysis

[159] S. Stelzer, A.J. Brunner, A. Argüelles, N. Murphy, G.M. Cano, G. Pinter, Mode I delamination fatigue crack growth in unidirectional fiber reinforced composites: Results from ESIS TC4 round-robins, Engineering Fracture Mechanics 116 (2014) 92–107

[160] Weixing Yao，Jacques Renard，Norbert A. Himmel, Fatigue Behaviour of Fiber Reinforced Polymers: Experiments and Simulations, page 49-64

[161] M. Beghini, L. Bertini, P. Forte, Experimental investigation on the influence of crack front to fiber orientation on fatigue delamination growth rate under mode II, Composites Science and Technology 66 (2006) 240–247

[162] Chen Y, Liu W, Mixed mode delamination static and fatigue crack growth of unidirectional CFRP composite laminates, Cranfield University MSc thesis (Academic Year: 2014-2015).

[163] Khanh-Hung Nguyen, Viet-Hoai Truong, Jin-Hwe Kweon, a study on failure behaviors of repaired composite structures with scarf bonded patch, ICA-2016

[164] K. Pingkarawat, A.P. Mouritz, Comparative study of metal and composite z-pins for delamination fracture and fatigue strengthening of composites, Engineering Fracture Mechanics 154 (2016) 180–190

[165] A. Argu¨ elles, J. Vin˜a, A.F. Canteli, M.A. Castrillo, J. Bonhomme, Interlaminar crack initiation and growth rate in a carbon-fibre epoxy composite under mode-I fatigue loading, Composites Science and Technology 68 (2008) 2325–2331

[166] Weixing Yao，Jacques Renard，Norbert A. Himmel, Fatigue Behaviour of Fiber Reinforced Polymers: Experiments and Simulations, page 49-64

[167] Georgia Charalambous ,Giuliano Allegri, Stephen R. Hallett, Temperature effects on mixed mode I/II delamination under quasi-static and fatigue loading of a carbon/epoxy composite, Composites: Part A 77 (2015)

[168] Bianchi F, Koh TM, Zhang X, Partridge IK, Mouritz AP. Finite element modelling of z-pinned composite T-joints, Composites Science and Technology 73 (2012) 48–56

[169] Strouboulis T, Copps K, Babuska I. The generalized finite element method. Comput Methods Appl Mech Eng 2001;190(32–33):4081–193.

[170] Belytschko T, Black T. Elastic crack growth in finite elements with minimal remeshing. Int J

Numer Meth Engng 1999;45(5):601–20.

[171] Moës N, Dolbow J, Belytschko T. A finite element method for crack growth without remeshing. Int J Numer Meth Engng 1999;46(1):131–50.

[172] Belytschko T, Gracie R, Ventura G. A review of extended/generalized finite element methods for material modeling. Modell Simul Mater Sci Engng 2009;17(4).

[173] Fries T-P, Belytschko T. The extended/generalized finite element method: an overview of the method and its applications. Int J Numer Meth Engng 2010;84(3):253–304.

[174] Iarve EV, Gurvich MR, Mollenhauer DH, Rose CA, Dávila CG. Mesh-independent matrix cracking and delamination modeling in laminated composites. Int J Numer Meth Engng 2011;88(8):749–73.

[175] Song JH, Areias PMA, Belytschko T. A method for dynamic crack and shear band propagation with phantom nodes. Int J Numer Meth Eng 2006;67:868–93.

[176] Van de Meer FP, Sluys LJ. A phantom node formulation with mixed mode cohesive law for splitting in laminates. Int J Fract 2009;158:107–24.

[177] Chen BY, Pinho ST, De Carvalho NV, Baiz PM, Tay TE. A floating node method for the modelling of discontinuities in composites. Engng Fract Mech 2014;127:104–34.

[178] Chen BY, Tay TE, Pinho ST, Tan VBC. Modelling the tensile failure of composites with the floating node method. Comput Methods Appl Mech Eng 2016;308:414–42.

[179] Chen BY, Tay TE, Pinho ST, Tan VBC. Modelling delamination migration in angle-ply laminates. Compos Sci Technol 2017;142:145–55.

[180] Li X, Chen J. An extended cohesive damage model for simulating multicrack propagation in fibre composites. Compos Struct 2016;143:1–8.

[181] Li X, Chen J. The implementation of the extended cohesive damage model for multicrack evolution in laminated composites. Compos Struct 2016;139:68–76

[182] Liu W, Yang QD, Mohammadizadeh S, Su XY, Ling DS. An accurate and efficient augmented finite element method for arbitrary crack interactions. ASME J Appl Mech 2013;80(4):041033.

[183] Liu W, Yang QD, Mohammadizadeh S, Su X. Y. An efficient augmented finite element method (a-fem) for arbitrary cracking and crack interaction in solids. Int J Numer Methods Eng 2014;99(6):438–68

[184] M. Naderi, N. Iyyer, 3D modeling of arbitrary cracking in solids using augmented finite

element method, Composite Structures 160 (2017) 220–231

[185] M.M. Shokrieh, H. Rajabpour-Shirazi, M. Heidari-Rarani, M. Haghpanahi, Simulation of mode I delamination propagation in multidirectional composites with R-curve effects using VCCT method, Computational Materials Science 65 (2012) 66–73

[186] Sylwester Samborski, Numerical analysis of the DCB test configuration applicability to mechanically coupled Fiber Reinforced Laminated Composite beams, Composite Structures 152 (2016) 477–487

[187] Huifang Liua, Hailiang Niea, Chao Zhanga, Yulong Lia, Loading rate dependency of Mode I interlaminar fracture toughness for unidirectional composite laminates, Composites Science and Technology 167 (2018) 215–223

[188] Wei Ding, Delamination Analysis of Composite Laminates, University of Toronto 1999 (PhD Thesis)

[189] Jarno Jokinen, Markus Wallin, Olli Saarela, Applicability of VCCT in mode I loading of yielding adhesively bonded joints—a case study, International Journal of Adhesion & Adhesives 62(2015)85–91

[190] Crisfield, M. A. 1997. Non-linear Finite Element Analysis of Solids and Structures, Chichester, UK., John Wiley & Sons.

[191] J.Bonet, R.D. Wood, Solution procedures for the finite element analysis of superplastic forming of thin sheet, Computational Plasticity, UK,1987,pp.927-939

[192] C. G. Broyden, The convergence of a class of double-rank minimization algorithms, J. Inst. Math. Appl. 6 (1970) 76-90.

[193] M. A. Crisfield, A fast incremental / iterative solution procedure that handles snap-through, Comput. Struct. 13 (1981) 55-62.

[194] J. Nocedal, S. Wright, Numerical Optimization, second ed., Springer, 2006.